Performance Investigation of Bladeless Micro-expanders

Avinash Renuke

Università di Genova

Thermochemical Power Group
Since 1998

UNIVERSITY OF GENOA

PHD IN MACHINE AND SYSTEM ENGINEERING FOR ENERGY, THE
ENVIRONMENT AND TRANSPORT

Department of Mechanical, Energy, Management and Transport Engineering,
Genoa, Italy

Performance Investigation of Bladeless Micro-expanders

by

Avinash Renuke

Thesis submitted for the degree of *Doctor of Philosophy* (XXXIV cycle)

May 2022

Prof Alberto Traverso   Supervisor, UniGe

Prof Mario Ferrari   Co-Supervisor, UniGe

PREFACE

अहं ब्रह्मास्मि

My identity is with the cosmos.

La mia identità è con il cosmo.

Firstly, I wish to express my deepest gratitude to *Prof. Traverso*, for allowing me to be a part of their research group. I thank him for inspiring and at the same time for his flexibility and patience. I wish to demonstrate my sincere gratitude towards my colleagues, *Matteo Pascenti, Federico Reggio and Marco Ferrando,* who allowed me to have a valuable experience in the experimental facility of TPG research group.

I am also particularly grateful to *Prof. Mario Ferrari and Prof. Alessandro Sorce* for their support during my PhD activities. I thank the Horizon-2020 project – *PumpHeat - and SIT Technologies Company* for making me a part of their research activities to explore Tesla expanders in two-phase domains. My deepest gratitude goes also to, *Dr. Vishnu Sishtla (Carrier, USA), Prof. Daniele Fiaschi (University of Florence), Dr. Matthew Traum (University of Florida) and Dr Paolo Silvestri (SIT Technologies, Italy)*, for being part of TTIO (Tesla Turbomachinery Research Organisation) and encouraging this organisation.

Finally, I dedicate this thesis to my brothers *Anant and Ajay, and my family* for encouraging me to pursue my dreams far away from home.

Avinash Renuke

Genova, May 2022

Invention is the most important product of a human's creative brain. The ultimate purpose is the complete mastery of mind over the material world, the harnessing of human nature to human needs.

L'invenzione è il prodotto più importante del cervello creativo umano. Lo scopo ultimo è la completa padronanza della mente sul mondo materiale, l'imbrigliamento della natura umana per i bisogni umani.

Nikola Tesla

My inventions, The autobiography of Nikola Tesla

ABSTRACT

Interest in small scale turbines is growing mainly for small scale power generation and energy harvesting applications. Conventional bladed turbines impose manufacturing limitations, lower performance and higher cost, which hinder their implementation at a small scale. Tesla bladeless turbomachines are recently being investigated due to many advantages such as their simple design and ease of manufacturing with acceptable performance. If an efficient design is achieved, this will be a promising machine in the area of small-scale power generation and energy harvesting. However, low (less than 40%) overall experimental isentropic efficiency has been recorded in the literature for Tesla turbines.

In this study, firstly, a 0-D model is developed to design the expander rotor. A systematic algorithm is presented, and results of the model are compared with 2-D rotor model results. A 3D computational fluid dynamic (CFD) analysis of rotor and stator with real fluid gas is performed to characterize flow in the Tesla micro expander (all three prototypes studied). The experimental turbine efficiencies were found to be lower compared to the CFD results. The gap in the efficiency is discussed by analyzing CFD and experimental results.

A systematic experimental, numerical performance and losses investigation of Tesla turbines for micro-power generation is carried out combining experimental and numerical approaches. In the first prototype, a flexible test rig for the Tesla turbine fed with air is developed of about 100W net mechanical power, with a modular design of two convergent-divergent nozzles to get subsonic as well as supersonic flow at the nozzle exit. Extensive experiments are done by varying design parameters such as disk thickness, the gap between disks, radius ratio and outlet area of exhausts with speeds ranging from 10000 rpm to 40000 rpm. Major losses such as stator and ventilation losses at end disks together with mechanical, leakage and exhaust losses are evaluated experimentally and numerically. The effect of design parameters on the performance of Tesla turbines is discussed. The experimental analysis focused mainly on the efficiency features of this expander, showing the impact on performance of different disk gaps, disk thickness, discharge holes, exhaust geometry, as a function of speed and mass flow. Maximum adiabatic efficiency of **18%** has been measured, with many other points in the 10-15% range. Results show that the three largest sources of losses are the nozzle losses (which

include the nozzle and nozzle-disk tip interaction losses), the leakages losses (due to flow bypassing the rotor at the extremes gaps), and ventilation losses. The nozzle losses account, alone, for about 2/3 of overall losses.

In the second prototype, the experimental performance investigation of a 3 kW (rated power) expander with a high-speed integrated generator is carried out. The Tesla expander and electric generator are housed in a single casing making it the first of its kind to be tested with such configuration. The expander is fed with air and operated at high rotational speeds up to 40000 rpm. The test is carried out with a different number of nozzles (1, 2, 4 and 8) to understand its effect on performance. Results show that the peak efficiency for two nozzles is better than one-nozzle and four-nozzles configurations for the same inlet pressure conditions. Experimental tests revealed that this turbine is the most efficient Tesla turbine till now with air as a working fluid. Furthermore, one of the most important losses in Tesla turbomachines, nozzle loss, is experimentally characterized. Maximum isentropic efficiency is obtained for two-nozzle case which is 36.5% at 10000 rpm. This is the highest Tesla turbine efficiency recorded till now for actual prototypes with air as a working fluid.

Using such 3-kW Tesla expander air prototype, systematic experimental characterization of loss mechanisms is performed. The sources of losses discussed are stator losses, stator-rotor peripheral viscous losses, end wall ventilation losses and leakage losses. Once the effects of losses are separated, their impact on the overall efficiency curves is presented. This experimental investigation, for the first time, gives insight into the actual reasons for the low performance of Tesla turbines, highlighting critical areas of improvement, and paving the way to next-generation Tesla turbines, competitive with state-of-the-art bladed expanders.

The third prototype is designed with an innovative concept "Ultra-high Tesla expander" which is developed based on findings of the first two prototypes aiming to minimize stator-rotor losses and then potentially approaching the rotor-only efficiency for the overall machine. The prototype is 1 kW (rated power) with water as working fluid. The 3D numerical results show very high total to static efficiency (70 -75%). The preliminary experimental tests results are discussed and ventilation loss, which is major source of loss in this expander, is characterized.

CONTENTS

LIST OF FIGURES

LIST OF TABLES

NOMENCLATURE

b	gap between disks	[mm]
d	diameter	[mm]
e	specific internal energy	[J/kg]
g	function	[-]
h	enthalpy	[J/kg]
k	specific heat ratio	[-]
l	arm length of flywheel	[m]
$\dot{m}$	mass flow rate	[g/s]
n	number of samples	[-]
nc	number of channels	[-]
nz	nozzle	[-]
p	pressure	[Pa]
r	radius	[mm]
v	velocity	[m/s]
x	variable	[-]
A	area	[m^2]
C	specific heat	[J/kgK]
D	hydraulic diameter	[m]
F	drag enhancement number	[-]
Fr	force	[N]
G	gap ratio	[-]

L	length	[m]
K	empirical constant	[-]
N	rotational speed	[rpm]
U	uncertainty	[-]
P	power	[W]
Po	Poiseuille's number	[-]
Q	volume flow rate	[m^3/s]
Re	Reynolds number	[-]
SD	standard deviation	[-]
T	temperature	[^{o}C]
W	specific work	[J/kg]
Y_N	nozzle loss coefficient	[-]
α_o	inlet flow angle (absolute)	[^{o}]
β_o	Inlet flow angle (relative)	[^{o}]
β	minor loss coefficient	[-]
ε	expansion ratio	[-]
η	efficiency	[-]
μ	dynamic viscosity	[Pa·s]
ρ	density of fluid	[kg/m^3]
σ	target of fitting procedure	[-]
τ	torque	[N·m]
$\bar{\tau}$	stress tensor	[-]
ω	angular velocity	[rad/s]
$\dot{\omega}$	rotational acceleration	[rad/s^2]
ζ	total pressure loss coefficient	[-]
ξ	dimensionless radius ratio	[-]
Ψ	Degree of reaction (DoR)	[-]

Subscripts

atm	atmospheric
amb	ambient
avg	average
c	rotoric channel
e	exhaust manifold
exit_loss	exit losses
exp	experimental
exp.tot.st	experimental total to static
e.st	exit static
in	inlet of turbine
id	ideal
i	inner edge of disk
in.tot	total properties at nozzle inlet
kin	kinetic
line	compressed air line before turbine
loss	losses
m	modified
nz_loss	nozzle loss
o	outer edge of disk
p	pressure
p.in	inlet pressure
p.o	pressure at outer edge of disks
r	radial
ref	reference
rel	relative

res	resistive
stat	static
t	tangential
tot.stat	total to static
η	efficiency

Superscripts

'	isentropic condition
a	exponential term of ventilation losses

Abbreviations

CFD	Computational Fluid Dynamics
COP	Coefficient of Performance
TPC	Total Pressure loss Coefficient
TTIO	Tesla Turbomachinery International Organization

Chapter 1   Introduction and State of the Art

1.1   Motivation

There are interesting areas where demand for small scale turbomachinery is foreseen such as oil and gas, refineries, geothermal, solar, fuel cell systems, micro-gas turbines, space and small-scale power applications. These applications require a cost-effective and efficient turbomachinery solution. The performance of bladed turbines drops at small scale and the manufacturing cost is higher due to the complex blading system. Tesla/bladeless turbine is a plausible alternative to traditional turbomachinery at small scale.

A potential market for Tesla turbine technology is energy harvesting in heat pump and refrigeration cycles. This technology can first enter within large size heat pumps (1-100 MWth), targeting in the mid-term small size heat pumps, down to domestic fridges and air conditioners. Once this technology is demonstrated, the global heat pump market would likely quickly embrace it to reach a higher performance standard. At the current stage, the European Heat Pump Association (EHPA) reports that the heat pump market for 2022 in Europe will be characterized by 35.6 GWth new installations, which corresponds to approximately 10 billion euros. Other estimations underline that 2017/2018/2019 have been interesting years for this sector: more than 240000/year units have been sold in France and more than 170000/year units in Italy, the second-largest market in the EU (Figure 1.1 left). This means that the heat pump market is taking off, mainly driven by energy efficiency targets.
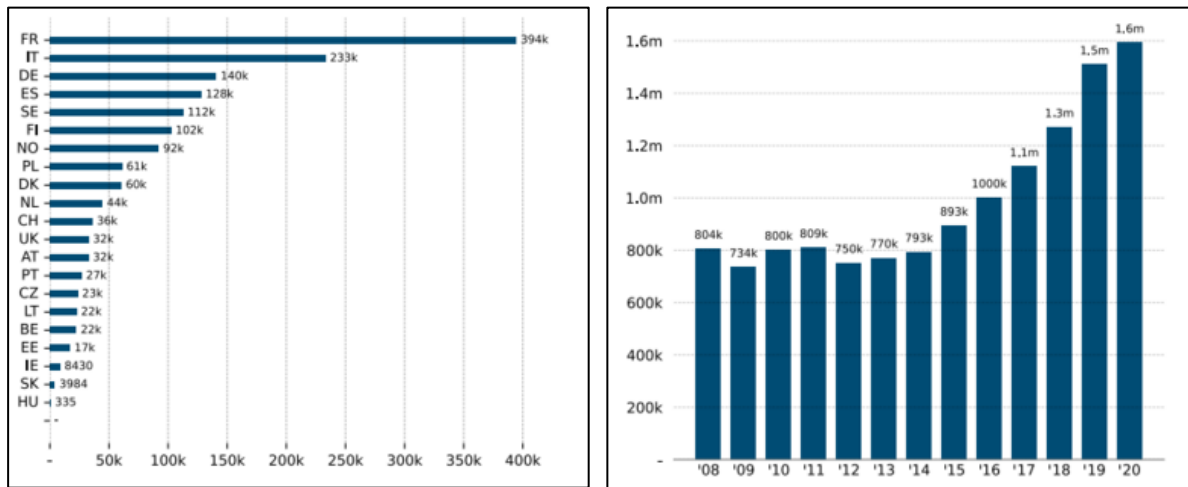
Figure 1.1 (left) Heat pump market development from 2007 to 2020 in 21 European Countries [EHPA, 2021]; (right)Units sold by the country in 2020, 21 European Countries [EHPA stats]

In Europe, it is clear that the most promising markets are for sure localized within Mediterranean countries, such as Italy and France, but relevant attention must be given to Nordic countries, such as Sweden and Norway, that have an interesting balance between population and heat pump installations. Furthermore, it is important to underline that the target market is not constituted by new installations only, but also by the possibility of retrofitting most of the existing heat pumps, of any size. This represents an unprecedented business opportunity, as well as a necessary technical upgrade, which may benefit from National subsidies. The current scenario in Italy is characterized by huge utilization of reversible air-source heat pumps, mainly used for summertime cooling. It is clear that there is great potential for improvement in both qualitative and quantitative terms, considering the continuous growth of the sector within past years (Figure 1.1 right).

The use of Tesla in small and micro-ORC (Organic Rankine Cycles cycle) can allow the advent of this new niche market, where ORCs suffer due to their high investment cost, which is significantly influenced by the expander. Demonstration of affordable turbine technology with minimal maintenance requirements would give ORC a significant boost up in this field. Their application as low-temperature energy harvesters might spread ORCs at capillary level, like
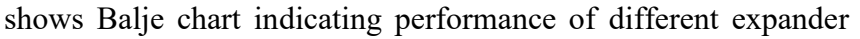
smart grids, with an EU potential in the order of thousands of units. The possible hurdles in the realization of conventional expanders in small scale ORC applications are:

- High cost and high maintenance of existing expanders
- Low efficiency at small power scale ORC applications
- Use of lubrication not permitted in several applications.

A low cost, efficient and reliable Tesla expander technology is promising for small scale ORC applications.

In the biomedical field, it is required to have low noise, compact and efficient pumps/turbines. Conventional bladed turbines or pumps create high noise and change the working fluid characteristics, which is undesirable in the biofluids. Tesla turbine/pumps are suitable for these applications where compact, low noise and efficient machines are required. Another inherent feature of the Tesla turbine/pump is that the working fluid characteristics remain unchanged due to laminar flow inside the rotor, which is an important criterion in medical applications such as blood pumps.

Tesla machinery is inherently reversible, as it is sufficient to reverse the direction of rotation to reverse the flow direction. However, this property of Tesla machinery has not been sufficiently exploited so far, due to the limited knowledge of such technology and research/demonstration of such concept. Another major obstacle has been constituted by the difficulty in designing efficient bladeless machinery.

Balje diagram[43] is one of the means which is used in the selection of conventional turbines and expanders. shows Balje chart indicating performance of different expander technologies. Balje diagram shows the isentropic efficiencies as a function of specific speed. The specific speed and specific diameter are calculated and represented on Balje diagram for Tesla expanders used in this thesis i.e. air 100 W, air 3 kW and water 1kW at the maximum efficiency condition. Conventional turbines are usually operated in the high specific speeds and low specific diameters, while the Tesla turbine is characterised by relatively high specific diameter and low-medium specific speeds closer to the drag turbines and volumetric expanders.
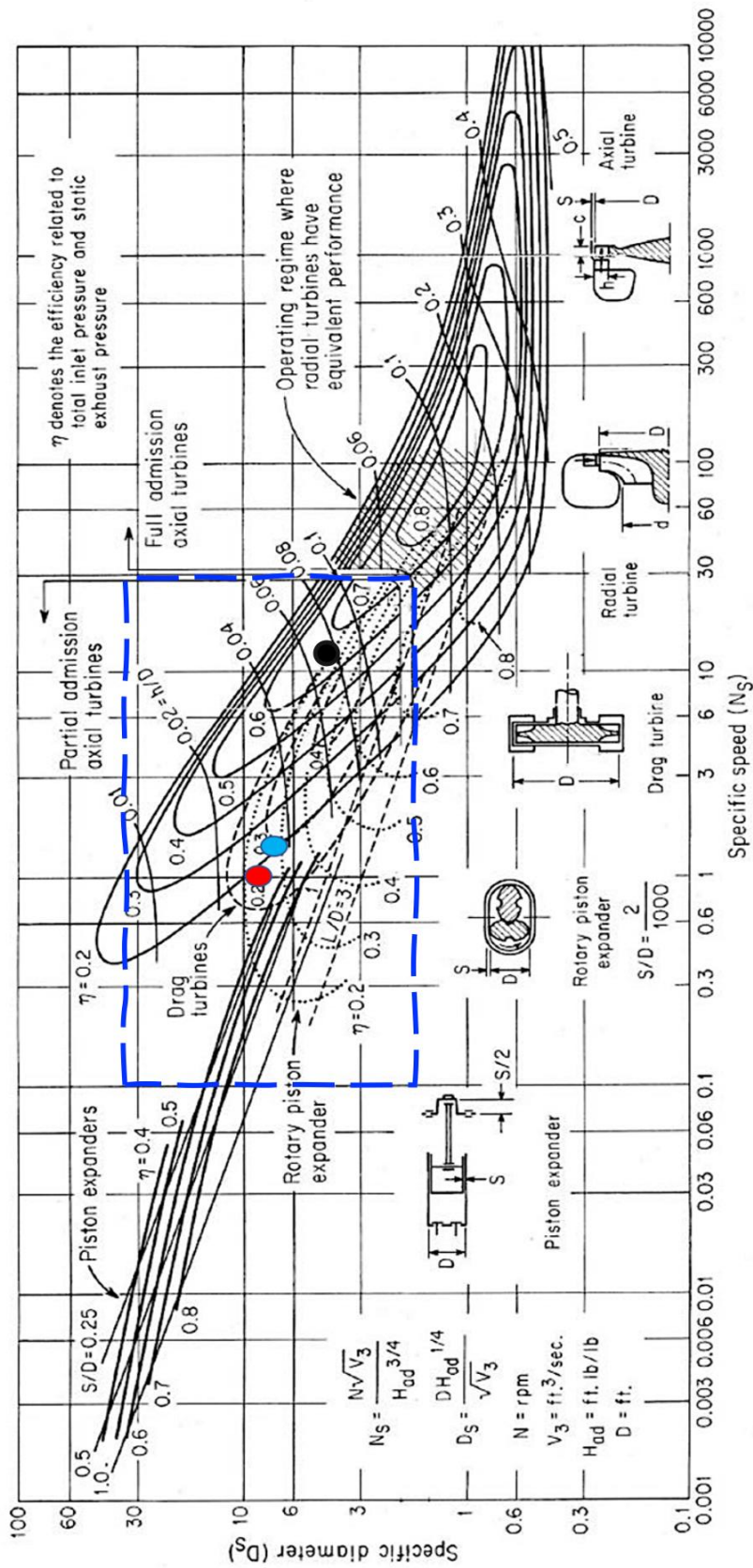
Figure 1.2: Performance of several expanders on Balje map [29]: Tesla expanders in studied in this thesis are represented by : red dot - air 100W, blue dot - air 3 kW and black dot - 1kW water Tesla expander. The blue dotted line represents zone in which Tesla expanders could be operated based on literature data.

The Tesla turbine is still in the early stages of development and many researchers are investigating the technology numerically and experimentally. However, a deep understanding regarding the low performance of these devices is still vague and the lack of systematic design methodology hinders its further development. There is a need for a structured research effort towards the efficient and well-designed Tesla machinery, albeit in the kW ratings, where their features are competitive or more promising than other conventional machinery, allowing us to tap into their potential for becoming one of the key technologies in the turbomachinery field. The present study involves an attempt towards a deeper understanding of the performance of Tesla expander through experimental campaigns on several prototypes and numerical simulations for better clarity on the performance.

1.2   Tesla Bladeless Turbomachinery

1.2.1 Nikola Tesla – The Inventor

Nikola Tesla was a mechanical, electrical engineer and inventor, born in Croatia. He is mostly known for his contributions in the field of electromagnetism, such as the distribution of electricity with alternating current and electric motor driven by alternating current. But he has also contributed to other engineering areas, among which the development of novel turbomachinery, known today as Tesla turbomachine in his honour. Tesla turbine and compressors use smooth, circular disks instead of vanes, and placed inside housing. The principle of the Tesla turbine is founded on two main phenomena: adhesion and viscosity

The bladeless turbomachinery was invented by Nikola Tesla in 1913[1][2] as shown in Figure 1.3. What Tesla claims in his patents was a high efficiency due to the form of energy transfer, based on the assumption that the highest performance will be attained when the changes in velocity and direction of the movement of the fluid are as gradual as possible. This can be accomplished by causing the propelling fluid to move in a natural paths or streamlines of the least resistance, free from constraints and disturbances caused by vanes in common turbomachinery, and changing the fluid velocity and direction of movement.
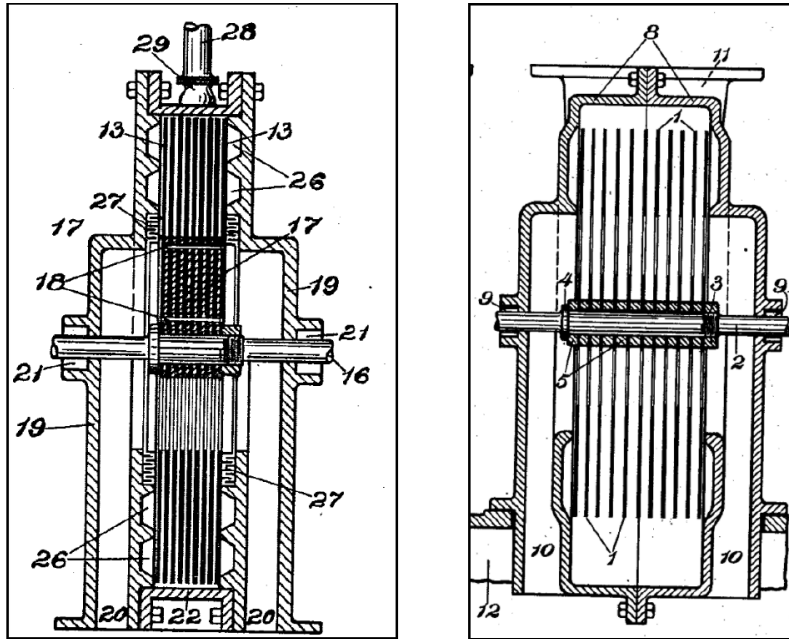
Figure 1.3 Nikola Tesla's patents: "Turbine" (left) and "Fluid Propulsion" (right)

The efficiency of the rotor which works within a laminar flow can hit above 95% isentropic efficiency. However, the flow rate values must be as low as possible to attain high rotor efficiency. In other words, it requires a large number of disks and hence a physically large rotor to achieve the above objective.

1.2.2 Principle of Operation

Tesla turbines or bladeless turbines consists of thin disks with a central hole, mounted parallelly on the shaft with spacing between them, as shown in Figure 1.4. In turbine mode, fluid enters tangentially to the rotor and leaves the rotor through the centre axially. In compressor mode, fluid enters from the central holes of the disks and leaves through the periphery. The high speed of the fluid at the periphery is then converted into static pressure using the external volute. Hence, this machine is reversible i.e. by changing the rotational direction of the rotor both the modes, turbine and compressor, are possible using a single machine. The relative velocity between fluid and disks is very low compared to conventional bladed turbines. Due to the lower relative velocity, the flow inside the rotor is laminar. And this is the key for the effective energy transfer between the fluid and the disk. The energy exchange between the fluid layers and

between the last fluid layer to the disk is due to shear force. The drag force generated on the disk resulting from this shear is in the direction of rotation of the disk. Hence, in the case of the Tesla rotor, viscous shear drag is in favour of power generation unlike a loss in the case of a bladed turbine where viscous drag is in the opposite direction of rotor motion. This interesting phenomenon has attracted many researchers to study bladeless turbines.
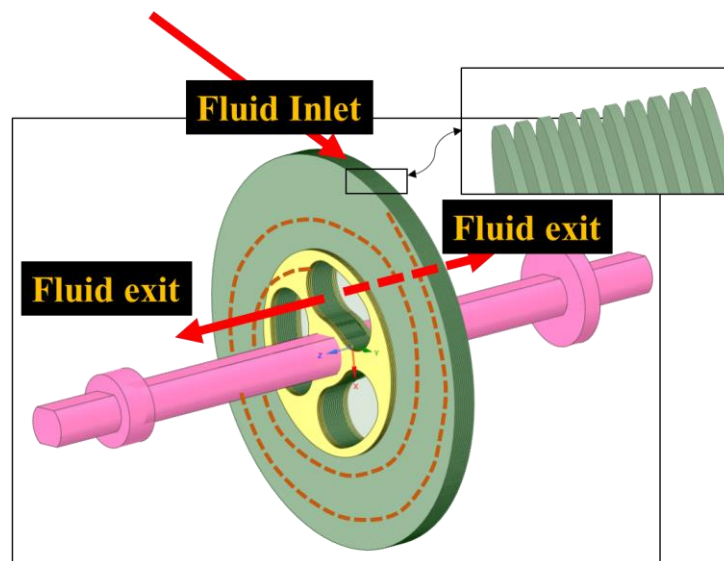
Figure 1.4 Schematic of Tesla turbine rotor showing principle of operation

Opportunities and challenges of bladeless turbines/compressors

Tesla turbines are promising in various applications where conventional turbines impose several issues. Following are some of the pros and cons of Tesla turbines:

Opportunities:

- High rotor efficiency
- Reversible machine
- Absence of impingement (erosion free)
- Laminar flow inside the rotor
- High reliability
- Easy to manufacture
- Ability to handle dirty fluids – abrasive fluid, two-phase fluids, etc.

Challenges:

- Large gap between theoretical and experimental performance
- No detailed research on stators suitable for bladeless turbomachinery
- No systematic assessment of losses
- Very few experimental data available for complete turbine/compressor set-ups

1.3   State of the Art

Tesla claimed to have very high rotor efficiency (up to 97%)[5]. This has also been proved analytically by researchers. However, in practice, the overall Tesla turbine efficiency has been found very low (< 35%) as shown in Table 1.1. This lower efficiency of Tesla turbine as compared to conventional bladed turbomachinery has been one of the core reasons why it hasn't been commercially successful till now. In the following section, state of the art research on Tesla turbines is reviewed.

1.3.1 Experimental Research

Many researchers modified the Tesla turbine configuration to enhance its performance. Analysis of key experimental literature is presented in chronological order to highlight the progress of research in the Tesla turbine domain. Tesla build a steam turbine to demonstrate his bladeless turbine concept with 25 disks, disk diameter of 457 mm and 2.9 mm gap between disks. He recorded the output power of 147 kW with 957 g/s mass flow as shown in Table 1.1. This was the first construction and demonstration of the bladeless turbine. Armstrong[3] modified the Tesla turbine by tapering all the disks with one side from a thickness of 0.254 mm at the outer diameter to 4.76 mm (3/16 inch) at the shaft. Maximum efficiency of 4.3% with steam as working fluid was reported. Low efficiency was due to an ineffective sealing mechanism. The major focus of the experiment was to demonstrate the effect of nozzle size and shape upon turbine performance. Convergent-divergent nozzle performed better than the straight nozzle, with the same pressure drop, producing 47% more power. It was observed that the efficiency of the turbine seemed to increase with greater pressure drops through the nozzle. Beans[4] wrote his PhD thesis on performance characteristics of friction disk turbines. The

objective of his thesis was to verify the theoretical analysis with experimental data with nozzle inlet pressure and spacing between disks as control parameters. Efficiency was found to be higher at lower disk spacing and lower inlet nozzle pressure. The maximum turbine efficiency obtained by the experiment was 24%. He also cited the work of Muhlstein and Read, who developed a Tesla turbine for air with 10 disks, 99 mm in diameter and 1.6 mm thick. The spacing between disks was the same as thickness. Maximum efficiency with air as working fluid was 11.1% at a supply pressure of 1.38 barg@6430 rpm. Since the nozzles limit the entrance velocity to sonic velocity, investigators concluded that turbine efficiency is the main function of the inlet velocity ratio between fluid and disk. Rice[5] has made several Tesla turbine prototypes and improved them over time. Analytical as well as experimental data has been discussed in his paper. Three turbine models, with air as a working fluid, achieved maximum efficiency of 34.8%.

Table 1.1 Experimental and numerical literature data for Tesla turbo expanders

Author	Fluid	# of disks	Disk Thickness, mm	Disk dia, mm	Inner disk dia, mm	Gap, mm	Inlet pressure, barg	Mass flow, g/s	RPM	Nozzle	Power	Efficiency, %
Tesla [1][2]	Steam	25	0.79	457.2	[--]	2.9	8.62 (dry sat)	957	9000	[--]	147 kW	46.6[1]
Amstrong [3]	Steam	10	6.35	177.8	25.4 (6 holes)	[--]	6.89		6000	6.83 mm hole	382.5 W	[--]
							6.89	[--]	5500	3.18 mm thorat + 15 deg diverging	382.5 W	[--]
							8.14		8300	6.83 mm throat + 7 deg diverging	816.4 W	[--]
Beans [4]	Air	7	0.66	152.4	15.9 (6 holes)	1.55	[--]	[--]	[--]	Two nozzles - 14.29 mm hole (inlet) to 12.7 mm x 4.76 mm (exit)	[--]	23.5[2]
Muhlstein et al[4]	Air	10	1.59	99.06	[-] (8 holes)	1.59	4.14	16.6	19000	1.59 mm (18 holes)	183.9 W	9.99[2]
							1.38	4.85	6430		33.8 W	11.1[2]
Rice [5]	Air	9	2.38	177.8	[--]	1.59	8.62	36.4	10000	Two nozzles(CD)-15 deg diverging	1235.6 W	23.2[3]
		11	[--]	[--]	[--]	1.016	2.76	21.31	9200	10 deg diverging	625.2 W	25.8[3]
		24	0.508	203.2	33.7	0.508	5.15	[--]	17200	20 deg diverging	2942 W	34.8[3]
Bloudíček, P., and Paloušek [6]	Water	[--]	2	200	[--]	[--]	[--]	1192 (1.192 lps)	400	[--]	13.6 W	54.9[4]
Guha[7]	Air	4	0.9	92	25	[--]	2.9	[--]	25000	[--]	140 W	25[4]
Vedavalli [9]	water	20	0.125	10		[--]	0.125	0.15	8	5590	converging circular 0 deg	20.3 mW	18.4[4]
		20				[--]	0.125	0.13	8	5264		19.8 mW	19.7[4]
		13				[--]	0.25	0.19	10	6522		16.9 mW	9.3[4]
		20				[--]	0.125	0.01	2	1243		0.4 mW	36.6[4]
		20				[--]	0.125	0.01	2	689	converging circular 0 deg	0.32 mW	27[4]
		13				[--]	0.25	0.06	5	3488		0.87 mW	22[4]
Peshlakai[10]	Air	12	1.5	150	34.5	1.5	[--]	5.5	3600	1 and 1.65 dia holes	6 W	31.1[1]
Holland[11]	Air	[--]	0.8	95	17	0.2	3	[--]	10000	[--]	[--]	8.5[1]
Li et al[12]	Air	13	0.5	80	12.5	1	2.6	390	900	11 mm hole		8[4]
Manfrida [14](Numerical)	R245fa	8	[--]	200	80	0.12	10.09	[--]	[--]	15 deg diverging	40W	15 @M=1
											84W	27 @M=0.4
	n-hexane						1.8	[--]	[--]		22 W	29 @M=1
											34W	39 @M=0.4
Rusin[15]	Air	[--]	1.3	73	27.5	1.5	3	[--]	20500	1.8 mm dia hole	42.5 W	8.4[2]
Manfrida[16]	Air	40	[--]	125	31	0.3	1.49	28	3000	ABS, 4 circular holes 19 mm, thorat 0,8 mm	94 W	11,2[3]
	R1233zd(E)	60		216	55	0.1	5.18	253	3500	4 nozzles, Thorat 1 mm, 85°,	800	30[Num]
The definition of efficieny used by previous literature												
1				2				3			4	
$\eta = P_{output} / \text{Enthalpy drop across turbine}$				$\eta = P_{output} / m\, C_p\, t_0\, (1-(P_2/P_0)^{(k-1)/k}$				$\eta = P_{mechanical\ energy} / P_{isentropic\ expansion\ of\ air}$			$\eta = \tau\omega / Q\, P_0$	

Bloudíček and Paloušek [6] constructed a Tesla turbine to verify its performance. The test was carried out with water and they achieved 54.9% efficiency which is 15 points more than the numerically estimated value making the data points not reliable. Hoya and Guha[7] presented the analysis of the Tesla turbine focusing on the performance measurement system. They have provided a simple method to measure output torque and power in the Tesla turbine. According to their analysis, the low efficiency of the Tesla turbine is due to losses in the nozzle. Also, the inlet system of the turbine was not efficiently designed, leading to total loss of pressure upstream of the nozzle. They obtained the highest efficiency of 25% with 4 disks of 92 mm at 25000 rpm. In the following year, Guha and Smiley[8] studied and focused the work on inlet geometry and nozzle of the turbine. They provided ways to improve them to increase the overall efficiency of the Tesla turbine. According to their experimental analysis, as compared to the old inlet–nozzle assembly, the new design reduced the loss in total pressure by a very large factor (40–50).

An interesting Tesla micro-turbine was built and tested by Vedavalli et al[9] for low-pressure head application. The test was carried out for different configurations of nozzles and rotor. Design parameters such as disk spacing, radius ratio and the number of disks is investigated with water as working fluid. Maximum efficiency, at a low flow rate (2e-06 m^3/s) with 13 disk rotor stack was 36% with 0.4 mW output power. Peshlakai [9]performed an experiment on Tesla expander with air as a working fluid and obtained 6 W of power at 3600 rpm @31.1% efficiency. Holland [11], in his Master thesis, has performed the experimental evaluation of the performance of Tesla turbine and compared results with literature data. He has found that the nozzle angle of 45 deg performed better. This is not expected considering previous research, which suggests an optimum angle somewhere between 5 to 15 deg. Even using an extensive sealing system, overall efficiency of 8.5% was obtained. Li et al[12] developed a test rig for a bladeless turbine to estimate the losses inside the turbine, specifically inlet and exit losses. They have created numerical models to validate their results. They have also shown that the lower the difference between inlet fluid velocity and disks tip velocity, the higher the output of the turbine. An interesting study was done by Schosser[13] in his Master thesis, where highly resolved optical PIV experiments of the radial and the tangential velocity distribution in the small gap between disks of Tesla rotor is performed. Manfrida et al[14] demonstrated analytically Tesla turbine operating on a closed loop with refrigerant fluids, R245fa and n-

hexane. Maximum efficiency was found at a low Mach number at stator exit and it decreases as the Mach number increases for both fluids. Rusin[15] performed an experiential Tesla expander with air as working fluid and obtained 42.5 W of power at 20500 rpm @8.4% efficiency. The effect of inflow conditions on turbine efficiency was investigated by Okamoto and Goto[16]. They have concluded that nozzle angle, opening angle and disk thickness have a significant impact on turbine efficiency.

1.3.2 Analytical and Numerical Research

A three-dimensional computational fluid dynamic analysis of Tesla turbine initially appears in the work done by Ladino[18][19] with air as a working fluid. Geometry is modelled with two simple nozzles. Maximum efficiency of around 20% has been reported. Lemma et al[20] performed an experimental and numerical study on a 50 mm rotor Tesla turbine. The results of the experimental study indicate that the adiabatic efficiency of these machines is around 25%. The main reasons for the low efficiency have been identified as parasitic losses in the bearing and viscous losses in the end walls. The parasitic losses are about 92% of the measured load. Bearing losses are suspected as the main cause of these losses. Lampart et al.[21] developed a CFD investigation on different Tesla turbine dimensions with SES36 (Ansys Fluent database) as a working fluid. The predicted efficiency of the turbine oscillates around 50%. Rusin et al [22]compared the experimental results of the Tesla turbine with numerical analysis by considering the surface roughness of the disks. The highest power and efficiency values obtained were: 55.6 W, 11.2% for inlet pressure 3 bar and 98.3 W, 11.8% for 4 bar. Qi et al[23] performed a numerical analysis to investigate the influence of disk tip geometry on the performance of the Tesla turbine. Wang et al[24] performed a numerical study with stationary components and rotor and discussed the loss mechanisms, particularly in the exhaust area. It is shown that high swirl flow present at the rotor exhaust developed high total pressure loss. The efficiency of the rotor is found to be higher at a low flow coefficient with high dynamic pressure. Sengupta and Guha[25] have performed extensive 3D numerical simulations for inflow-rotor interaction in Tesla disk turbines. They have studied the effect of discrete inflows, finite disk thickness and radial clearance on the fluid dynamics and performance of the turbine.

It is clear from the literature survey that the main sources of losses, resulting in poor performance of Tesla turbine reported, are parasitic losses and stator losses. There is no clear assessment of loss characterization and contribution of each component towards the performance of the Tesla turbine using CFD simulation.

1.3.3 Research based on applications

Tesla turbines have been studied for different applications due to their inherent advantages mentioned before. Steidel and Wiess[26] performed an experimental investigation of Tesla turbines for geothermal applications. The tests were performed with geothermal fluids with a vapour fraction between 6 and 15% with inlet pressure at the turbine from 11 bara to 28 bara. The maximum turbine efficiency observed was 6.8% at 4000 rpm with 1.57 kW power and 205.5 g/s mass flow. Patel and Schmidt[27] carried out an experiment on a boundary layer turbine using biomass combustion gases as working fluid. The test was conducted to verify the effect of deposition, erosion and corrosion of the Tesla turbine due to the substances present in the flue gases. The performance showed isentropic turbine efficiencies of 11% at 3.2 kW with a rotational speed of 6284 rpm. They observed no significant component degradation. The hot components were coated with a small amount of soot, but no deposits were formed. Deam et al[28] analysed the benefits of utilizing Tesla turbines instead of traditional gas turbines for small–scale applications. They demonstrated that for small–scale turbine applications, viscous turbines are more efficient than conventional bladed turbines, as the viscous and clearance losses are quite high in bladed turbines at small scale. The maximum efficiency obtained in turbine experiments was 23.5% with an inlet pressure of compressed air 1.31 bara. Valente[29] applied the Tesla turbine concept as equipment for pressure reduction of hydrocarbon gases to recover part of the elastic energy of a gas in a "near isothermal process". Crowell[30] has reported the use of Tesla turbines in small Organic Rankine Cycles (ORC). Electricity is generated using a solar hot water generator by exchanging solar heat with refrigerant and then passing gaseous state refrigerant into Tesla turbine. Cirincione [31] designed and commissioned a Tesla-hybrid turbine on the test bed with R245fa working fluid. Ho-Yan [32] presented the design methodology of the Tesla turbine in a pico-hydro application. The efficiency of the preliminary turbine design was predicted near 80% (rotor only efficiency) at 300W power, without considering inlet and exhaust losses. Zhao and Khoo [33] designed and

tested a 40 mm bladeless turbine for the harvesting of energy from air and rainwater applications: 0.5 W power output was obtained with air as working fluid at 3300 rpm.

Ruiz [34] demonstrated an interesting use of the Tesla turbine concept as a heat sink in high heat flux cooling applications. A unique type of heat sink device using a Tesla turbine exhibits enhanced heat transfer characteristics with both single-phase and two-phase flow (water as working fluid), which is modelled, manufactured, tested and characterized. Thawichsri and Nilnont [35] performed an experimental comparison between a centrifugal turbine and a Tesla turbine working with isopentane at low temperatures (70–90°C). The experimental assessment demonstrated, that the centrifugal turbine was on average 30% more performing than the Tesla turbine, but also that the Tesla turbine is quite cheap and easy to manufacture a turbine. The maximum efficiency of the Tesla turbine recorded was about 11.9%, the specific power output 35 kJ/kg when the heat source was 90°C. Bankar N et al. [36] designed a hybrid Tesla turbine in which grooves are introduced on the disks for micropower application. Umashankar et al.[37] analysed the application of the Tesla turbine in the cogeneration of heat and power systems. Cogeneration concept and turbine analytical approach were presented. Manfrida et al.[38] worked on the ORC application. The analysis is carried out using different organic fluids: R245fa, R134a, SES36, n–pentane, n–hexane. Their assessment showed that maximum efficiency can be obtained with n-hexane as a working fluid. A potential application of the Tesla turbine is described by Traverso et al. [39][40] as energy recovery of the pressure difference between the condenser and the evaporator of refrigeration systems or heat pumps. The introduction of such expanders in the refrigeration cycle can potentially increase the Coefficient of Performance up to 20%.

1.3.4 Conclusions of state of the art and contribution of the thesis

Literature analysis provided a good insight into the development of Tesla expanders experimentally, numerically and with different fluids. The activities and results are broadly concluded as follows:

1. Experimental: many researchers have performed experimental work on Tesla expanders and provided insight into the performance of the machine. The performance recorded is very low (i.e. total to static efficiency < 35%). However, the loss

characterisation on such expanders to understand its low performance is not carried out in detail. The experimental data is available mostly for low size expander i.e. net power less than 1 kW. The performance of tesla expander at different sizes are not available for the same fluid/design conditions. The design methodology for most of the experimental prototypes are not presented which makes it even more difficult to analyse its performance. The past research also does not discuss extensively about improvement strategies for Tesla expanders based on the analysis performed.

2. <u>Analytical:</u> very significant and impressive work is done in the past by the researchers with analytical studies on flow within Tesla rotor. Analytical analysis helped to understand flow parameters and their correlation with respect to the rotor performance. From the analytical analysis, it is understood that following parameters have the most significant effect on turbine efficiency:

a. The flow rate is proportional to the gap between disks so that it increases almost linearly with the number of disks

b. The flow rate increases at approximately the square of the disk diameter

c. Efficiency is optimal when the Reynolds Number is approximately 5-8, using $Re=(\omega h^2/\upsilon)$, where ω is the angular velocity of the disks, h is the gap width between disks and υ is the kinematic viscosity of the fluid

d. Efficiency increases with increasing diameter ratio and with decreasing flow rate, where the diameter ratio is defined as the ratio of the diameter of the periphery of the disks to the diameter of the axial opening in the disks

e. Pressure at the rotor inlet increases as a week effect of decreasing flow rate and increases non-linearly with an increasing radius ratio

f. Torque increases linearly with increasing flow rate and non-linearly with an increasing radius ratio.

The impact of these parameters on the performance of the rotor is described well. Several non-dimensional correlations are developed which helped to design the Tesla

expander rotor. However, there is no systematic design methodology presented to design rotor for best efficiency and power for different working fluids.

3. Numerical (CFD): numerical analysis started in early 2000. 2D analysis on rotor and 3D analysis on rotor+stator is carried out in the literature with simple geometries. The analysis is mainly performed to characterise the overall performance of the expander and to complement results from analytical analysis to understand major losses inside the machine. The detailed loss characterisation on based on convergent and convergent-divergent nozzles with rotor and comparison with experimental data is not performed.

In order to address the research questions and gaps in the literature presented before, following main contributions to the Tesla expander research is presented in this thesis:

1. Design methodology: This thesis provides the systematic approach to design Tesla rotor for the best efficiency point for given design conditions. The expanders tested and analysed in this thesis are designed using this methodology. The 2D CFD analysis validates the design methodology presented.

2. Numerical analysis: extensive 3D CFD analysis for three different prototypes is presented with detailed loss characterisation. The correlations are tuned with experimental data as well to calculate the losses in the Tesla expander.

3. Experimental campaign: three prototypes for different power size and different fluids (compressible and incompressible) are developed and tested. The detailed loss characterisation on each prototype is carried out.

4. Innovation: the lessons learned from the first prototype is applied to second prototype to improve the performance (achieved highest efficiency for Tesla expander with air as working fluid). The learnings and loss characterisation on second prototype led to innovative ideas (patent filed) which are implemented in the third prototype. The innovation in the different components of the expander is also discussed in the thesis. The thesis also provides the important strategy for the tesla expander based on the analysis done in this thesis.

1.4   Objectives/Problem Definition

This study aims to analyse systematically, from the experimental and numerical points of view, the impact of key parameters on turbine efficiency. Therefore, the objectives of this thesis are:

1. Development of systematic design methodology using 0-D model for Tesla expanders
2. 2D/3D numerical analysis of Tesla expander prototypes
3. Experimental performance investigation of modular Tesla turbine prototypes with flexible test rigs –
    a. <u>100 W Air Tesla expander</u>
        i. To study thoroughly the impact of the following parameters on the performance of Tesla turbine: disk thickness, gap between disks, outlet opening of disk, exhaust area of the turbine
        ii. To characterize the losses inside the turbine
    b. <u>3 kW Air Tesla expander</u>
        i. Design and testing of modular Tesla turbine with flexible test rig with integrated high-speed generator
        ii. Impact of nozzle number on the performance of the turbine
        iii. Experimental characterization of losses
            1. Stator losses: these losses include turbine inlet, nozzle and peripheral viscous friction between stator and rotor
            2. Ventilation losses: these losses consist of viscous friction losses between end disks and casing wall
            3. Leakage losses: these losses include the power loss due to leakage flow
    c. <u>1 kW Water Tesla expander</u>
        i. Design and testing of Tesla expander with water as working fluid
        ii. Experimental loss characterisation
4. Comparison and analysis of numerical and experimental results

1.5   Organisation of Research

The thesis is organised into five chapters.

Chapter 1 outlines the background research and motivation for the study. It introduces bladeless Tesla technology, its original inventions and working principle. The chapter ends with the introduction of research gap in the literature along with some commercial and potential application aspects of it.

Chapter 2 focuses on the analytical calculations (design criteria) and numerical 3D computational fluid dynamics modelling to understand the performance of the bladeless expanders. 3D CFD simulation is done on the three prototypes – 100W air, 3 kW air and 1 kW water.

Chapter 3 describes the experimental campaign tests on the three prototypes mentioned above. The detailed experimental characterisation for performance investigation has been done in this chapter. Results are analysed and discussed for each experimental test prototype.

Chapter 4 describes the loss characterisation of Tesla expanders. Firstly, losses associated with all the components of Tesla expanders are discussed. Furthermore, an experimental loss characterisation for each prototype is discussed in detail.

Chapter 5 concludes by summarising the activities done in this study

Chapter 2   Numerical Investigation

2.1   Tesla Expander Components Analysis

2.1.1   Rotor

The Tesla turbine rotor typically consists of several closely spaced flat disks mounted on a shaft, driven by a fluid flowing between them, in spirals concentric with the shaft, toward the outlet as shown in Figure 2.1. These disks are flat, thin and smooth, spaced along the shaft with thin gaps. The working fluid flows between the disks spirally from the outer to the inner radius and transfers the energy to rotating disks through the boundary layer formed on the disk surface. The fluid enters in the tangential direction through outer periphery and exits axially through the inner exit ports.

The rotor is the heart of Tesla turbomachinery together with conventional or novel stator and exhaust system. The flow between two corotating disks has been studied in the past analytically and the performance is discussed both qualitatively and quantitatively (discussed in section 1.3.2). However, there are no systematic design criteria given for the rotor of a Tesla expander in the literature. In the following section, we present a 0-D preliminary design methodology to calculate rotor parameters such as disk diameters, the gap between disks, number of disks and rotational speed of the expander. This method provides an efficient rotor design with preliminary rotor geometrical parameters.
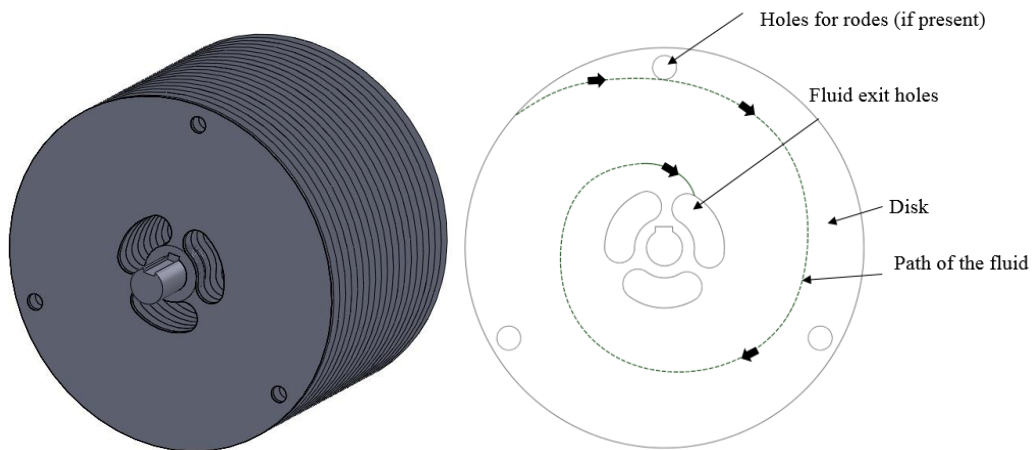
Figure 2.1 Rotor of Tesla bladeless expander

The design of the rotor is done based on the following flow parameters.

Inlet flow angle (α_o) and inlet velocity ratio

The fluid should enter from the stator to the Tesla rotor in a nearly tangential direction for the best performance. However, the design of the stator to have nearly tangential flow is difficult to obtain. Hence, researchers in the past have used stator with positive flow angle (greater than 5º) for practical reasons. Figure 2.2 shows the velocity triangle at inlet and exit of the Tesla rotor. The flow angles are measured with respect to tangential direction (along the disk tip velocity vector). The angle between absolute velocity vector with tangential direction is α_o, which is the angle which stator makes with the rotor (inlet flow angle). The angle between relative velocity vector with tangential direction is β_o i.e. relative flow angle. There are two cases shown in the Figure 2.2 based on the inlet velocity ratio (ratio between inlet tangential velocity and the disk tip velocity).

Case 1-3: This case is represented in Figure 2.2 by #1 and #3 velocity triangles with corresponding relative fluid path from outer to inner edge of the disk as 1-3. In this case, the inlet tangential fluid velocity, v_{to}, is higher than the disk tip speed (velocity ratio greater than 1). The relative velocity between fluid and disk, $v_{o.rel}$, is in the direction of the rotation of the disk. This positive relative velocity produces shear force on the disks which in turns results into torque. Similarly, in the exit velocity triangle when the exit tangential velocity is higher

than the disk tip velocity, it results into positive torque. However, energy is lost in the exit of the rotor due to higher tangential velocity of the fluid without exchanging work with the disk. In this case, the inner radius of the disk has to be carefully designed to recover maximum energy from the fluid. The typical relative fluid path is shown with dashed line1-3.
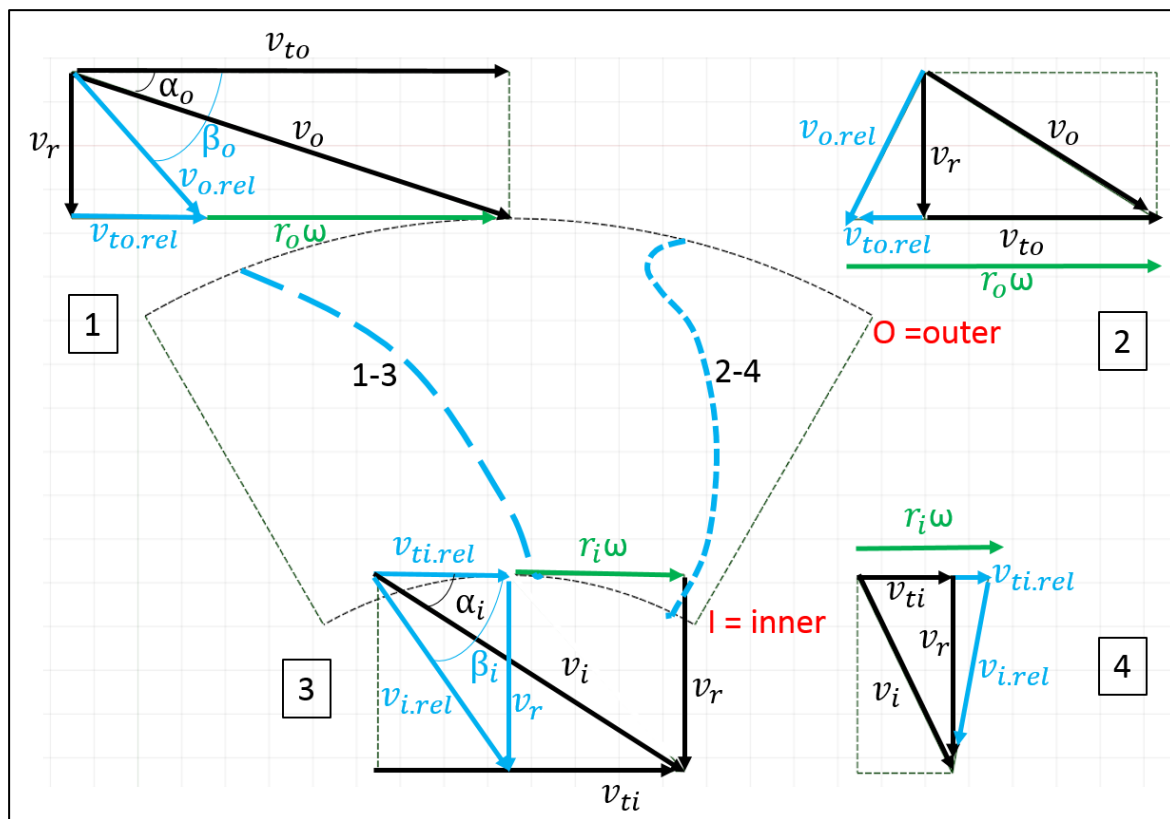
Figure 2.2 Velocity diagram for Tesla rotor

Case 2-4: This case is represented in Figure 2.2 by #2 and #4 velocity triangles with corresponding relative fluid path from outer to inner edge of the disk as 2-4. In this case, the inlet tangential fluid velocity, v_{to}, is lower than the disk tip speed (velocity ratio lesser than 1). The relative velocity between fluid and disk, $v_{o.rel}$, is in the opposite direction of the rotation of the disk. This creates reversal of the flow as shown by the typical relative path of the fluid in Figure 2.2. The flow reversal inside the disk is inefficient energy transfer process which generates the losses as it acts as the frictional viscous loss (direction of shear force is in opposite direction of rotation of disk). Similarly, at the exit of the rotor tangential velocity is lower than the disk tip velocity. In this case, the disk performs work on the fluid which is again the inefficient energy transfer process. These conditions must be avoided in the Tesla rotor to avoid

losses. Hence, for the best performance of the rotor, inlet flow angle should be as small as possible and the velocity ratio should be higher than 1.

Reynolds Number

Reynolds number defines the flow behaviour inside the gap between the disks i.e. laminar or turbulent. It is the ratio of inertia force and viscous force. There are several definitions of the Reynolds number used depending upon the characteristic length and the velocity consideration.

Reynolds number based on inlet tangential velocity (represented same as peripheral disk speed) and outer radius of the disk as the characteristic length:

$$Re_{r.\omega} = \frac{\rho . r_o . (r_o . \omega)}{\mu} \tag{2.1}$$

Reynolds number based on the inlet tangential velocity (represented same as peripheral disk speed) and the gap between disk as the characteristic length:

$$Re_{b.\omega} = \frac{\rho . b . (r_o . \omega)}{\mu} \tag{2.2}$$

Reynolds number based on the fictitious velocity (represented as the product of the gap between disks and angular velocity) and the gap between disk as the characteristic length:

$$Re_{b.b} = \frac{\rho . b . (b . \omega)}{\mu} \tag{2.3}$$

The Reynolds numbers based on tangential velocity studied in the literature does not provide any true insight into flow behaviour because these are defined based on the absolute tangential velocity. However, in the actual case, the velocity should be considered in the rotational frame of reference.

The fluid adherence to a wall (i.e. the "no-slip" condition) is the basic flow phenomenon behind the Tesla turbine operation. As the fluid gains the velocity of the wall over which it flows, a disk tends to gain the velocity of the fluid imparted over it. In the rotating frame of reference, i.e. reference system attached to the disk, the relative velocity between fluid and the disk is

very low. The radial component of the velocity, which pushes the fluid towards the centre of the rotor is also present in a rotating frame of reference. For the effective transfer of energy (momentum) of the fluid to the disks by acquiring the momentum of the fluid by the disk, the flow should be laminar[5]. The tangential velocity after entering into the rotor transfers the momentum to the disks and at some point, the speed of the rotor reaches the tangential speed of the fluid. This is the case when relative velocity between fluid and disk becomes zero and the only non-zero velocity component is radial velocity, responsible for the fluid flow through the turbine. This velocity should also be considered to define the Reynolds number.

Reynolds number based on relative velocity (difference between the fluid tangential velocity and disk velocity) and the gap between disk as the characteristic length

$$Re_{b.rel} = \frac{\rho.b.(v_{to} - r_o.\omega)}{\mu} \tag{2.4}$$

Reynolds number based on radial velocity:

$$Re_{b.rel} = \frac{\rho.D_h.(v_r)}{\mu} \tag{2.5}$$

The characteristic length can be presented by hydraulic diameter:

$$D_h = \frac{4.S}{P} \tag{2.6}$$

where S is the flow cross sectional area and P is the wetted perimeter.

$$D_h = \frac{4.(2.\pi.r.b)}{2.(2.\pi.r)} = 2b \tag{2.7}$$

Therefore, Eq. 2.5 becomes,

$$Re_{b.vr} = \frac{\rho.2.b.(v_r)}{\mu} \tag{2.8}$$

23

This Reynolds number is comparable with the Reynolds number with the flow in the pipe case. This will help to understand the flow behaviour inside the rotor of the Tesla turbine i.e. laminar flow if $Re_{b.vr} < 2000$, transition if $2000 < Re_{b.vr} < 4000$ and turbulence if $Re_{b.vr} > 4000$.

Rice [5] has performed the analytical investigation of the Tesla rotor using Reynolds number based on fictitious velocity (Eq.(2.3). Although this Reynolds number does not give information qualitatively, the reasonable range for the higher performance of the rotor is recommended between 5 and 8.

Boundary layer thickness

The fluid flow between two disks exhibits boundary layers in tangential and radial direction based on the tangential and radial velocity components as shown in Figure 2.3. Therefore, these two components of velocity also generate shear stress on the wall due to the boundary layer. The tangential component of shear stress is responsible for the torque on the rotor while the radial component of the shear stress merely contributes to viscous frictional loss. Shear stress on the wall, in general, is given by,

$$\tau_w = \mu \frac{du}{dy} \tag{2.9}$$

Where, du/dy is the velocity gradient normal to the wall.

Figure 2.3 also shows the flow regions between disks. The fluid after entering inside the gap between the disks forms a boundary layer on the disk wall. The core region, which is an inviscid region, forms when the gap between two disks is too large for the boundary layer to merge. The core flow has a velocity similar to the inlet velocity of the fluid and it does not participate in the transfer of momentum to the disk wall.
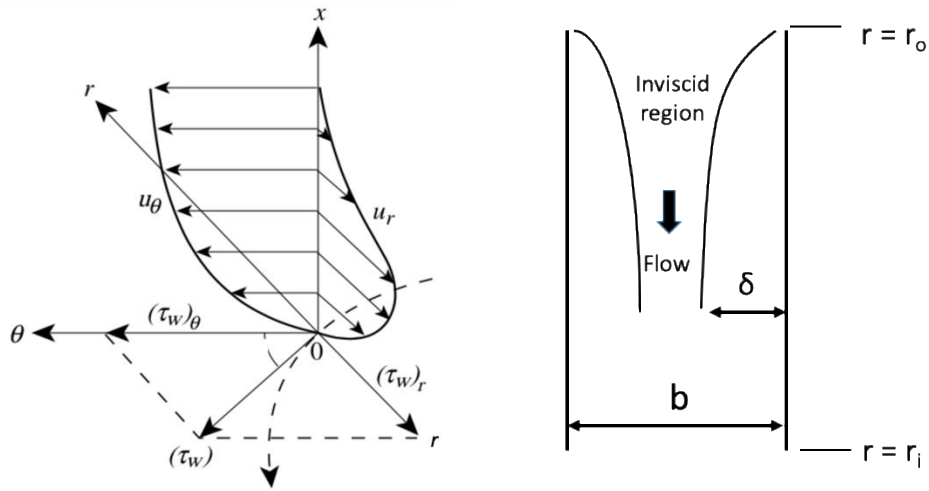
Figure 2.3 Boundary layer development due to tangential velocity, u_θ and radial velocity, u_r

The gap between two disks being an important design parameter greatly depends on Reynolds number, boundary layer thickness, the kinematic viscosity of the fluid and the rotational speed of the disks. The gap between the disks is evaluated considering both the boundary layers i.e. tangential and radial direction. There is an optimum gap that ensures effective energy transfer between fluid and disks (boundary layer in tangential direction) and to ensure positive flow through rotor with less viscous frictional loss (boundary layer in the radial direction). Boundary layer thickness for laminar flow [41] can be evaluated as follows,

$$\delta = 5. \sqrt{\frac{v.l}{U}}$$
(2.10)

where, l is the length of the channel and U is the free stream velocity outside boundary layer. In case of tangential direction, $l = 2\pi r_o$ and $U = v_{to}$. In case of radial direction, $l = r_o\text{-}r_i$ and $U = v_r$.

Breiter and Pohlhausen[42] used a similarity parameter that determines the shape of the radial and tangential flow profiles between the disks. Figure 2.4 shows the generalised profile for the radial flow. It can be seen that the profile shape depends on the similarity parameter, P which is defined as follows,

$$P = \frac{b}{2} \cdot \sqrt{\frac{\omega}{\nu}} \qquad\qquad (2.11)$$
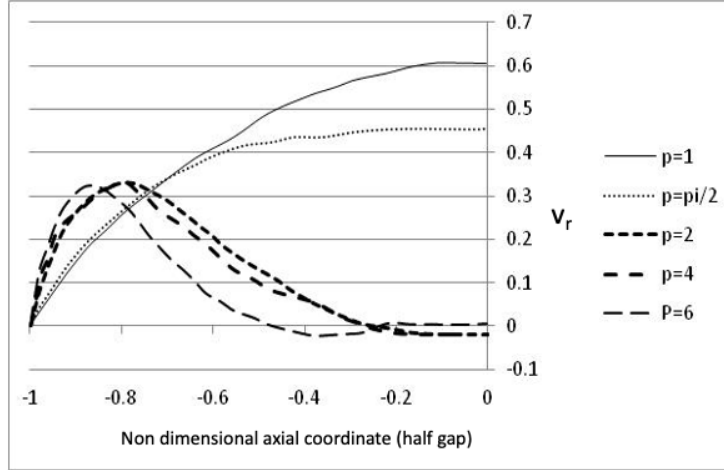
Figure 2.4 Radial velocity vs non dimensional axial coordinate (half gap) for different values of P [42]

We can observe in Figure 2.4 that two maxima appear close to the walls, which means that disks are spaced too apart. For instance, there is backflow at the centre of the disks at $P = 2,4$ and 6. It is preferred to have a profile that gives acceleration at the centre. However, there is a limit to bringing the disks closer together because the friction surface for the radial profile becomes very high. A profile that is just deviating from a parabolic shape is considered to be optimum[51] i.e. flow conditions should be such that P value appears close to "π/2".

There is a similar parameter studied by some researchers, Ekman Number, which is considered to be crucial for velocity profile between the gap and the efficiency of the Tesla rotor. Ekman number is defined as the ratio of viscous forces to the Coriolis forces or the ratio of half gap to the boundary layer thickness. Ekman number is given by,

$$Ek = \frac{\frac{b}{2}}{\delta} = \frac{b}{2} \cdot \sqrt{\frac{\omega}{\nu}} \qquad\qquad (2.12)$$

Ekman number is identical to the Eq. (2.11) and the recommended range for high rotor efficiency is 1- 2.

From the above analysis, one can estimate, as a rule of thumb, gap between the disks is in the neighbourhood of double the boundary layer thickness, for Tesla expanders.

Flow parameter

Flow rate per disk gap is another important parameter to be evaluated for the maximum efficiency of the Tesla rotor. Rice[5] has performed analytical calculations for non-dimensional flow rate and its impact on the efficiency with respect to velocity ratio and radius ratio.

Following are the recommended values for flow rate parameter, radius ratio and velocity ratio (inlet fluid tangential velocity to disk tip velocity) at disk tip.

Non dimensional flow rate parameter for optimum flow per disk gap:

$$q_f = \frac{Q}{\omega.r_o^3} \sim 0.00001 - 0.0001 \tag{2.13}$$

equivalent to:

$$U_0 = \frac{Q}{2.\pi.\omega.r_o^2.b} \sim 0.1 - 0.25 \tag{2.14}$$

Velocity ratio:

$$VR = \frac{v_{to}}{\omega.r_o} = \ \sim 1.1 - 1.3 \tag{2.15}$$

Radius ratio:

$$RR = \frac{r_o}{r_i} = \ \sim 2 - 5 \tag{2.16}$$

Once the flow rate per gap is calculated, number of disks can be estimated based on the total flow available at the inlet of the turbine.

Torque per disk can be evaluated using Euler's equation for turbine,

$$T = m.(r_o v_{to} - r_i v_{ti}) \qquad (2.17)$$

Power per disk is given by,

$$P = T.\omega \qquad (2.18)$$

Rotor design algorithm (0-D)

Based on the parameters discussed in the above section, an algorithm to preliminary design the rotor has been established, as shown in Figure 2.5. This algorithm gives the geometric and flow parameters for the turbine to be selected at design condition. The fine tuning of the geometry may be required mainly for the design case and feasibility with respect to manufacturing of the rotor.

Case study – 3 kW air expander rotor design

3 kW expander for which detailed numerical and experimental investigation is performed in later paragraphs, is considered for the case study of rotor design. The generator has rated rotational speed of 40000 rpm with 3 kW power, which is considered a starting point for the analysis.

    a. The outer diameter for the rotor is selected to limit the Mach number to 1 or less. Peripheral velocity of 250-300 m/s is taken as a starting point. The outer diameter of 120 mm is calculated for tip speed of $\sim$ 250 m/s.

    b. Total absolute pressure at the rotor inlet, P_{t0} , is considered 2 times the dynamic pressure due to fluid velocity at rotor periphery. At this total pressure at rotor inlet, density of 2 kg/m^3 is calculated for the temperature of 300K.

    c. Reynolds number, $Re_{b.b}$, of 4 is selected for the calculation of gap between disks. Using the fluid thermodynamic properties, gap between disks comes out to be around 0.1 mm.

    d. As a check for P, similarity parameter according to Eq. (2.11) is evaluated which is $\sim$1. This is close to the recommended value of $\pi/2$

    e. The fluid being low density, inner diameter is calculated using diameter ratio 2. The diameter ratio of 2 is chosen considering the outlet area blockage due to

shaft and discrete exhaust holes on the disks, as shown in Figure 2.1. The calculated outlet diameter for the rotor is 60 mm.

f. The inlet tangential velocity is calculated using optimum velocity ratio of 1.2. The calculated inlet tangential velocity is 300 m/s.

g. Radial velocity is calculated by setting inlet flow angle (α_o) of 1-2 degree for near tangential flow at the rotor. In this case, for the inlet flow angle of 1.36 degree, we get radial velocity of 7 m/s.

h. Using the radial velocity, mass flow and flow rate at the periphery of the disks is calculated which is 0.45 g/s and 0.000283 m^3/s per gap respectively.

i. Flow rate is checked with respect to flow rate parameter, Eq. 2.13: the calculated flow rate parameter in this case is 0.0003 which is in the acceptable range.

j. Torque per disk is calculated using Euler's Eq. (2.17), which is 0.006487 Nm, and power per disk, calculated by multiplying torque with angular velocity, is 27 W.

k. Number of disks of 120 is selected to have a total power higher than 3 kW (being upper limit power, in practice power will be less than 3 kW). The power and mass flow for 120 disks is 3.26 kW and 54 g/s.

l. The efficiency calculated using the ratio of output power and inlet isentropic power is 85.3%, that is the expected rotor-only efficiency.

The design of rotor is performed for various inlet flow angles (α_o) i.e. with different radial velocities which leads to different mass flow per gap. The performance of 0-D design is compared with 2D CFD analysis in the following section.
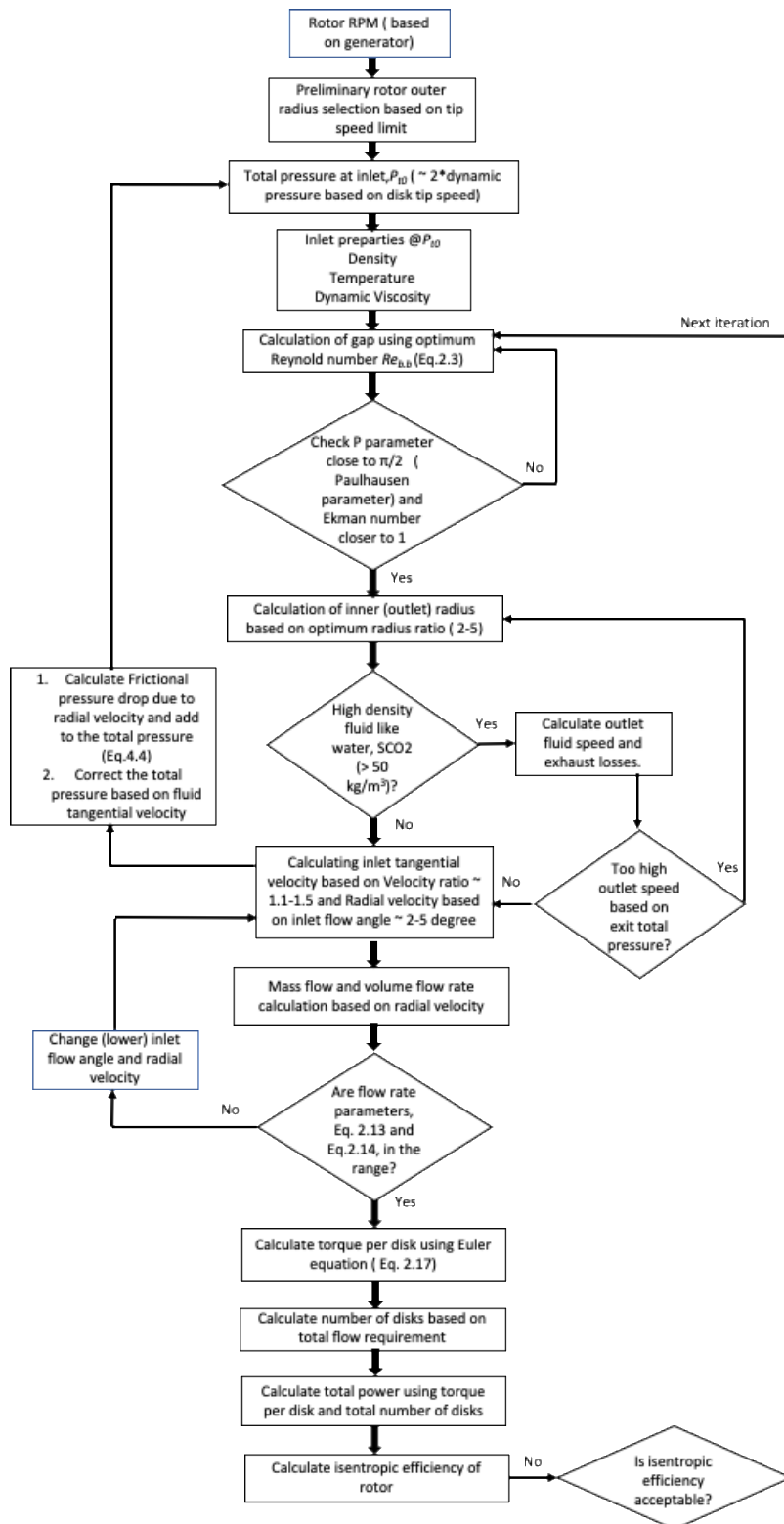
Figure 2.5 0-D algorithm for the preliminary design of the rotor

2-D Rotor of 3 kW Tesla expander – 2D CFD

In this section 2-D CFD of the rotor for the 3-kW expander with air is performed. The geometry and mesh are shown in Figure 2.6. The hexahedral mesh is used and inflation layers on the wall of the disks are used to accurately capture the boundary layer phenomena. The Y+ on the wall is maintained ~1. A mesh sensitivity analysis is performed for different number of elements and output variables are monitored so that optimized mesh can be selected.
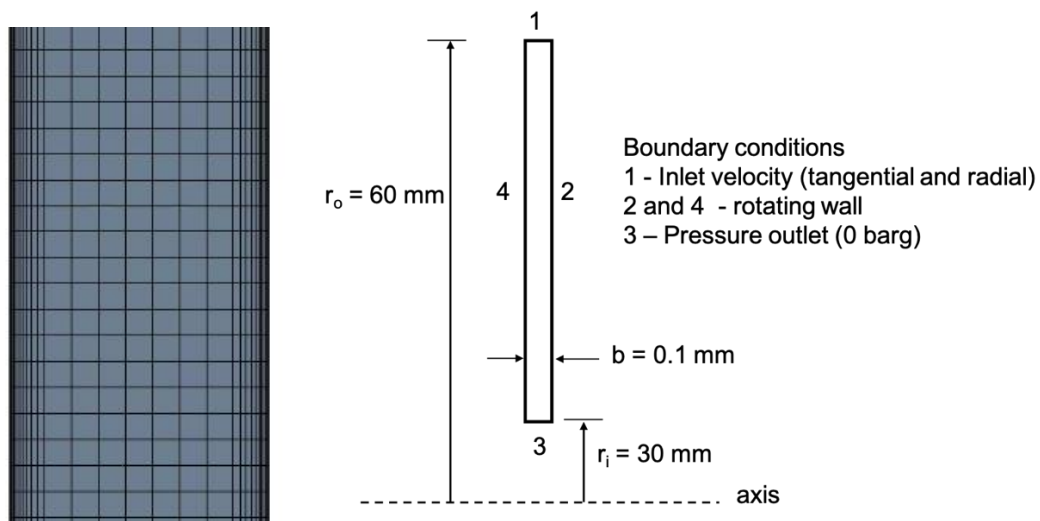
Figure 2.6 Mesh, geometry and boundary conditions for 2-D CFD

Figure 2.7 shows the mas flow and output variables versus mesh size. We can see that the mass flow remains unchanged at the mesh size greater than 7000. However, outlet velocity and torque remain unchanged at the mesh size greater than ~14000. Based on the sensitivity of outlet variables, mesh size of ~15000 is selected for this analysis.

A steady state, incompressible, and air with ideal gas model is used for the simulation. The k-w SST turbulence model is used for the accuracy to capture shear stresses at wall. The simulation is run with double precision for different mass flow per gap which is defined by inlet velocity boundary condition – tangential velocity, radial velocity and axial velocity (0 m/s).
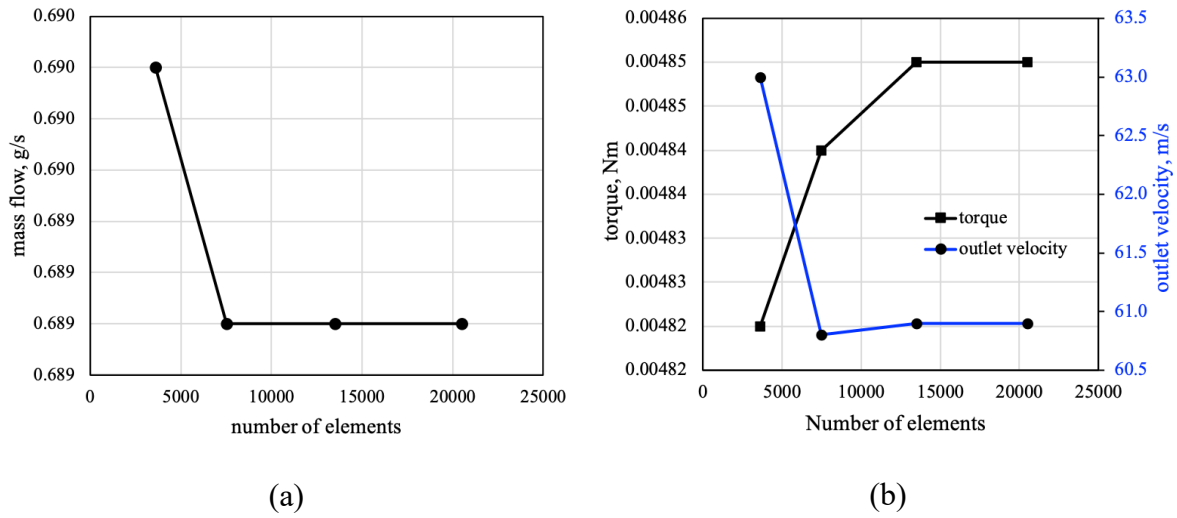
Figure 2.7 Mesh sensitivity analysis (a) mass flow versus number of elements (b) torque and outlet velocity versus number of elements
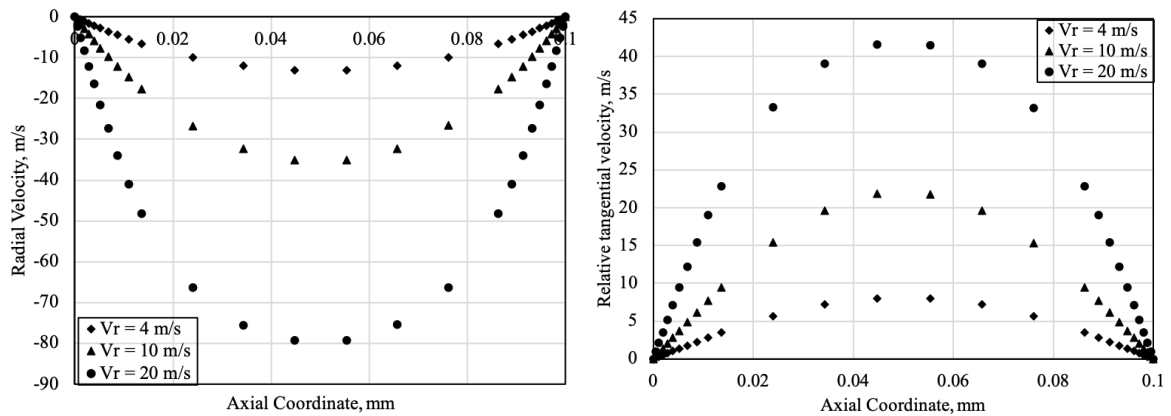
Figure 2.8 Radial velocity and relative tangential velocity profile at r = 35 mm for different inlet radial velocity i.e. mass flow

Figure 2.8 shows the radial and relative tangential velocity profiles for different mass flows (represented in terms of inlet radial velocity) between the gap of disks at a radius of 35 mm. It can be seen that that the velocity profile doesn't show any inflection or reverse flow. The parabolic profile both in the radial and tangential directions ensures the good design of the rotor. The relative tangential velocity is lower at lower mass flow and it increases at higher mass flow. The higher relative velocity between fluid and disks means lower energy transfer

and low performance of the rotor. It is important to choose the relative tangential velocity as low as possible while maintaining the parabolic profile shape throughout the disk length.

(a)   (b)
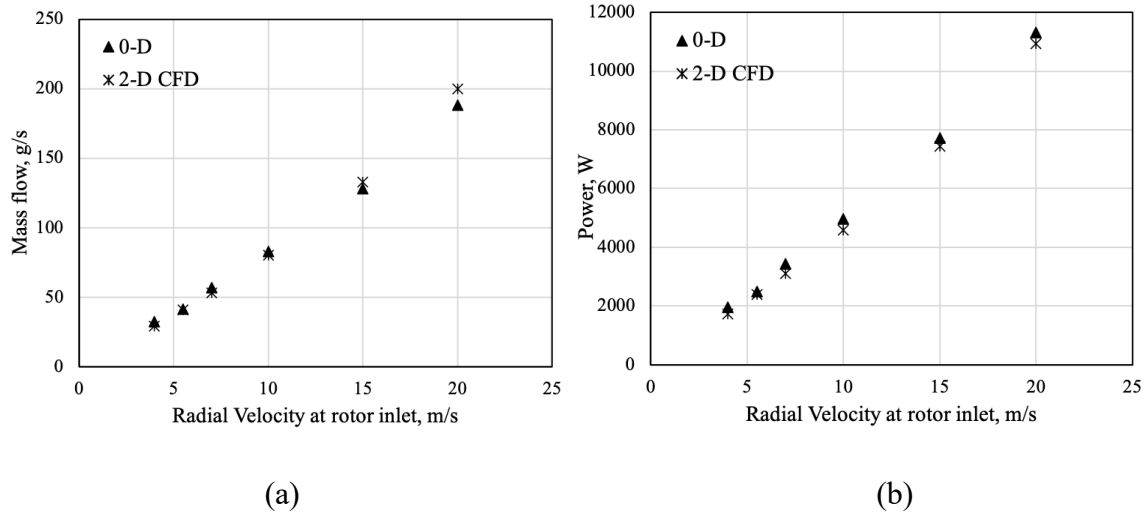
Figure 2.9 Comparison between 0-D and 2-D CFD analysis. (a) mass flow versus radial velocity at the rotor inlet; (b) turbine power versus radial velocity at the rotor inlet for 120 disks

(a)   (b)
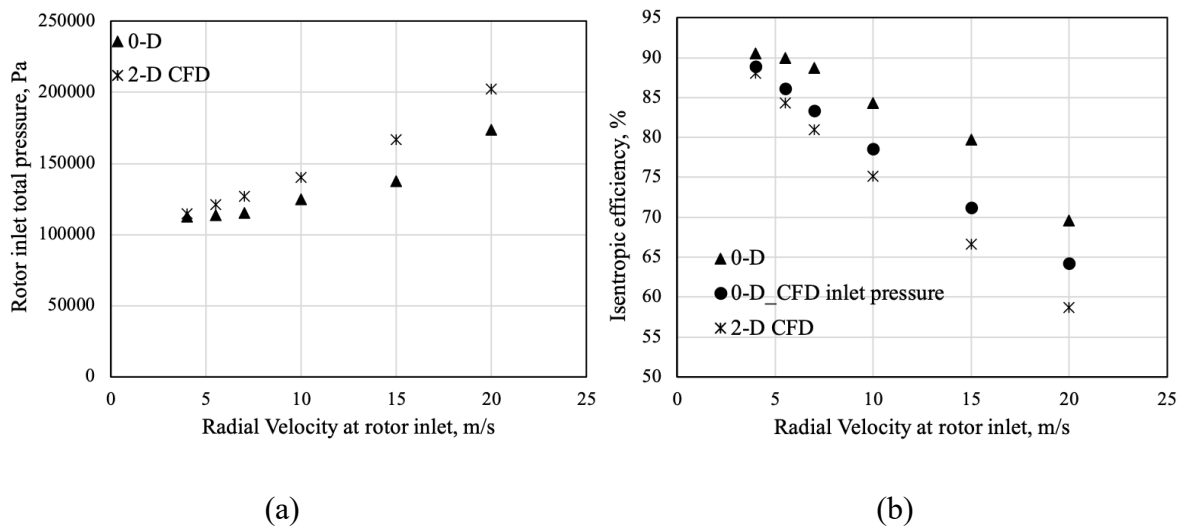
Figure 2.10 Comparison between 0-D and 2-D CFD analysis. (a) rotor inlet total pressure versus radial velocity at the rotor inlet; (b) isentropic efficiency versus radial velocity at the rotor inlet for 120 disks

The comparison between 0-D and 2-D models are shown in the Figure 2.9 and Figure 2.10. The graphs are plotted with respect to inlet radial velocity as this is the fixed parameter in both the simulations. The mass flow from 0-D calculation agrees well with the 2D CFD results at lower inlet radial velocities. The difference at higher inlet radial velocities is due to the approximate inlet density of the fluid. The correction of a density involves the good prediction of inlet total pressure which is the most difficult parameter to calculate by 0-D as it depends on several other factors. The high error in the prediction of pressure at higher inlet radial velocity conditions can be seen in the Figure 2.10 (a). There is a good agreement between turbine power with slight overprediction in case of 0-D model as it does not take into account the losses of energy transfer between fluid and disks. The effect of a bad prediction of inlet total pressure can be seen in the Figure 2.10 (b) on the isentropic efficiency. There are two plots for 0-D for isentropic efficiency – one with rotor inlet total pressure derived from 0-D model and other with rotor inlet total pressure taken from 2D CFD. We can see that efficiency prediction of 0-D model is pretty good and within the acceptable range. The 0-D model efficiency curve follows the similar trend as that of 2-D CFD but with overestimating the efficiency at higher inlet radial velocity.

The 0-D model discussed above is a promising design approach to preliminary design the Tesla rotor and then further fine-tuning could be done based on the CFD simulations. The expanders discussed in this study are designed using the 0-D model approach and, then, they are further tuned for the flow parameters keeping the geometrical parameters the same.

2.1.2 Stator

The function of the stator is to provide uniform tangential velocity at the periphery of the rotor of Tesla expanders. Researchers have used traditional design of nozzles with convergent or convergent-divergent profile to attain subsonic to supersonic flow regimes. The rotor analysis is assumed to have full peripheral admission. However, if conventional nozzles are used, they have to be arranged in discrete manner around the periphery of the rotor. This leads to partial admission of fluid to the rotor which incurs additional losses.

One of the important parameters is nozzle angle which affects the tangential flow entry to the rotor. Highly tangentially rotor makes nozzle throat very narrow and introduces additional losses in the stator-rotor cavity.

In this study three different configuration of nozzles are studied both experimentally and numerically.

1. Convergent divergent nozzle for 100 W air expander
2. Convergent nozzle for 3 kW expander
3. Convergent nozzle for 1 kW water expander.

2.1.3 Exhaust Diffuser and Collector

The flow discharged from the turbine rotor has certain amount of kinetic energy. In case of Tesla turbine, the exhaust kinetic energy has very high swirl component and lower axial component due to the nature of rotor (without any vanes). The exhaust loss due to the lost kinetic energy can be very high particularly in case of high-density flows like water or sCO2. In this case, the kinetic energy recovery becomes a significant aspect of the design of the turbine.

The exhaust kinetic energy treatment or its recovery has not been discussed in the literature for Tesla turbines. The conventional axial diffuser will not be sufficient as it works best for the axial velocity component. In order to recover the swirl velocity component, for the first time, radial diffusers are considered in this study.

Figure 2.11 shows the 2-D CFD of the Tesla rotor with radial and tangential velocity plots. It can be seen that the fluid has very high tangential velocity and outward radial velocity at the exit of the rotor. The resultant of the two velocities create flow in radially outward (away from axis) direction with high swirl. Hence, the axial diffuser will not be effective in this case and radial diffuser will diffuse the swirl flow as well as radial flow effectively.

In this study, radial diffuser design is applied for water expander case. The high density and high velocity of water at the exit contributes significantly to the exit loss. Radial diffuser is designed to effectively convert the kinetic energy into static pressure.
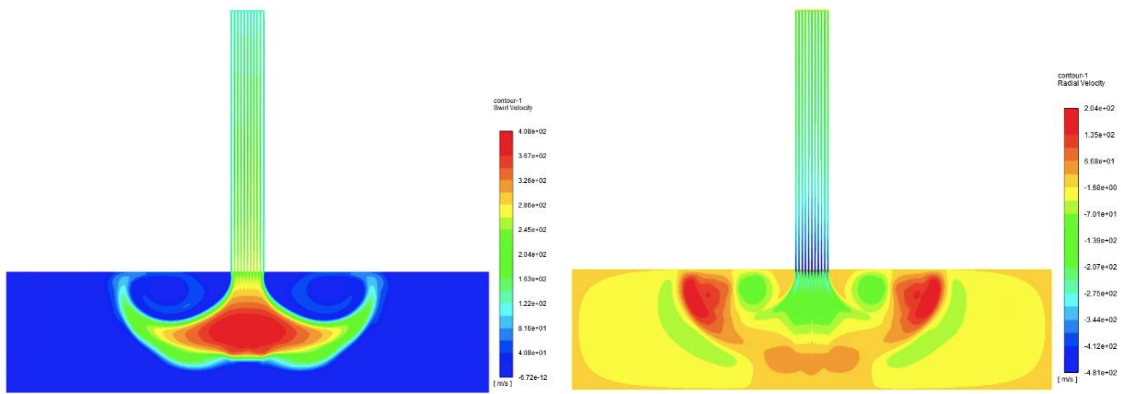
Figure 2.11 2-D CFD of Tesla expander with exhaust passage showing tangential velocity (left) and radial velocity (right) plots

Figure 2.12 shows the schematic of a radial diffuser. For higher diffuser efficiency, transition radius between axial and radial direction is 36% of the inlet pipe diameter [43]. Maximum recovery from diffuser is obtained from width to inlet pipe diameter ratio of 0.15. It is also suggested to avoid any deceleration in the transition region to avoid flow separation. The design and 3D CFD of radial diffusers are discussed in the water expander section 2.2.3.
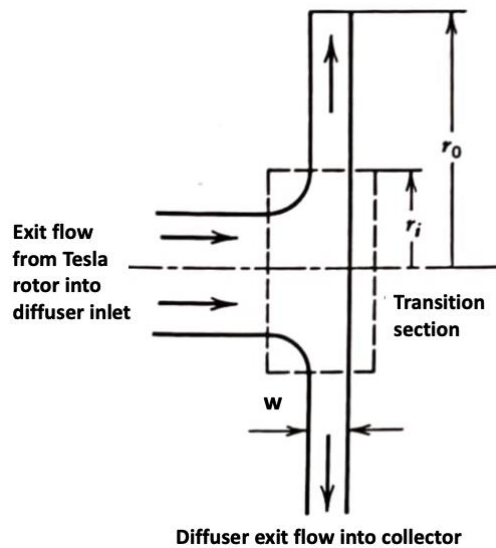
Figure 2.12 Radial diffuser configuration

2.2 3D Numerical Investigation

Inside the Tesla rotor, the Navier-Stokes equations governing fluid flow can be solved by analytical method or numerical approach. The closed form analytical solution by some approximation has been obtained in the past, which characterises the fluid flow inside the Tesla rotor, thanks to its laminar behaviour. This approach is the fastest way to design the optimum Tesla rotor for a design condition. However, for the complete understanding of fluid flow phenomena between stator and rotor, which is the main source of losses in the expander, it is crucial to perform 3D CFD simulations.

In this study, the commercially available CFD software Ansys Fluent 19 is used to solve the Navier-Stokes equations, both for 2D and 3D simulations in the computational domain.

The set of equations are as it follows,

The mass conservation equation,

$$\frac{\partial \rho}{\partial t} + \nabla.(\rho \bar{v}) = 0 \tag{2.19}$$

Eq. (2.19) is the general form of conservation of mass equation and valid for both incompressible and compressible flows.

Conservation of momentum in an inertial reference frame is described by

$$\frac{\partial(\rho\bar{v})}{\partial t} + \nabla.(\rho\bar{v}\bar{v}) = -\nabla p + \nabla.(\bar{\tau}) \tag{2.20}$$

Where $\bar{v}$ is velocity vector, p is static pressure and $\bar{\tau}$ is stress tensor (described below)

The stress tensor $\bar{\tau}$ is given by

$$\bar{\tau} = \mu\left[(\nabla\bar{v} + \nabla\bar{v}^T) - \frac{2}{3}\nabla.\bar{v}\,I\right] \tag{2.21}$$

Where μ is the molecular viscosity, I is the unit tensor and the second term on the right hand side is the effect of volume dilation.

Energy Equation is given by

$$\frac{\partial}{\partial t}\left[\rho\left(e + \frac{v^2}{2}\right)\right] + \nabla.\left[\rho\bar{v}\left(e + \frac{v^2}{2}\right)\right] = \nabla.(k\nabla T) + \nabla.(-\rho\bar{v} + \bar{\tau}.\bar{v}) \qquad (2.22)$$

The term on the right of the equation side $\nabla.(\bar{\tau}.\bar{v}))$ is the viscous dissipation term which in Tesla expander rotor case represents viscous work. In the equation potential energy is neglected. An "e" in the first term contains internal energy and in the second term contains enthalpy.

The viscous term is important in the Tesla expanders as the work transfer takes place through boundary layer viscous force.

To see the low Reynolds number effect, which is the case for Tesla expander rotor, let us consider the Lagrange formulation for the momentum equation,

$$\rho\frac{D\bar{v}}{Dt} - \nabla p + \mu\nabla^2\bar{v} \qquad (2.23)$$

If we define Reynolds number as following and substitute in Eq. (2.23) to make it non-dimensional, we obtain Eq. (2.25).

$$Re = \frac{\rho.l.v}{\mu} \qquad (2.24)$$

$$Re\,\frac{D\bar{v}}{Dt} = -\nabla p + \nabla^2\bar{v} \qquad (2.25)$$

We can infer from the Eq. (2.25) that at low Reynolds number pressure term is balanced by viscosity term. The viscous effects become more dominant. In other words, the momentum equation is governed by pressure gradient and viscosity. In a way, time derivative vanishes from the Eq. (2.25) for very low Reynolds flow. Hence the flow inside the rotor of Tesla expander is "near reversible" which means the efficiency of the Tesla rotor is not affected in reverse mode, i.e. compressor mode.

One of the reasons for the high efficiency of the Tesla rotor is laminar flow inside the rotor. However, there is large influence of the stator on the inflow conditions of the rotor, which needs to be studied by 3D CFD simulations.

To evaluate the performance of the expander, certain parameters are developed to define the efficacy of the rotor and stator.

Power is calculated using torque of the rotor and angular velocity as:

$$P_{CFD} = \tau.\omega \tag{2.26}$$

Mechanical efficiency of total-to-static $\eta_{CFD.tot.st}$, computed as it follows,

$$\eta_{cfd.tot.st} = \frac{P_{CFD}}{C_p T_{in.tot}\left(1-\frac{1}{\varepsilon^{\frac{k-1}{k}}}\right)\dot{m}} \tag{2.27}$$

Specific heat at constant pressure, c_p and heat capacity ratio, k are considered constant with temperature. For air, $c_p = 1.005$ kJ/kg K and $k = 1.4$ are used.

The expansion ratio ε is given by

$$\varepsilon = \frac{p_{in.tot}}{p_{e.st}} \tag{2.28}$$

The degree of reaction of the expander is also numerically computed in order to see the expansion partition in the rotor and the stator. It is defined as the ratio of static pressure drop in the rotor to the static pressure drop in the expander.

$$\psi = \frac{p_{rot.in.s}-p_{rot.out.s}}{p_{noz.in.s}-p_{rot.out.s}} \tag{2.29}$$

2.2.1 Air 100W Tesla Expander Prototype

Geometry and computational domain
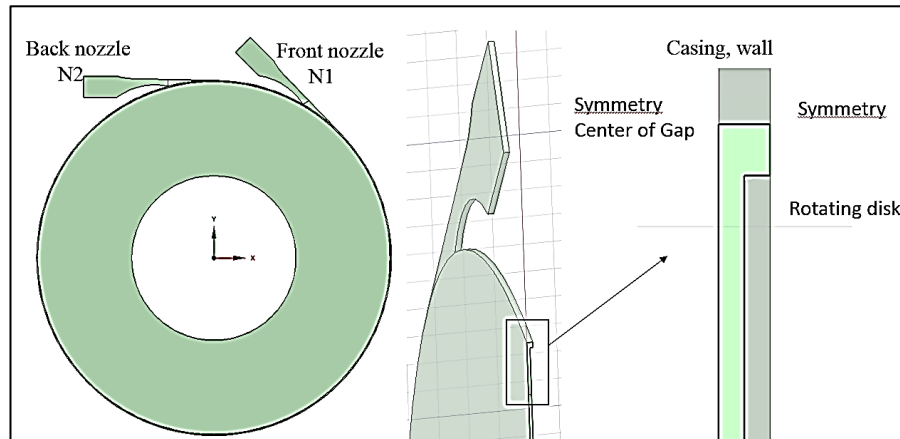
Geometric Parameters

Outer diameter of disk, mm	64.5
Inner diameter of disks, mm	30
Number of nozzles	2
Gap between disks, mm	0.2
Disk thickness, mm	0.2
Number of disks	10
Nozzle angle, degree	2.2

Figure 2.13 Geometry and boundary conditions used for CFD simulation

A partial 3D model is built to retain sufficient accuracy at acceptable computational cost, which consists of nozzle, casing and disk. The geometric parameters and model used for this simulation is shown in Figure 2.13. In these models, half disk and half gap are simulated for the rotor. Such configuration greatly reduces computational efforts without compromising on the quality of the results.

Mesh and boundary conditions

A 'mapped hexahedral meshing' for the model using commercial Ansys ICEM 19.2 software is created. Mesh sensitivity is carried out by changing the grid distribution in the stator and the rotor. The grid distribution is different in all three coordinates (axial, radial and tangential). The grid distribution in axial direction is non-uniform to capture wall physics accurately. To resolve the viscous sub layer, y+ between 0 to 1 has been maintained. Mesh sensitivity analysis

is shown in Table 2.1. As shown in Figure 2.14, a mesh is selected for the model for which no significant change in the output parameters such as outlet tangential velocity, torque on disk and outlet temperature is reported. The grid size of #3 is selected for the simulation.

The following boundary conditions are used in the CFD simulation of this study : (a) at the inlets of both the nozzles, total pressure and total temperature; (b) at the outlet, zero static pressure; (c) disks are considered to be rotating walls with no slip condition; (d) stationary walls of the casing and the nozzles are given no slip wall condition; (e) symmetry boundary condition at the centre of the gap between disks and at the centre of disk, as shown in Figure 2.13.

Table 2.1 Grid independence tests

Mesh model #	# of Nodes	# of elements	Outlet Total temperature, K	Torque, Nm	velocity outlet, m/s
Grid distribution variation in rotor					
1	2,6E+06	2,7E+06	281,41	0,001533	60,60
4	1,7E+06	1,8E+06	281,45	0,001534	60,60
3	1,4E+06	1,5E+06	281,45	0,001535	59,66
4	4,3E+05	4,7E+05	281,48	0,001539	58,55
Grid distribution variation in stator					
1	4,3E+05	4,7E+05	281,48	0,001539	58,55
2	8,1E+05	8,8E+05	281,58	0,001527	60,72
3	1,1E+06	1,2E+06	281,43	0,001539	60,72
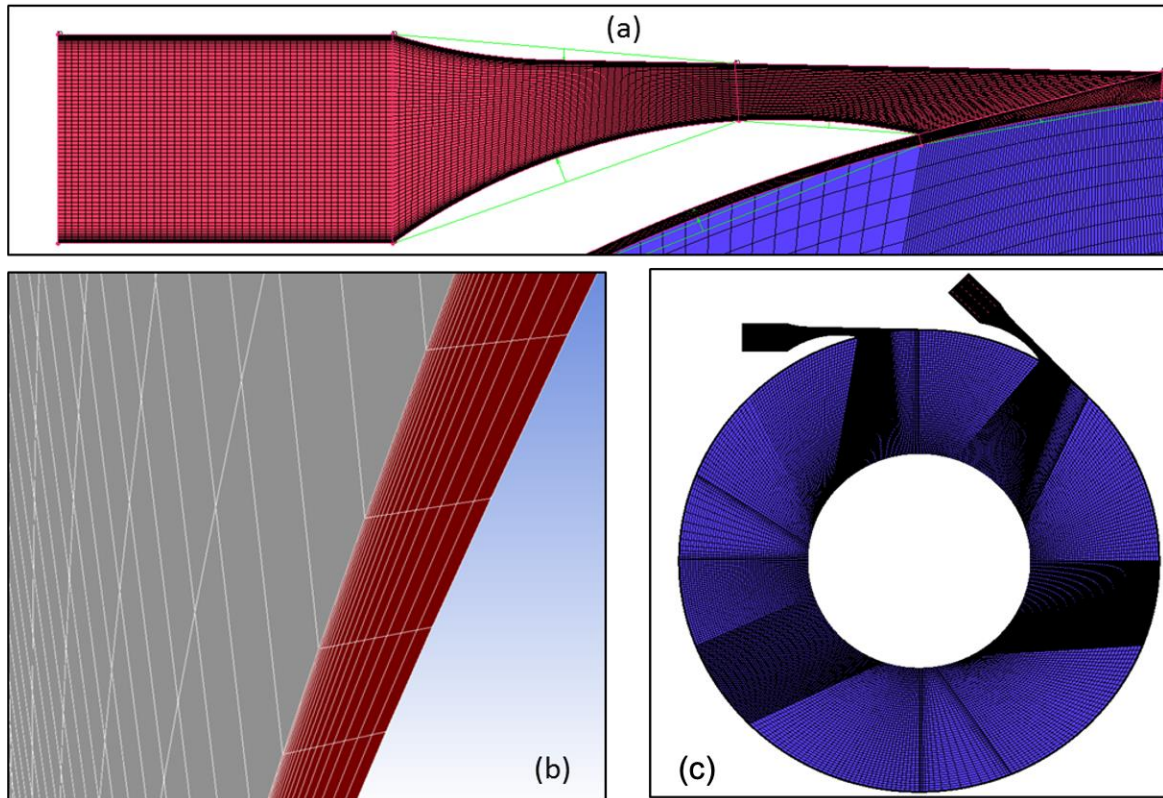
Figure 2.14 Grid distribution in: (a) nozzle; (b) half gap between disks; (c) entire model

Numerical solution conditions

The nozzle being convergent-divergent, supersonic flow at the outlet of the nozzle is predicted. Therefore, CFD simulation for steady, turbulent and compressible supersonic flow is performed. For this purpose, 3D, double precision, density-based solver in Fluent 19 is used with energy equation model and transition SST (shear stress transport), to accurately resolve flow at the wall. Compressed air with ideal gas is used as fluid domain. Convergence for residual is tracked till 10^{-6} along with the convergence of following parameters: outlet tangential velocity, outlet total temperature, torque on the disks and mass flux.

Results and Discussion

In this section, the performance of the Tesla turbine simulated with stator and rotor for 100W expander is presented. The stator consists of convergent divergent nozzle, which feeds the high velocity fluid to the rotor. The CFD is performed at various operating points for different

speeds and mass flows. Figure 2.15 presents the comparison between experimental and CFD simulation results. Experimental set-up is described later in section 3.1. Here, focus is on numerical results due to the design geometry previously defined. Figure 2.15 (left) shows the mass flow versus the absolute nozzle inlet pressure. All the speeds are plotted on the same graph to also see the dependence of the rotational speed on the mass flow. We see that there is good agreement between CFD and experimental data. It also shows that there is no significant effect of rotational speed on mass flow. Figure 2.15 (right) presents the power characteristics as function of mass flow. In the CFD model, ventilation losses, leakage, mechanical and exhaust losses are not captured. The experimental power loss due to ventilation and mechanical losses has been subtracted to CFD power curve. This gives us the closest comparison possible between experiment and numerical data. Difference of power between experiment and numerical results is due to exhaust loss and leakage present in the expander (and bearings, supposedly of one order of magnitude lower). In this expander there is no anti-leak system installed and hence, it is estimated to have higher leakage flow around 30 to 40% of main flow[44]. The difference in power can be seen lower at low mass flow and increasing at high mass flow points. It means that the leakage flow is high at high nozzle inlet pressure or mass flow.
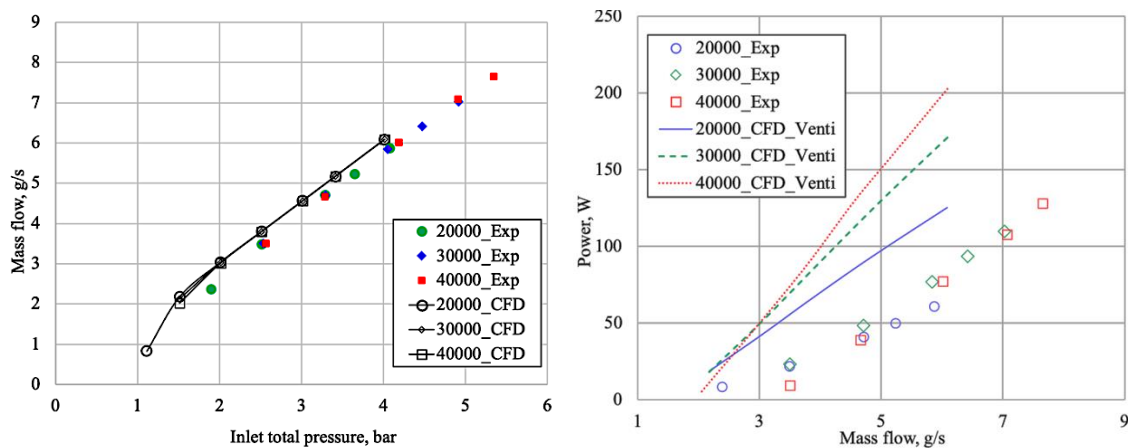
Figure 2.15 CFD and experimental results comparison of air 100W expander; (left) mass flow versus nozzle inlet pressure-abs, (right) expander power versus mass flow

We can observe that at low mass flow, the trend of power lines with respect to rotational speed is obtained by numerical results showing reversal point on the power lines. This trend can be

observed in both numerical and experimental results. The lower mass flow leads to lower nozzle exit velocity at same rotational speed. As the mass flow is decreased, the velocity ratio of nozzle-exit fluid velocity to the disk tip velocity decreases. When the velocity ratio drops less than 1, there is reversal of tangential velocity and energy transfer efficiency decreases significantly leading to lower power and efficiency.

Apart from the external losses, 3D numerical method helps to characterize the nozzle and rotor losses both qualitatively and quantitatively, which is difficult by experimental methods.

Figure 2.16 shows the total to static efficiency and power of the turbine versus coefficient of expansion obtained with CFD simulations. We observe that for all rotational speeds, peak of the efficiency shifts towards lower coefficient of expansion, i.e. at lower mass flow rate. Performance of the turbine is better with higher rotational speeds. The expander efficiency curve follows the rotor only efficiency curve showing higher performance at lower mass flow, which means that the stator losses have no significant influence on the trend in the overall efficiency curve. Moreover, the power curves are varying linearly showing no peak. This demonstrates that the turbine power is strictly a function of mass flow or the inlet pressure of the expander.
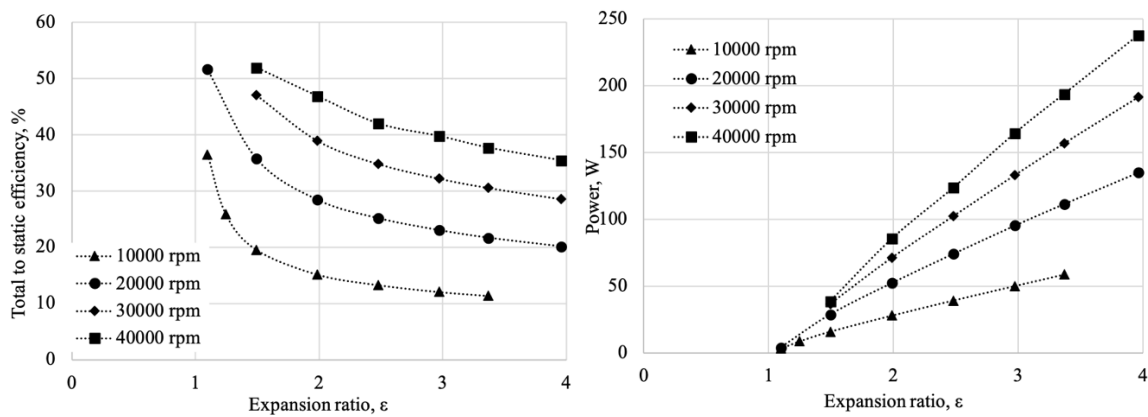
Figure 2.16 CFD performance curves for air 100W expander; (left) total to static efficiency and (right) power, versus expansion ratio at different rotational speeds

There is a significant influence of rotational speed on the performance of the turbine. It can be seen that expander performance is better at higher rotational speeds if the velocity ratio (fluid velocity / disk tip velocity) is maintained > 1. Analytically, it has been shown in the literature

that the Tesla machines perform best at higher rotational speed due to higher number of spiral turns taken by fluid inside the rotor which will be discussed in the subsequent sections through stream-plots. In the following section we illustrate the fluid dynamic principles inside stator and the rotor through numerical simulations.

Nozzle: Stator plays a significant role in the performance of a Tesla expander. In the air 100 W expander, stator is a convergent-divergent nozzle. The flow at the exit to the nozzle varies from subsonic to supersonic. The exit Mach number (mass averaged) for the various inlet nozzle pressure is indicated in Table 2.2.

Table 2.2 Mach number at nozzle outlet at different inlet pressures

Total inlet nozzle pressure, bar	Mach number	
	10000 rpm	40000 rpm
3.4	1.60	1.56
3.0	1.56	1.44
2.5	1.47	1.34
2.0	1.33	1.18
1.5	1.05	0.78

The supersonic flow between the nozzle and the stator-rotor cavity leads to possible shock waves. Shock waves play an important role in the performance of the turbine, hence their detection from experimental or numerical analysis is a demanding research. Shock waves may cause some of the following aerodynamic phenomena: loss of total pressure drop, interaction with other flows such as boundary layer flows to create another flow structure, and sudden change of properties like pressure, Mach number, density, temperature, entropy, etc.

Figure 2.17 shows the total pressure loss coefficient from nozzle inlet to the outer periphery of the rotor. This tremendous total pressure drop is due to the losses at the stator-rotor interaction and the shock waves due to supersonic flow. According to Figure 2.17, total pressure drops from inlet of nozzle till rotor inlet for 2.5 bar inlet pressure reaches up to 45% at 10000 rpm. This 45% drop in total pressure is a complete loss before the rotor. For lower inlet pressure at the nozzle, Mach number decreases, and the shock waves becomes weaker, hence the total pressure drop is lower.
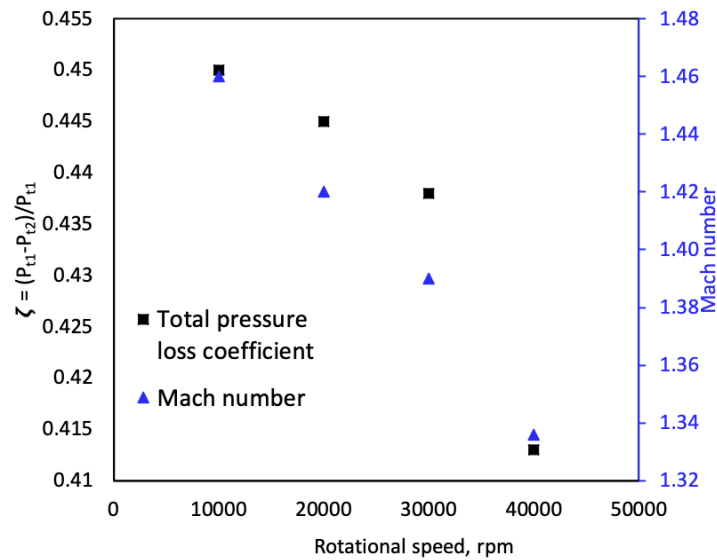
Figure 2.17 CFD data for nozzle performance. Total pressure loss from inlet of nozzle to rotor inlet versus rotational speed, at 2.5 bar nozzle inlet pressure

Another interesting aspect to study is the effect on nozzles when placed adjacent to each other. It is very crucial to select the number of nozzles as it affects the overall performance of the turbine. In this expander, two active adjacent nozzles are placed at 45° apart. The purpose is to understand the effect of two adjacent nozzles on the performance of the turbine. Figure 2.18 shows the contour plot of velocity magnitude for 3 bara inlet nozzle pressure at 10000 rpm.
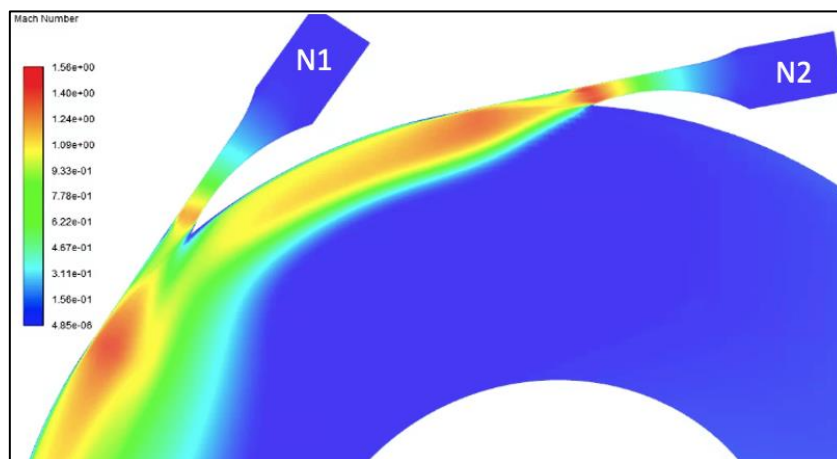
Figure 2.18 Contour plot of velocity at 10000 rpm and 3 bar inlet nozzle pressure
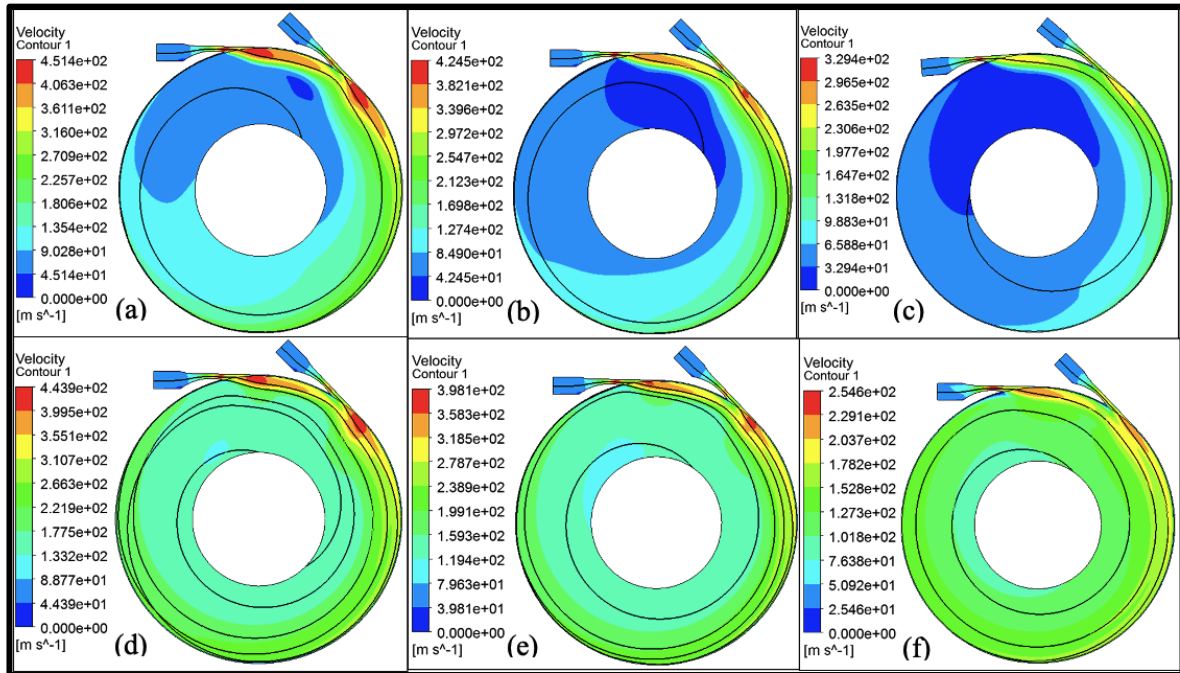
Figure 2.19 Turbine velocity contour and path lines obtained from CFD simulation for different inlet total pressures. (a) 3.4 bara, 10000 rpm (b) 2.5 bara, 10000 rpm (c) 1.5 bara, 10000 rpm (d) 3.4 bara, 40000 rpm (e) 2.5 bara, 40000 rpm (f) 1.5 bara, 40000 rpm

We observe from Figure 2.18 that the nozzle, N2, achieves more velocity than nozzle N1. Clearly the performance of the back nozzle, N2, gets affected due to the front nozzle, N1. We observe in Figure 2.19 that the flow is disturbed from its natural streamline path. This deflection of the flow from its natural path causes degradation of rotor performance. Tesla [1][2] claimed that to achieve maximum efficiency of the rotor, fluid should flow to its natural path. Hence, adjacent nozzles affect the performance of the other nozzles and rotor performance itself leading to significant drop in the overall expander performance.

Rotor: Tesla mentions in his patent the following : " in order to attain the highest economy, the changes in the velocity and direction of the movement of the fluid should be as gradual as possible and propelling fluid to move in natural paths or stream lines of least resistance, free from constraints and disturbance and to change its velocity and direction of movement by imperceptible degrees, thus avoiding the losses due to sudden variation while the fluid is imparting energy"[2]. This means that fluid should follow a spiral path from inlet of rotor to exit, changing the velocity gradually. Figure 2.19 shows streamlines from both the nozzles for

different inlet pressure conditions/mass flow at 10000 and 40000 rpm. We see that fluid takes longer path in case higher rotational speed of the disks. At 10000 rpm, rotor is subject to low velocity zones in the rotor. Hence the area available for the energy transfer is small. At higher rotational speed, 40000 rpm, we observe that the entire disk area is used for energy transfer between fluid and disk. It also shows no zones for low velocity field.

Figure 2.20 presents the variation of efficiency of the rotor+stator, rotor and stator separately with respect to rotational speed. It also shows the velocity ratio in each case with respect to rotational speed and the influence of stator and the rotor on the complete turbine performance.
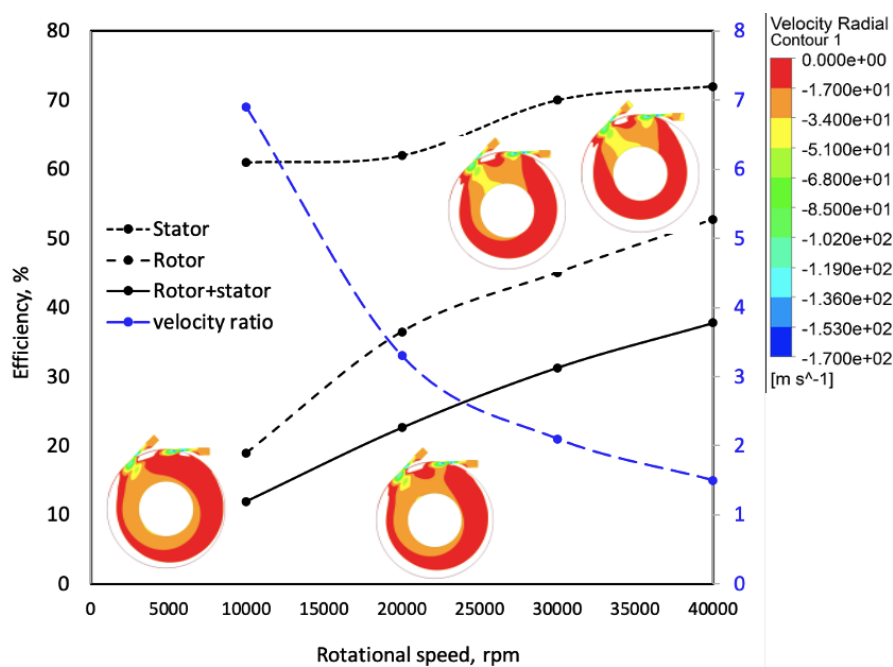
Figure 2.20 Variation of total to static efficiency for rotor and rotor+stator configuration, stator efficiency and velocity ratio with respect to rotational speed for the inlet nozzle pressure case of 2.5bar (negative towards the centre)

The efficiency of the stator, which includes the losses in the stator and the rotor cavity, varies between 60% to 70% and the overall rotor efficiency is found to be low. The increase in the rotor efficiency with rotational speed is due to the following reasons:

a. Velocity ratio decreases as rotational speed increases for given inlet nozzle pressure of 2.5 bar. The optimum velocity ratio is between 1 to 1.5. As the velocity ratio increases further, slip between disk and fluid increases leading to lower performance of the rotor.

b. Fluid travels in longer spiral path at higher rotational speed. Longer the path travelled, more energy transfer between fluid and disk takes place.

The relatively low rotor efficiency (for all the cases) is due to the high mass flow per disk, which can be seen in the radial velocity contour plots of Figure 2.20 (white area at the periphery of the red area represents the outward mass flow between disks, at gap centre).

Further in the rotor analysis, Figure 2.21 (left) presents the static pressure reduction in the rotor along the radial position. There is higher pressure reduction at the outer portion of the disks (~ < 20% radial position from the outer edge) and it is more gradual at the remaining portion of the rotor. For the efficient design of the rotor, gradual static pressure reduction across the rotor is favorable. Such pressure drop in the rotor represents the energy transfer to the disk. In order to ensure higher rotor efficiency at all the radial locations, gradual pressure drop in the rotor should be ensured while designing the Tesla expander, as also shown by Rice[5].

Figure 2.21 (right) shows the degree of reaction of the Tesla expander. Degree of reaction is calculated using equation (2.29) which is static pressure drop across the rotor with respect to overall pressure drop. The highest degree of reaction is seen at highest efficiency operating cases, which is at low inlet nozzle pressure and high rotational speeds, as also observed in analytical solution[5].
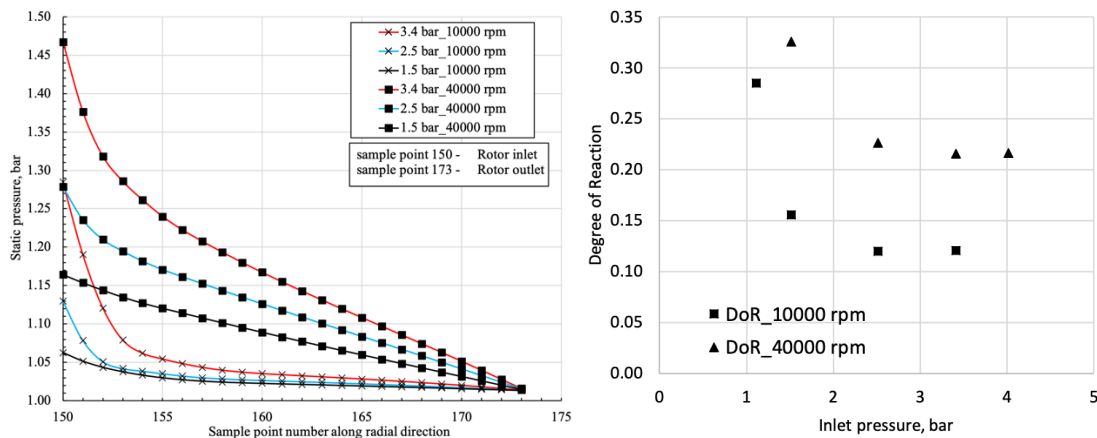
Figure 2.21 Variation of static pressure (abs) inside the rotor at different nozzle inlet pressures and rotational speeds along the rotor radial position (inlet to outlet of rotor)

2.2.2 Air 3kW Tesla Expander prototype

In this section, performance of the Tesla turbine simulated with stator and the rotor for 3kW expander is described. The simulation is run for 1, 2, 4 and 8 number of nozzles for different rotational speeds and expander inlet pressures. The nozzle used in this prototype is convergent only to avoid the supersonic flow and related total pressure losses as discussed in section 2.2.1. However, due to the sudden enlargement area at the exit of the nozzle due to rotor-stator clearance, the flow may become supersonic at higher nozzle inlet pressure. Details about the experimental set-up are described in section 3.1.

Figure 2.22 shows the geometry and the hexahedral mesh for the 3-kW expander with the boundary conditions. The methodology of CFD simulation (mesh sensitivity, solver, set-up, working fluid) is same as described for 100 W expander.
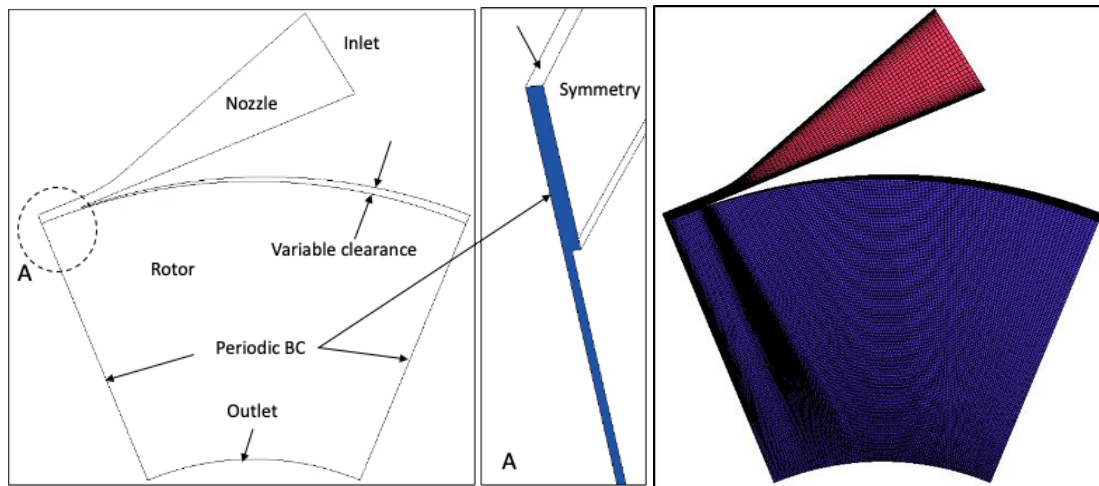
Figure 2.22 Geometry and mesh for air 3kW expander

At first, the numerical performance is compared with experimental data (uncertainty ±1.8%) as shown in Figure 2.23. As for the 100W prototype, CFD simulation does not incorporate the ventilation, mechanical, exhaust and leakage losses. Hence, the power and efficiency curves obtained from CFD show higher values. The figure also shows the CFD data subtracting experimental ventilation loss[45]. The trend of the CFD curve with ventilation loss approaches the experimental curve, showing a very similar trend. The remaining difference in the efficiency is mainly due to exhaust loss and leakage loss (bearing losses can be estimated of

one order of magnitude lower). Similarly, to 100 W expander case, leakage losses are high at higher nozzle inlet pressure or mass flow.
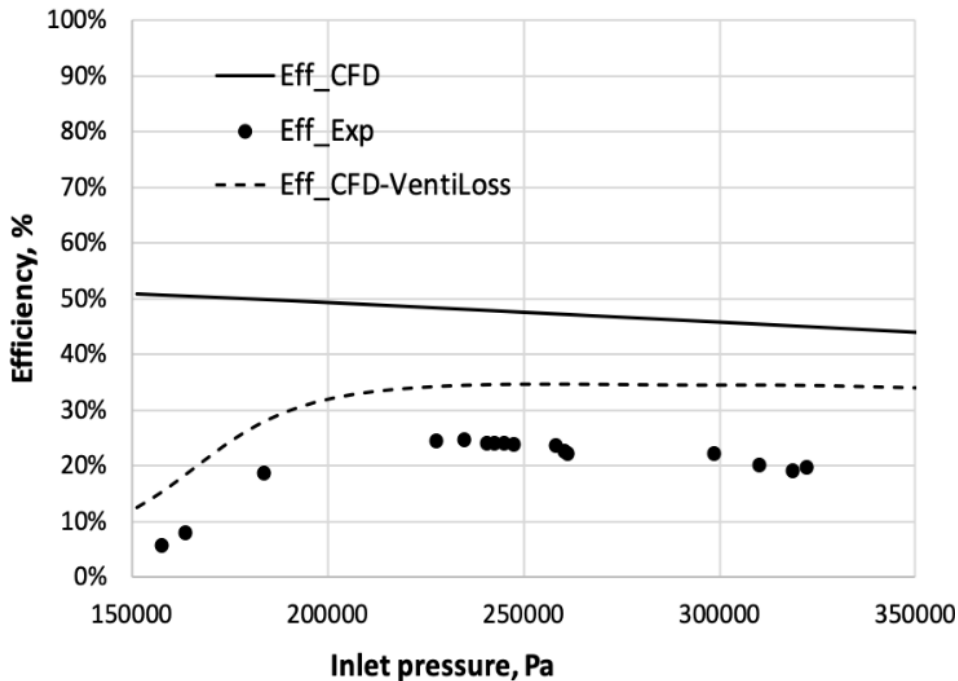
Figure 2.23 CFD and experimental performance comparison for 2 nozzle case

at 10000 rpm

Here, the performance of the expander with stator and rotor is described with the help of qualitative analysis using fluid dynamics analysis inside the rotor.

Figure 2.24 presents the total pressure, normalized with inlet total pressure, along the clearance between the rotor and stator for 2 nozzles (2N) and 8 nozzles (8N) case. The x-axis represents the position in the stator-rotor clearance shown in Figure 2.24 (left) from no. 1 to 7, where 1 is the nozzle exit and 7 being the next adjacent unfed nozzle. The two-nozzle case shows a total pressure loss higher than the 8 nozzles case for the same inlet pressure and rotational speed. This is due to the fact that 8 nozzles case carries 4 times mass flow than 2 nozzles case. Due to the higher mass flow, the rotor periphery static pressure is higher than the 2 nozzles case (the rotor being the same in both cases). Higher back pressure leads to lower velocity at the exit of the nozzle. This lower velocity leads to lower total pressure loss at the clearance between rotor and stator as the friction loss in the clearance is proportional to the square of the velocity: therefore, there is a clear advantage in operating all the 8 nozzles.

51
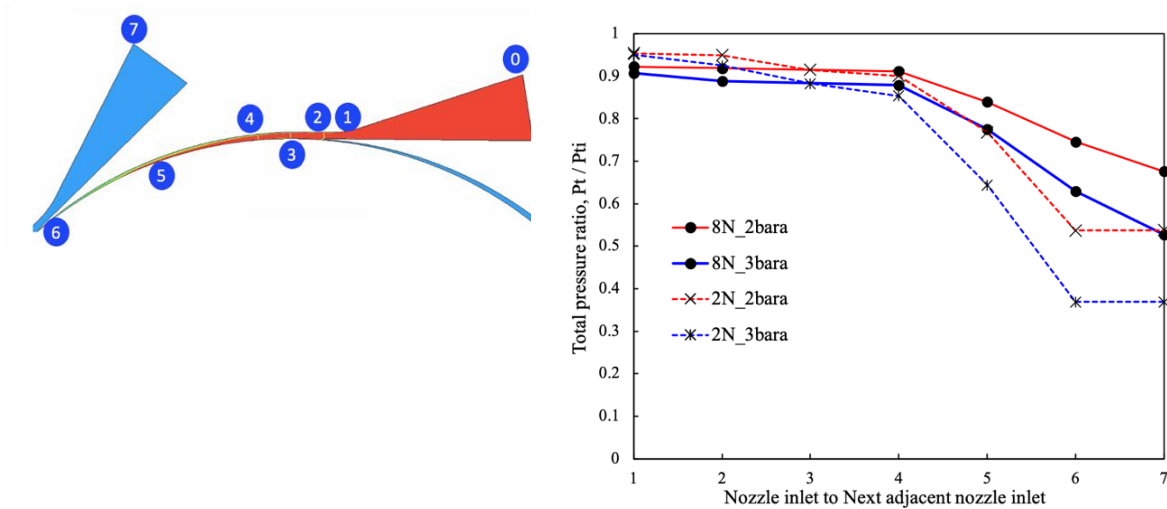
Figure 2.24 Variation of total pressure along the rotor - stator clearance (x-axis is the position where total pressure is measured as per diagram on the left)

Figure 2.25 shows the relationship between efficiency, total pressure coefficient (TPC), degree of reaction (DoR), tip velocity ratio (maximum nozzle-exit velocity and mass flow averaged velocity at the rotor inlet - just before the disk tip) with respect to number of nozzles at fixed inlet total pressure and rotational speed. Total pressure loss coefficient is the reduction in total pressure from nozzle inlet till rotor periphery (mass flow averaged total pressure at rotor). We see that total pressure loss coefficient increases as the number of nozzles decreases. As seen previously, this is due to the higher nozzle exit velocity, increasing friction loss between rotor and stator. Degree of reaction is seen increasing with number of nozzles with optimum value between 0.3 – 0.4 (for velocity ratio higher than 1), which was also observed in case of 100 W expander. We see that the difference between maximum velocity at the exit of the nozzle and mass averaged velocity at the rotor periphery is higher at low number of nozzles. This signifies that the loss in tangential velocity from the exit of the nozzle till rotor periphery due to stator-rotor interaction losses and larger surface area at the casing for viscous frictional loss.
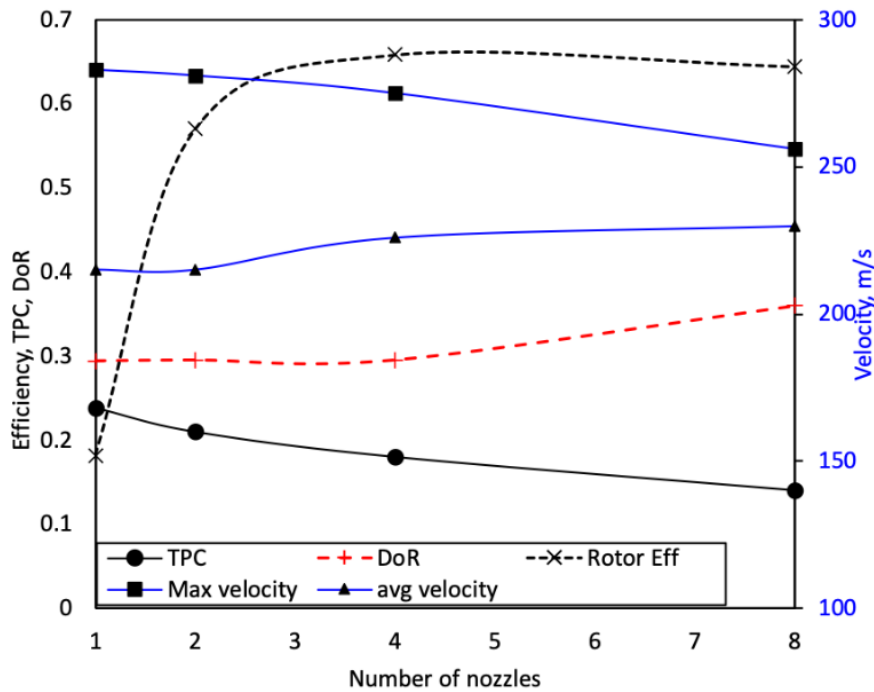
Figure 2.25 Variation of rotor efficiency, total pressure loss coefficient (TPC), degree of reaction (DoR), maximum velocity and average velocity with respect to the number of nozzles for the operating point at 1 bar and 30000 rpm

On the other hand, rotor efficiency increases as the number of nozzles increases. However, there is a peak at 4 nozzles configuration. This trend is due to the effect of higher mass flow at higher number of nozzles. It is an established fact [5] that as mass flow increases rotor efficiency decreases. The mass flow contributes to the impact on rotor efficiency along with parameters discussed above. Hence it is important to design the rotor and number of nozzles simultaneously for higher overall performance of the expander. In any case, rotor efficiency clearly shows a kind of plato beyond 4 nozzles, with limited reduction in efficiency passing from 4 to 8 nozzle configurations: larger number of nozzles and mass flow may contribute to reduce the impact of ventilation and leakage losses, not computed here.
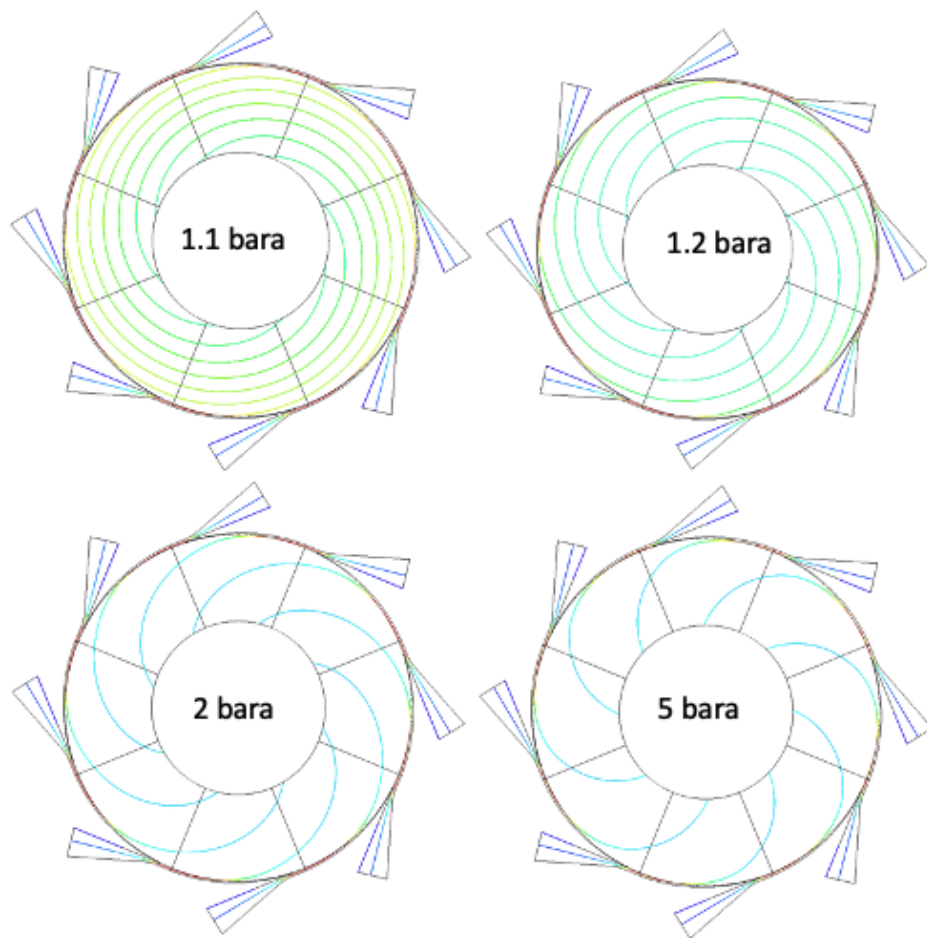
Figure 2.26 Streamline plot for 8 nozzle configurations at 10000 rpm for different inlet nozzle pressures

The effect of mass flow on the rotor efficiency can also be seen in the streamline plot of 8 nozzles configuration for different nozzle inlet pressure or mass flow, as shown in Figure 2.26. At lower mass flow (lower inlet pressure), the fluid travels longer path and as the mass flow increases, the path becomes shorter. Higher fluid path leads to more efficient energy transfer between fluid and disk. This effect is also plotted for 2-nozzle configuration at different inlet pressure and for two different rotational speeds, 10000 and 30000 rpm in Figure 2.27. We, similarly, observe the streamline trend with respect to mass flow for 2-nozzle case. The effect of rotational speeds also can be clearly seen on the path travelled by fluid. There is a significant increase in fluid path travel length at 30000 rpm compared to 10000 rpm. The increase in efficiency can be seen in Figure 2.29.
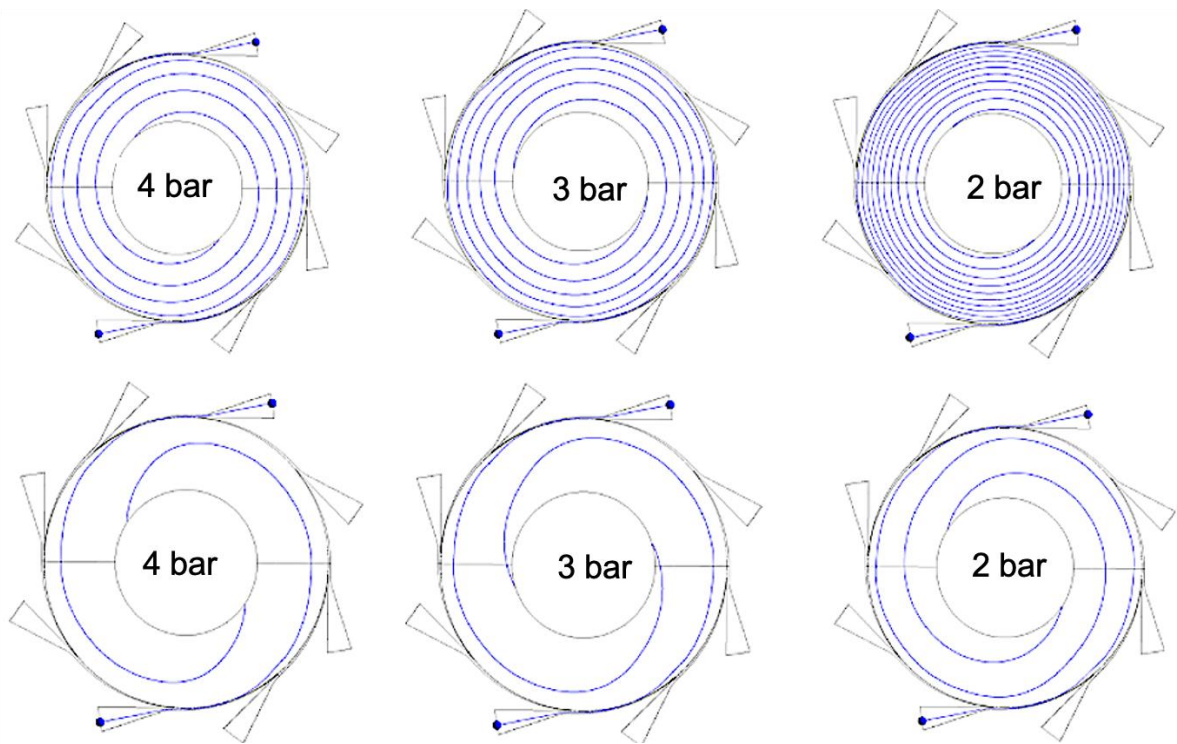
Figure 2.27 Streamline plot for 2 nozzle configuration at (top) 30000 rpm and (bottom)10000 rpm for different inlet nozzle pressures

It is established that, as the number of nozzles increases, flow axisymmetry is achieved towards inlet of the rotor, as seen in Figure 2.28, where 8 nozzles configuration attains the most axisymmetric inflow condition resulting in higher performance. The significantly higher power obtained for 8 nozzle case compared to the 4 nozzle case should drive the designer preferably towards the 8 nozzle case: in fact, the apparent similar peak efficiency will be later displaced in favour of the 8 nozzle case by including ventilation and leakage losses, not included in this analysis.

The overall expander performance (rotor +stator) can be seen in Figure 2.29. The variation of efficiency and power is shown with respect to rotational speeds for different number of nozzles. We need to take note that these curves are plotted for same nozzle inlet pressure of 1 bar. From the efficiency and power plot, we observe the trend of increase of efficiency and power with respect to number of nozzles and rotational speed as explained in previous sections. There is peak seen at particular rotational speed and the it drops for further increase in speed. This is due to the decrease in velocity ratio at the rotor inlet. The velocity ratio lower than 1

significantly reduces the expander performance due to negative relative velocity (fluid velocity – disk tip velocity) between disk tip and accelerated fluid.
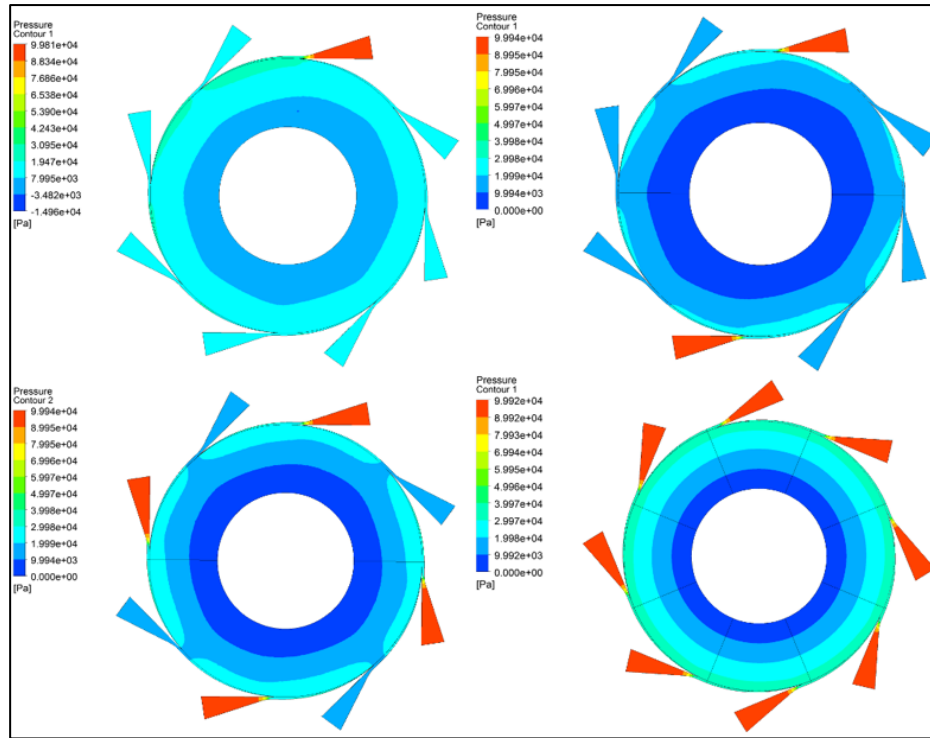
Figure 2.28 Static pressure contour for 1, 2, 4 and 8 nozzles at operating point of 1 bar and 30000 rpm
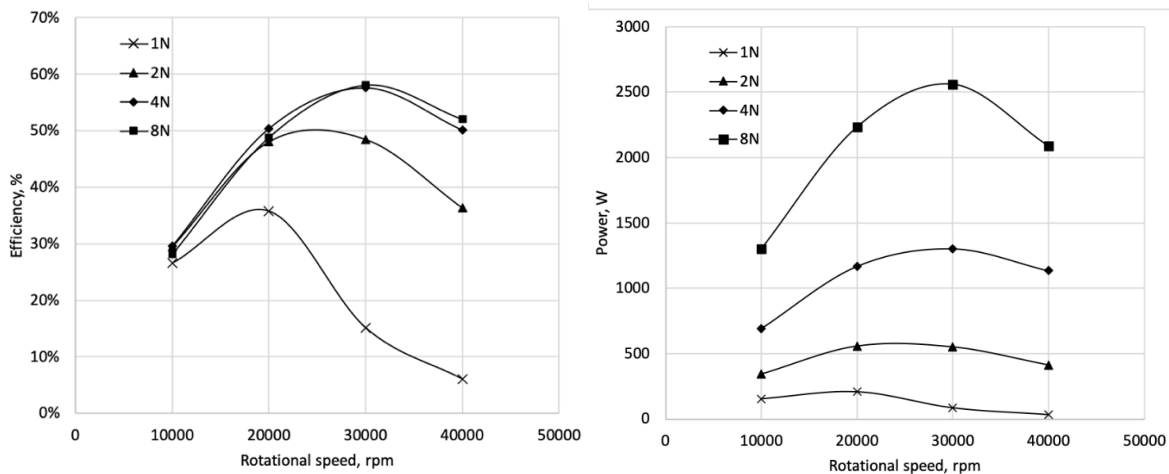
Figure 2.29 Variation of efficiency and power with respect to rotational speed for 1, 2, 4 and 8 number of nozzles (1N, 2N, 4N and 8N) at the fixed nozzle inlet pressure of 2 bar

The expander power increases with respect to number of nozzles as mass flow increases in similar proportion. However, the power increases less than proportionally to the number of nozzles, as the higher static pressure at the rotor periphery decreases the nozzle exit speed, leading to lower power gains, as the number of nozzles is increased. More CFD contour plots are available in the Appendix B section for flow visualisation at different rotational speeds and number of nozzles.

2.2.3 Water 1 kW Tesla Expander Prototype

The water expander studied in this section is designed based on the high performing novel "ultra-efficient" bladeless concept developed based on the deep understanding of the stator-rotor loss phenomenon investigated on bladeless turbomachinery on the previous air prototypes and later presented in depth in chapter 4. The core innovation of this prototype focused in reducing the loss mechanism contributing most to the performance. In fact, one of the reasons why bladeless turbomachinery hasn't been successful commercially is the experimental low efficiency. This is due to the requirement of highly tangential flow at the inlet of the rotor. The present innovation reduces the losses between stator-rotor significantly by ensuring lesser wetted surface available for the tangential flow between stator-rotor region. This innovation improves the performance of the bladeless turbine/compressor to the level of conventional bladed machinery, making it now competing with conventional machinery not only at lower scale (where bladed machinery suffers high losses, differently from bladeless machinery) but also at large scale: patent has been recently submitted (Appendix C).

Unlike many inventors who have tried to improve the performance of the Tesla turbomachines by introducing complex features on the disks itself, increasing the complexity of the original bladeless Tesla design, the present invention only adds external simple features in the original Tesla's bladeless turbomachinery. These features are simple to manufacture and straightforward to implement without introducing additional complexity into the original bladeless design.

The prototype, which numerical results are described hereby, has been designed to perform demonstration of liquid Tesla expander for heat pump application condition.

The design point case used to demonstrate the present "ultra-efficient" Tesla turbine is for expansion of butane as working fluid, as shown in Figure 2.30. As seen in the P-h diagram, the expansion is in liquid phase (incompressible fluid), therefore we consider water (safe – incompressible fluid) for performance demonstration applying similitude considerations to later transfer the results to the liquid butane expansion case.
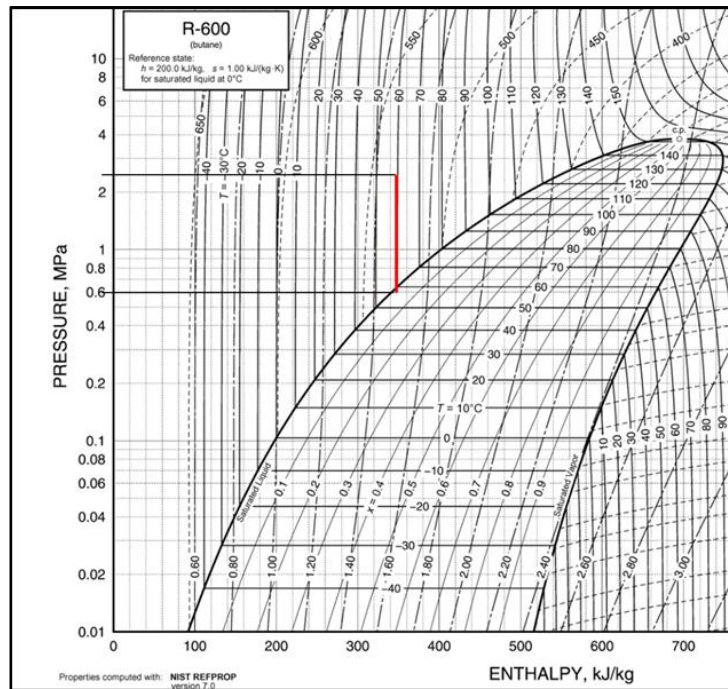
Figure 2.30 P-h diagram for butane (R-600) with design conditions for expander

Therefore, considering the derived butane thermodynamic conditions, targeting a water prototype design as close as possible to such butane thermodynamic condition, the following design point is formulated.

Table 2.3 Thermodynamic design specification

Thermodynamic data	Demonstration design data
Working fluid	water
dp across turbine, bar	14
Rotational speed, rpm	10000
Mass flow, kg/s	2
Power, W	1400 (expected)
Efficiency, %	70+ (expected without leakage, ventilation and bearing loss)

The key principle of this innovation is to guide the fluid flow with uniform tangential velocity to the rotor. This is obtained with the help of two rotating shaped disks, as shown in Figure 2.31, mounted on both sides of the rotor. Regarding radial stator flow is accelerated through a radial stator and directed towards the rotor gaps, where flow passes and exchanges momentum, from the disk tip entry to the disk inner discharge. Differently from conventional Tesla machinery, where the radial stator passages, located at the periphery of the rotating disks, have an axial dimension close to rotor disk ensemble, here the stator has a reduced axial dimension, for instance half, and the statoric jets are not directed immediately towards the rotating disks, but they first enter a rotating "swirl chamber". Such chamber is created by two special rotating shaped disk/s, symmetrically mounted on shaft, shaped in such a way that they form a rotating radial passage to drive the fluid from the stator to the rotating disks. In this way, a significant radial distance exists, for instance 10% of the disk tip radius, between the stator and the rotating disk ensemble: as a consequence, friction between rotating disk ensemble and stator or casing is minimised, reducing friction losses between rotor and stator.
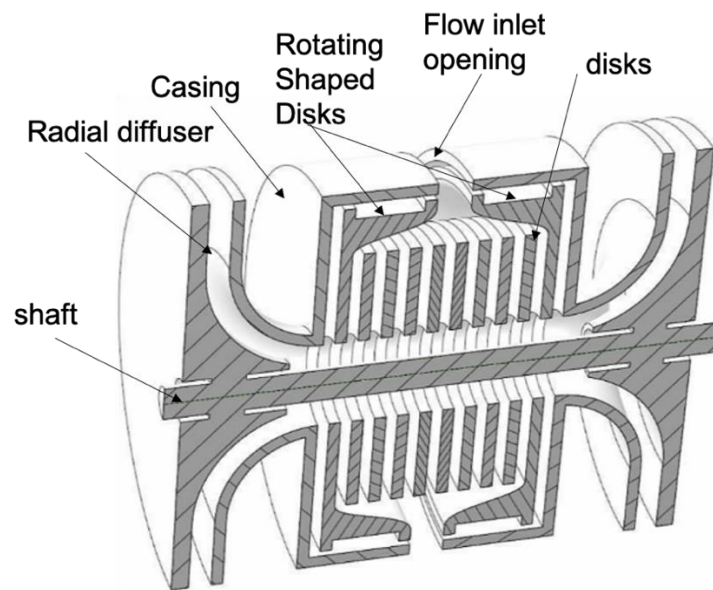
Figure 2.31 Schematic of "ultra-efficient" Tesla turbomachinery

The rotor design is done based on the 0-D algorithm outlined in the section 2.1.1. The 0-D algorithm defines the specifications the turbine for this study, as shown in Table 2.4.

Table 2.4 Turbine design specifications

Turbine specifications	
Stator	3D printed – 5º inlet flow angle
Number of nozzles	24
Rotor disk outer diameter, mm	80
Rotor disk inner diameter, mm	32
Disk discharge section holes	3
Disk thickness, mm	0.1
Gap between disks, mm	0.1
Number of disks	150
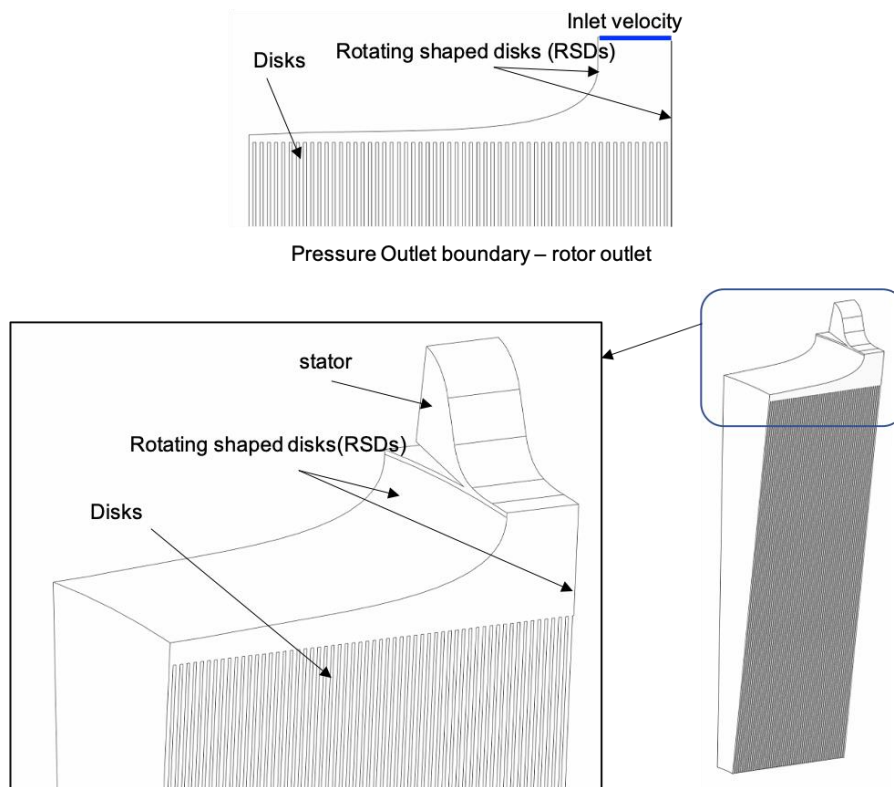
Figure 2.32 2-D axisymmetric (top) and 3-D CFD geometries (bottom)

2D and 3D computational fluid analyses are performed in order to check the efficacy of the novel design. Mesh sensitivity analysis is performed to ensure that there is no significant change in output parameters. The k-w SST turbulence model is used and Y+ <1 is used for rotor and walls present in the system. The working fluid as water with constant density properties is used.

The CFD geometry simulated in 2D and 3D is shown in Figure 2.32. The 2D geometry consists of rotating shaped disks, swirl chamber and disks (without exhaust system). The inlet condition is uniform tangential and radial velocity components and outlet with ambient pressure. The 3D geometry consists of rotating shaped disks and disks exactly the same as 2D except here a stator is used. The 3D simulation is closer to real turbine working condition. A conventional convergent nozzle geometry is used.

Results and discussion

The results of calculations are shown in Table 2.5. The 2D simulation is not capturing the stator losses but is retaining the stator-rotor interaction losses: for this reason, total to total efficiency, higher in 2D then in 3D, is obtained. On the other hand, the 3D model with stator (i.e. stator losses are included) predicts ~70% total to static efficiency. The difference in efficiency is due to losses present between stator exit and rotor inlet. The geometrical optimization of the nozzle would minimise the difference between 2D and 3D efficiencies.

The results are very promising and efficiency values predicted by CFD are far beyond than the known in literature. The CFD values in the literature has been found typically in the 50-60%: with the present innovation efficiencies exceeding 80% overall (numerical) has been recorded.

Table 2.5 2-D and 3-D CFD performance data for water expander with 24 nozzles

	Rotational speed, rpm	v_{ti}, m/s	Mass flow. kg/s	Total to static Efficiency, %
2-D	10000	53	2.19	77
3-D	10000	53	1.89	70

The CFD simulation of radial diffuser shows remarkable improvement in static pressure gain at the exhaust duct. One such analysis is performed as shown in Figure 2.33. The expander with Tesla rotor disk pack and radial diffuser exhaust system converts ~ 70-80% of kinetic energy at the exhaust of the rotor into static pressure, thus improving the overall performance of the expander. This improves the efficiency of the expander up to ~ 6-7 points. 2-D CFD is used to perform radial diffuser optimization. Figure 2.33 shows the comparison of preliminary diffuser design with respect to optimised design. The static pressure plot shows clearly rise in static pressure in the optimised design. Preliminary design has wider radial diffuser width

which is responsible for the recirculation for the flow. The decrease in width of the diffuser prohibits the recirculation and corresponding pressure losses. One of the important factors in the Tesla rotor is high swirl exit velocity. The objective of radial diffuser is to convert swirl velocity into static pressure. In order to achieve this, length of the radial diffuser from inlet to exit plays an important role. As seen in Figure 2.33, increase in diffuser length further decreases the swirl velocity that converts into static pressure. The detailed study of the exit radial diffuser is a promising research area in the context of Tesla expanders.
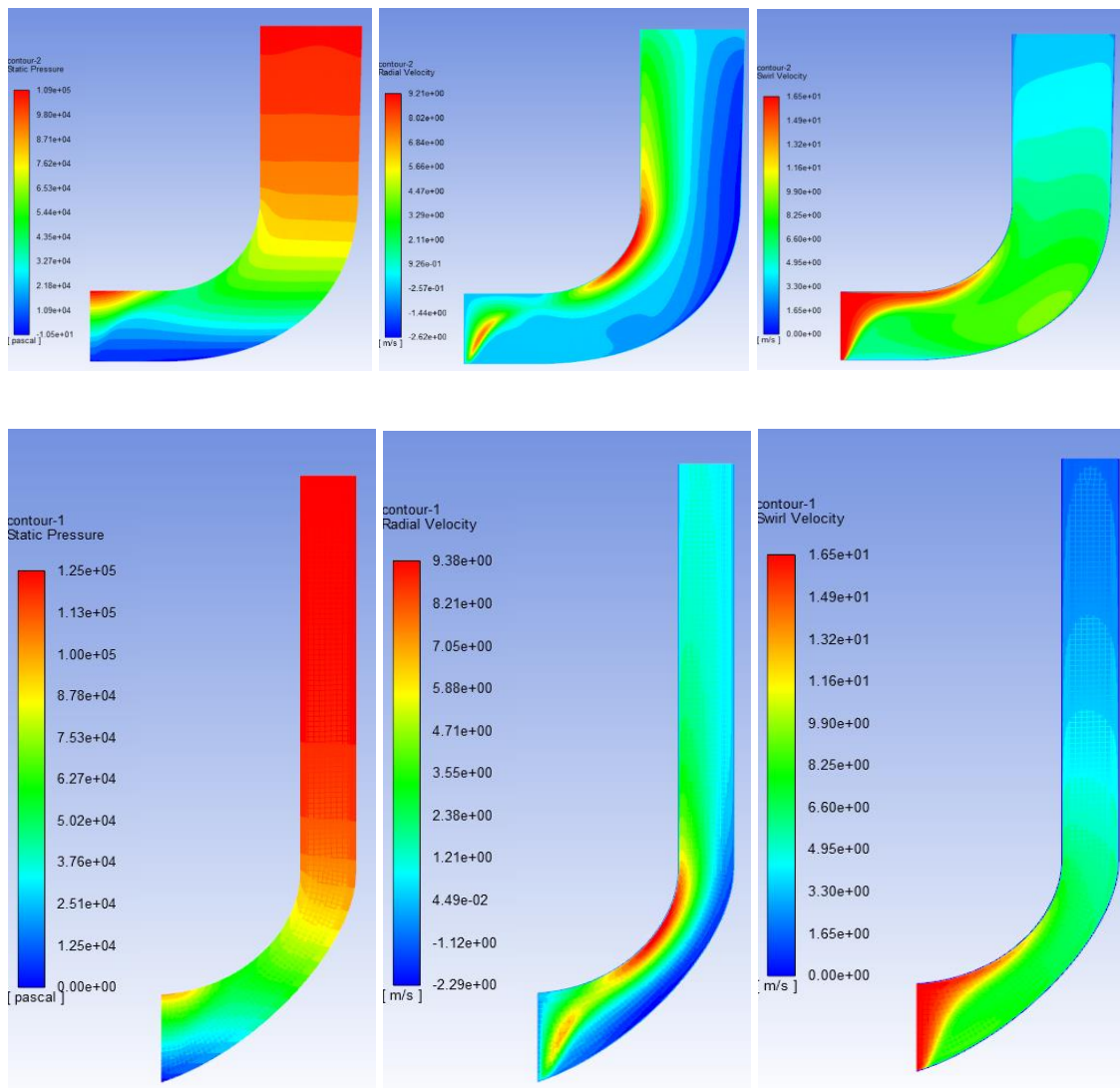
Figure 2.33 CFD of radial diffuser for water expander: (top) preliminary design and (bottom) optimized design. From left to right – static pressure, radial velocity and swirl velocity.

2.3   Summary of Numerical Analysis

The design of the tesla expander rotor begins with the 0-D algorithm in which rotor parameters are obtained with preliminary performance variables. 2-D analysis is then used to fine-tune the rotor parameters to achieve design conditions for the best efficiency point.

3D numerical analysis if performed on all the prototypes investigated in this thesis – air 100W, air 3kW and water 1 kW. Following insight is obtained from the analysis:

1. Stator of the Tesla rotor is defined, and performance is evaluated using 3D CFD analysis. Performance curves for each prototype are obtained to understand the experimental limit of the operation and validation of CFD model with experimental data.

2. For each prototype, loss characterisation is performed, mainly, stator and stator-rotor interaction losses. The loss data is used for improvement of the subsequent protypes.

3. 3D CFD analysis helped mainly to identify stator and stator-rotor losses and flow field inside the Tesla rotor for different operating conditions and rotational speeds.

    a. Air 100W expander: the detail loss characterisation using 3D CFD revealed that main contributor to the low performance of the expander is due to stator and stator-rotor interaction losses. The convergent-divergent nozzle led to supersonic flow which in turn led to shock waves formation. The shock waves created total pressure loss from exit of nozzle to entry of rotor.

    b. Air 3kW expander: this expander is designed using convergent nozzle to avoid supersonic flow and related losses. The stator is designed in such a way that the flow is tangential to the rotor and reduces entry losses. 3D CFD analysis gave higher performance than air 100W expander due to stator modification. Also, use of 8 nozzles enhanced the axisymmetric condition of the rotor inlet which is favourable condition for the performance of the rotor.

    c. Water 1kW expander: this expander is improved version of previous two prototypes and from the detailed loss characterisation of the 3kW some innovations are introduced to achieve overall total to static efficiency closer to the rotor efficiency.

Chapter 3   Experimental Investigation

3.1   Air 100W Tesla Expander Prototype

This section presents in detail the experimental campaign test on air 100W Tesla expander prototype. The objectives of the 100W expander prototype are: (1) design and testing of modular Tesla turbine with flexible test rig, (2) to study thoroughly the impact of main parameters on performance of Tesla turbine: (i) disk thickness (ii) gap between disks (iii) outlet opening of disk (iv) exhaust area of turbine (3) to characterize losses.

3.1.1   Turbine Components

The Tesla turbine prototype used in the experimental campaign consists of following main components: rotor, stator, and casing.

The rotor consists of smooth flat steel disks separated by spacers as shown in Figure 3.1 (a). The entire stack of disks and spacers are held together with the help of bushes. The shaft has a central part of circular cross section with two opposite and parallel flat sides, to allow the fitting of disks and spacers. The ends of the shaft is provided with threads with diameter and section equal to the central one, and even more externally, two sections in circular cross section. On this threaded connection, flywheel for magnetic brake and disks with magnets to detect rpm are attached. The rotor disks have a diameter of 64.5 mm and three different central hole diameters of 20mm, 25mm, and 30mm with a central fitting of 7.5mm for shaft. There are three different thicknesses of the disks used to evaluate impact on performance as shown in Table 3.1.

Around central hole, there are three other elongated holes identical to each other, whose purpose is to allow fluid to escape from the centre of the turbine only after going through the entire rotor and having transmitted energy to the disks. At the beginning and at the end of the pack of disk, there are washers/spacers of small size, interposed between final disks and bushes, which are shown in Figure 3.1 (a), whose outer diameter is equal to the inner diameter of the

three elongated holes of the disks so leaving no gap between the disk and spacer avoiding losses. The inner hole of the spacers (Figure 3.1 (a)) has geometry equal to the central shaft section, like that of the disks, to make all the rotor elements integral with each other, avoiding unnecessary friction and vibration. These elements are manufactured with stainless steel AISI 301.
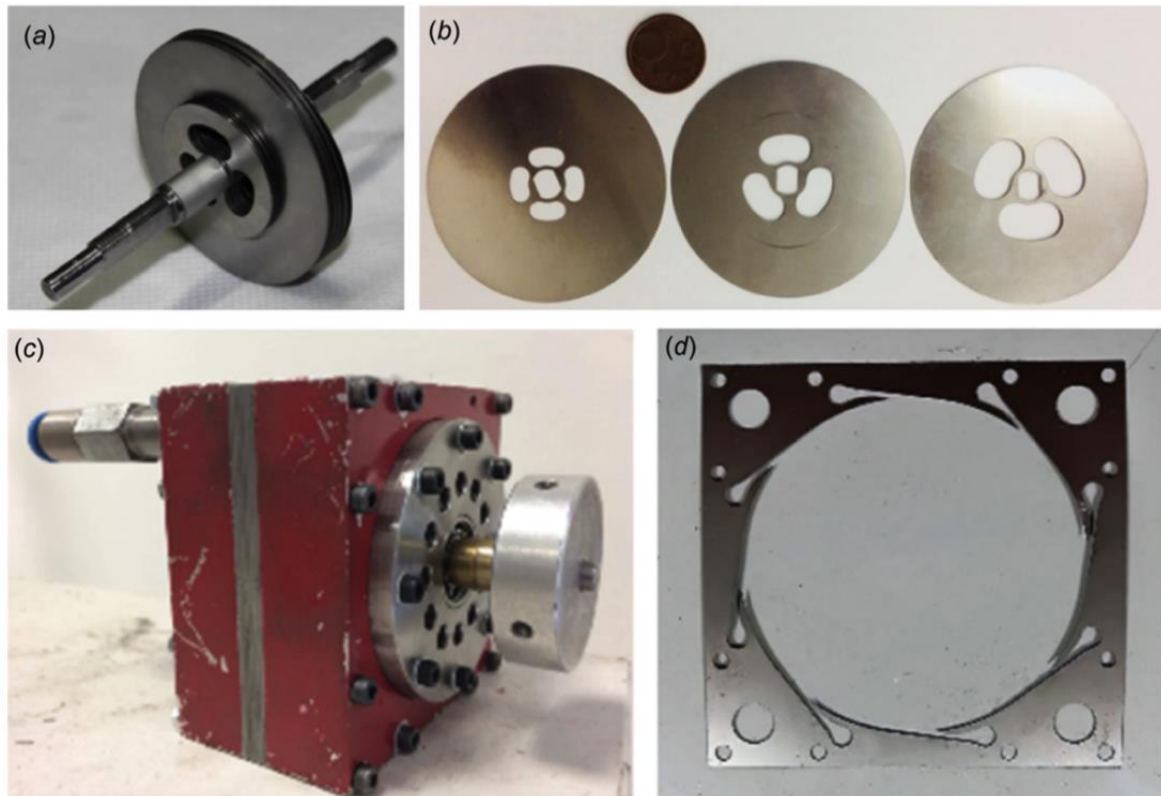
Figure 3.1 Turbine components—(a) rotor with disks, spacers, and shaft, (b) disks with different central opening, (c) assembled Tesla turbine prototype with flywheel for magnetic braking, and (d) stator element

The stator is composed of three different elements with some features in common. As shown in Figure 3.1 (d), all the plates have a very large central hole in which rotor is placed with an average clearance of 0.2 mm. Four holes at the corner of plates out of which two holes are given provision for entry of fluid and other two holes for symmetry of casing. Entire casing with stator plates with rotor inside are held together with 12 small studs. Complete stator thickness is equal to that of the pack of disks and spacers. The distance between the last disk

and the casing wall is such that they do not touch each other avoiding a strong friction and overheating, which would worsen the overall performance of the turbine.

Table 3.1 Different configurations of parameters for tests

Disk thickness (mm)	Gap (mm)	Disk inner diameter (mm)	Exhaust area (mm^2)	Number of disks
Effect of gap between disks				
0.1	**0.1**	25	A2	20
0.1	**0.2**	25	A2	14
0.1	**0.3**	25	A2	11
Effect of disk thickness				
0.3	0.2	25	A2	8
0.2	0.2	25	A2	10
0.1	0.2	25	A2	14
Effect of disk inner diameter				
0.3	0.2	**20**	A2	10
0.3	0.2	**25**	A2	10
0.3	0.2	**30**	A2	10
Effect of exhaust area				
0.2	0.2	25	**A1**	10
0.2	0.2	25	**A2**	10

The bold values indicate controlled parameters.

There are eight convergent-divergent nozzles and a multiple of two nozzles (2, 4, and 8) can be activated at a time. In this experimental campaign, two adjacent nozzles are activated. From turbine inlet to upstream of nozzle, compressed air passes through tortious path causing losses, which have been eliminated in the next experimental campaign.

The casing is the outer part of the turbine and is composed of two identical pieces. Two pieces of the casing tightly hold the pack of stator along with rotor. There are two exhaust holes on the casing from which exhaust fluid symmetrically flows out of turbine. One half of the casing is equipped with hole for inlet of fluid into stator. The bearings used are low-friction SKF 608 22 mm external diameter and 8 mm internal ball bearings, readily available in the market.

3.1.2 Description of Experimental Set-up

The prototype of Tesla turbine is tested using a specially designed test bench (Figure 3.2) consisting of the following elements: a pressure line, which leads the compressed air from the entrance to the turbine through all sensors and gauges used to measure fluid properties; the

braking system used to generate a load on the turbine and at the same time to measure the performance of the turbine in terms of torque; the data acquisition system that is connected to all digital or analog electrical sensors to collect the data; there is also an analog display to allow a quick visual check of the conditions inside the duct and the turbine. All the components are fixed on a same disk to facilitate transportation and a metal shield covers the external rotating parts of the turbine to prevent damage in case of accidental breakage of some component at high rotational speed.

The pressure measurement is carried out in two points, one upstream of the flowmeter and the other downstream. The first measurement is performed by means of a differential pressure transducer, of the same series as the one used in the flowmeter, able to assess pressures between 0 and 7 bar. The exhaust pressure is not measured by a sensor as the turbine discharge outdoors and is therefore considered ambient pressure. About the torque measurement, it was carried through the magnetic eddy current brake coupled to a load cell. The configuration involves the use of two strain gauges, located, respectively, one on the upper face of the strain gauge finger and the other on the lower face, and the presence of a suitable amplifier adapted to make electrical output signal, which is normally few millivolt, in a more easily readable signal. The signal is then processed to calculate the force applied to the transducer.

Measurement System

Flow measurement: there are different systems for measuring the flow but for design and economic reasons, differential pressure gauge with a piezo resistive transducer is used. The differential pressure flowmeters are popular methods to measure fluid flow in industry. It has a widespread International standardization and reliability shown in the most varied fields of application. A calibrated orifice is located between two sections, which narrow down the flow, introducing a pressure drop Δp. Considering the principle of Bernoulli and of mass conservation equation, flow is calculated by

$$Q = K \cdot A \cdot \sqrt{2 \cdot \frac{\Delta p}{\rho}} \qquad (3.1)$$

<u>Temperature Measurement</u>: The temperature measurements are carried out with the use of K-type thermocouples, having operating temperature between -55 ^{o}C and 125 ^{o}C. The first thermocouple (measuring T_{line}) is placed after the regulating valve of the air flow. The second (which measures T_{in}) is placed before entering the turbine. Three other thermocouples (T_{e1}; T_{e2}; T_{e3}) are arranged in the exhaust manifold for detecting the temperature of the ejected fluid. All sensors are thermally insulated.

<u>Speed measurement</u>: For measurement of shaft rotation, a tachometer located next to the turbine housing was used. A Hall effect magnetic sensor is used, sensing the magnetic field variations generated by the rotation of the magnets in the bushing located on one shaft end. The Hall sensor has operation similar to optical sensors, with the difference that instead of detecting a light beam, it senses the magnetic field variations. Each revolution of the shaft is detected by the sensor, which allows to count the number of laps completed.

<u>Pressure Measurement</u>: The measurement of pressure is carried out at different locations in the test bench such as, static pressure in the line, difference in static pressure before and after diaphragm, static pressure at the turbine inlet, upstream of both nozzles and gap between nozzle exit and rotor. The turbine discharges outdoors; therefore, the ambient pressure is considered as the turbine exhaust pressure.

<u>Torque Measurement</u>: The torque measurement is performed by means of the magnetic eddy current brake mounted on the bench. This measurement was made by a load cell resting on a small protruding metal platform and screwed onto the brake stator that faces on the flywheel of the turbine. Knowing the arm of the flywheel, it is easy to calculate the resisting torque. The load cell is, in fact, an electronic component used to measure a force applied by the measurement of an electrical signal that varies due to the deformation produced by an arm. It detects the mechanical deformation of an object in an indirect manner, by reading in Volts and transforming it into the correct unit of measurement. The load cell is very sensitive to the effects of nonlinearity, variations due to thermal effects, etc. For this reason, it was necessary to verify the linearity of the sensor to find a specific calibration. Torque is calculated by multiplying load cell value in grams and arm length of flywheel.

<u>Data Acquisition System</u>: A key component is the data acquisition system, which interprets, processes, and records all the signals coming from the various sensors. Such system is fully automated and once started carries out in full autonomy all the functions necessary for the measurement and recording. A key component of the acquisition system is ARDUINO[46], which is an electronic card with a small microcontroller inside useful for quickly creating prototypes. The hardware (as well as the development software) is completely open-source and design drawings are distributed freely.

Evaluation of Energy Parameters

To evaluate the performance of the turbine in terms of efficiency and power, the choice had to be made on the most appropriate parameters to be used. The thermocouples positioned at the exhaust of the turbine measure a static temperature (i.e., not considering the fluid speed contribution), while for the pressure we considered the ambient pressure. As the turbine is not provided with an exhaust duct, it is not possible to calculate or derive the fluid output velocity and therefore not able to obtain the values of total temperature and total pressure at the exhaust. Instead, at the inlet section it is straightforward to measure total values of T and p. For this reason, knowing the total properties at the entrance and those static at discharge, we considered the parameters useful to the calculation of the performance as total to static.

The total pressure and the total temperature at the inlet of the turbine are calculated by

$$p_{in.tot} = p_{in} + p_{amb} + \frac{\rho_{in}\, v^2}{2} \qquad (3.2)$$

$$T_{in.tot} = T_{in} + \frac{v^2}{2c_p} \qquad (3.3)$$

Torque can be directly calculated using the force measured by the load cell, Fr, and arm, l

$$\tau = Fr.l \qquad (3.4)$$
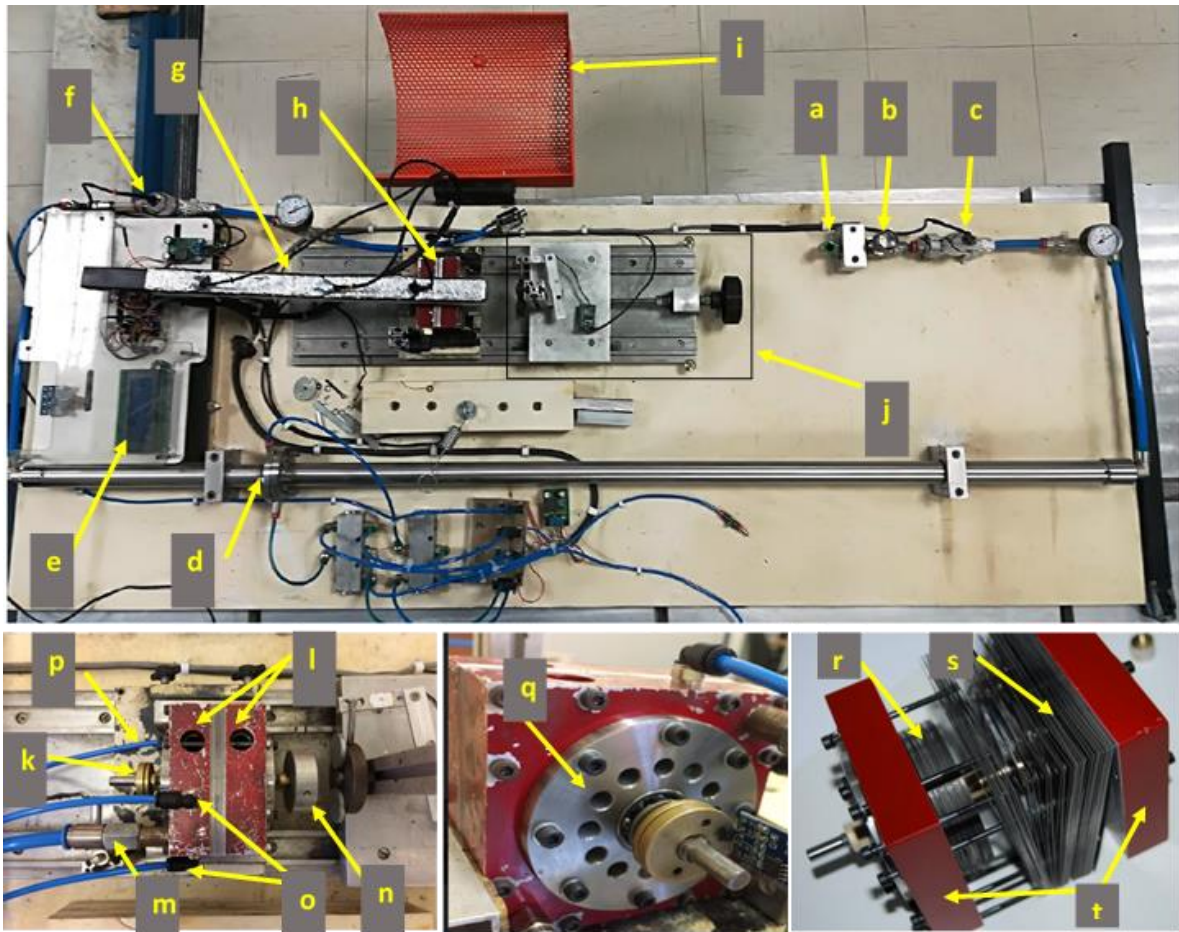
Figure 3.2 Test rig: (a) compressed air input, (b) flow controlling valve, (c) temperature probe, T_{line}, (d) diaphragm flowmeter, (e) real-time reading display, (f) temperature before turbine, T_{in}, (g) exhaust manifold to measure exit temperature, T_{e1}, T_{e2}, and T_{e3}, (h) turbine prototype, (i) protecting cover, (j) slider for magnetic brake, (k) disk for rotational speed measurement, (l) turbine two main outlets, A1, (m) turbine inlet, (n) flywheel, (o) pressure tap upstream of nozzles, (p) pressure tap between stator and rotor, (q) additional outlet for fluid, A2, (r) rotor, (s) stator elements, and (t) casing

It is therefore possible to calculate the mechanical power using torque of the rotor and angular velocity as:

$$P_{exp} = \tau . \omega \qquad (3.5)$$

Mechanical efficiency total-to-static $\eta_{exp.tot.st}$ can be computed as the ratio of actual enthalpy drop to the isentropic enthalpy drop across turbine. Isentropic expansion of air at low pressures does not produce high temperature drop. Uncertainty in measuring temperature is 0.5 C, which gives more uncertainty in the measurement of efficiency. Measuring torque of the turbine gives less uncertainty compared to enthalpy estimation from temperature. Therefore, efficiency is calculated through eq.(3.7), which is preferred to eq.(3.6) for the lower uncertainty (see next paragraph).

$$\eta_{exp.tot.st} = \frac{h_{in} - h_e}{h_{in} - h'_e} \tag{3.6}$$

$$\eta_{exp.tot.st} = \frac{P_{exp}}{c_p T_{in.tot} \left(1 - \frac{1}{\varepsilon^{\frac{k-1}{k}}}\right) \dot{m}} \tag{3.7}$$

Specific heat at constant pressure, c_p and heat capacity ratio, k is considered constant with temperature. For air, c_p = 1.005 kJ/kg K and k = 1.4 is used.

The parameter expansion ratio e is given by

$$\varepsilon = \frac{p_{in.tot}}{p_{e.st}} \tag{3.8}$$

Uncertainty Analysis

Efficiency of the turbine is calculated using Eq. (3.7), which is evaluated from the measured parameters like the temperature, the pressure, rotational speed, and torque. Mass flow rate is calculated by measuring pressure difference. Each of these quantities is affected by uncertainties due to instrument error, calibration error, and random error that propagate to the result through the function that binds the result to these parameters. Instrument errors for digitally recorded values are assumed negligible. Calibration errors are reported in Table 3.2. Random error is calculated by repeating experiment under same atmospheric conditions and with same user for different rotational speeds and inlet pressure. Combined error in an instrument is calculated by using root sum square method[47] .

The uncertainty in function g with n direct measures, g = f (x1, x2, x3,..., xn), can be calculated as follows [47][48]:

$$U_g = \sqrt{\sum_{i=1}^{n} \left(\frac{dg_i}{dx_i}\Delta x_i\right)^2} \tag{3.9}$$

where U_g is the uncertainty observed in g, while dx_i, is uncertainty in i^{th} measure. Uncertainty of efficiency is calculated over broad range of data. Maximum uncertainty in efficiency is found to be ~0.7% for low mass flow values. To account for the 95.5% confidence interval, standard deviation for all repeated measurements is taken into consideration as ±2 SD.

Table 3.2 Measurement accuracies associated with sensors

Sensors	Range	Accuracy
Pressure		
Turbine inlet pressure	0–7 bar	±5%
Differential pressure across	0–0.1 bar	±2.5%
diaphragm for flow measurement	0–1 bar	±2.5%
(two sensors for different capacity of flow)		
Nozzle inlet	0–5 bar	±2.5%
Stator and rotor	0–0.5 bar	±2.5%
Temperature	−55 °C to 125 °C	±0.5 C
Load cell	0–750 g	±0.5 g
Rotational speed sensor	—	±0.01%

3.1.3 Results and Discussion

In this section, test results for different configurations according to Table 3.1 are discussed. All tests are performed with two nozzles because at a time two nozzles out of eight nozzles could be activated in the current stator arrangement. Total thickness of the rotor and stator is kept same for all the tests by selecting different number of disks in case of different gap and disk thickness.

Table 3.3 Test rig on-design data at best efficiency configuration(20mm inner disk diameter, 0.2mm gap between disks)

Speed, rpm	Mass flow, g/s	Pressure at nozzle upstream, barg	Efficiency, %	Power, W
40,000	3.5	1.52	6.1	14.8
40,000	4.7	2.25	11.1	44.1
40,000	5.8	3.05	13.9	79.7
40,000	7.1	3.91	15.5	119.6
40,000	7.6	4.30	15.7	136.7

Performance of Tesla prototype for one particular configuration is tabulated in Table 3.3. We can see that power of the turbine increases with mass flow with no peak power seen in the Table 3.3 . Similar trend is observed with efficiency in some cases. This may be because the turbine is not operated at its full capacity as the nozzle gets choked. Loss characterization (presented in next section) inside the turbine will help to understand behaviour of the performance in depth.

Effect of exhaust area

Back pressure of the turbine has significant effect on performance of the machine. This is varied by drilling additional holes axially (Figure 3.2: *q*) for fluid to discharge along with primary discharge holes (Figure 3.2: *l*) Primary discharge holes area is denoted as A1 and total area along with additional drilled holes is denoted as A2. In Figure 3.3, we can see that additional exhaust area has increased performance of the turbine significantly, specifically at higher flow rate. At lower flow rate, inlet pressure is lower and exit velocity at the disk inner tip is lower. This high swirling exit flow is weaker in strength than exit swirling flow created due to higher mass flow. Additional axial holes aids in reducing back pressure. The effect of reduction of backpressure is more evident at higher mass flow rate conditions as expected. This is why efficiencies show higher gain at higher mass flow. Therefore, design of exhaust system plays important role in the development of a Tesla turbine.
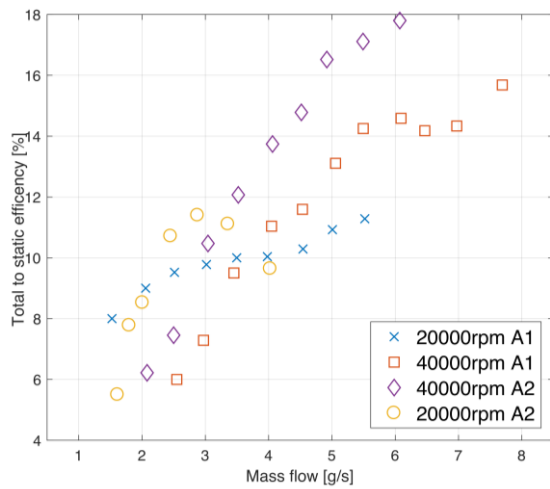
Figure 3.3 Variation of total to static efficiency versus mass flow for different exhaust area A1 and A2 for two different speeds
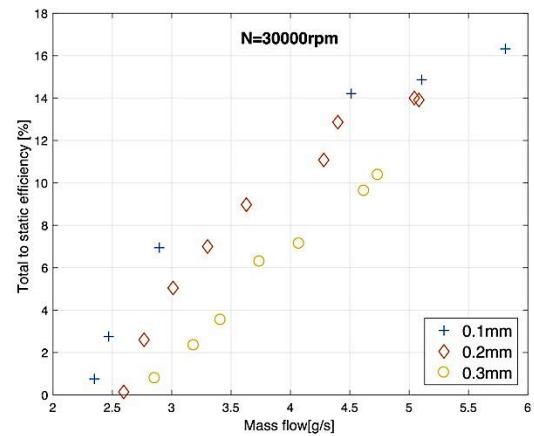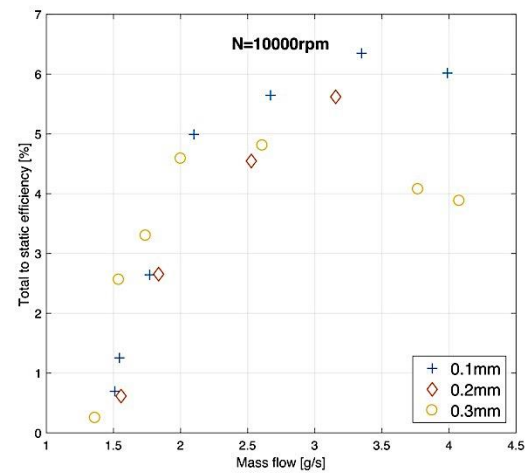
Figure 3.4 Variation of total to static efficiency versus mass flow for different thicknesses of disks at 10,000 and 30,000 rpm

Effect of disk thickness

Effect of disk thickness has been studied numerically but detailed experimental investigation has not been performed in literature. Tests are carried out for three different disk thicknesses. In Figure 3.4, it can be seen that at lower rotational speed and low flow, effect of disk thickness is not significant on turbine performance, but at higher flow disk thickness plays an important role. At higher flow, efficiency is higher with lower disk thickness.

At higher rotational speed and lower flow, there is significant effect of disk thickness over performance of turbine. If we compare results at different rotational speeds, it can be seen that at higher rotational speed disk thickness should be as small as possible. In fact, Sengupta and Guha (2018)[25] studied the effect of disk thickness numerically and showed that at higher rotational speed turbine performance is higher at lower disk thickness. We can describe this behaviour in following way. The length of the nozzle is summation of disk thickness and gap for all the disks. When disk thickness is zero, entire flow out of the nozzle sees the same cross section at rotor inlet. In this case we do not expect any major change in the velocity of the fluid. However, when disk thickness is finite, flow area at the rotor inlet decreases, which changes the radial inlet velocity at the rotor. At higher rotational speed and high mass flow, fluid velocity is high. Contraction of area due to finite disk thickness creates more losses. This explains the sensitivity of disk thickness at higher mass flow and higher rotational speeds, which is in accordance with the literature studies.

Effect of gap between disks

Gap between disks is one of the most important geometric parameters in the performance of a Tesla turbine. Tests are carried out for three different disks spacing. Results show that there is optimum value of the gap width for different speeds of the turbine and inlet conditions. In Figure 3.5, we can see that when gap between disks is high, 0.3 mm, for lower rotational speed, at same mass flow, performance of the turbine is better. While at higher mass flow efficiency decreases compared to higher rotational speed. Gap width also affects the leakage around the end walls based on pressure drop across rotor. For lower gap, pressure drop across rotor will be higher and hence more flow will bypass the rotor leading to lower performance. This can be the reason why 0.1 mm gap between disks shows lower efficiency. However, there is an optimum gap which depends on both rotational speed and mass flow rate of the turbine, and which can be determined basing on design considerations (flow through the disks) as well as practical considerations (leakage flow bypassing the rotor, also a function of degree of reaction)
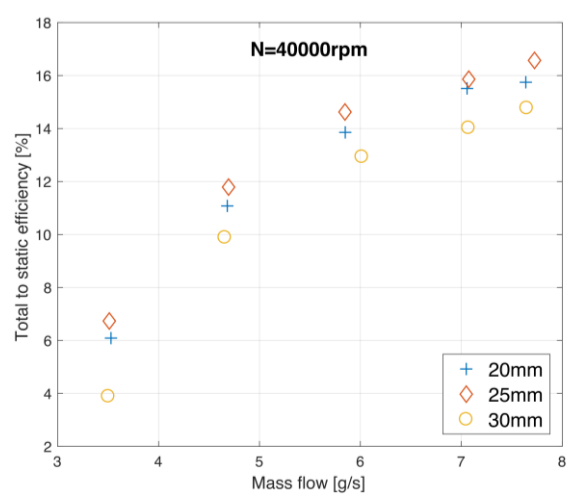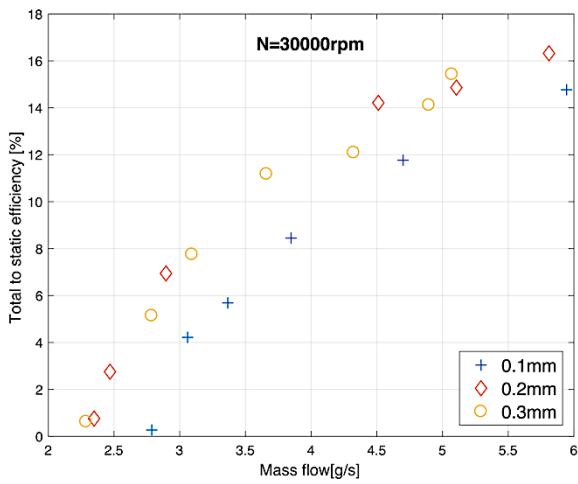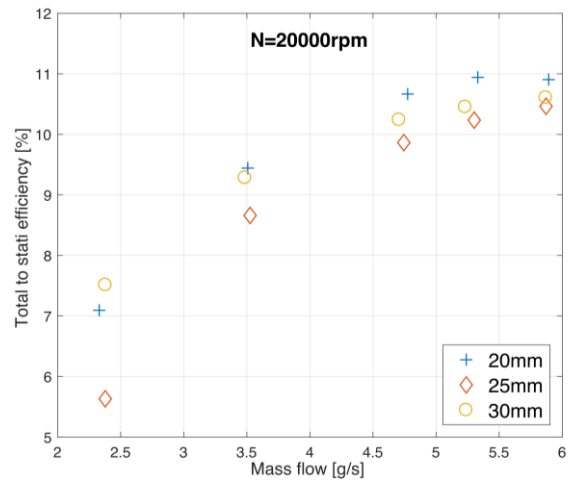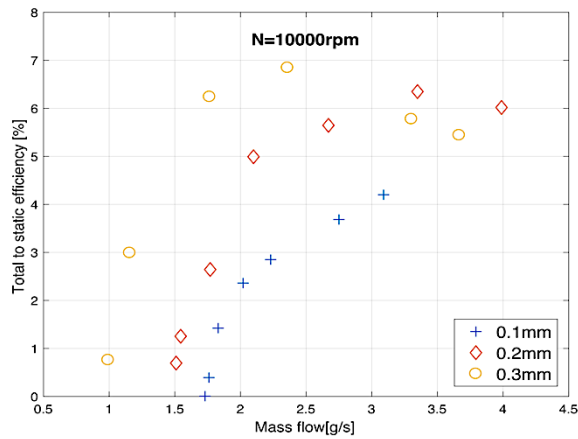
Figure 3.5 Variation of total to static efficiency versus mass flow for different gaps between disks at 10,000 and 30,000 rpm

Figure 3.6 Variation of total to static efficiency versus mass flow for different disk exit diameters at 10,000 and 30,000 rpm

Effect of disk inner diameter

Radius ratio of a disk is varied by fixing the outer diameter and changing inner diameter of disks (i.e. the outer diameter of discharge holes). There are three inner diameters for which tests are performed. We can see in Figure 3.6, variation of total to static efficiency with respect to mass flow for two different speeds. It has been observed that small inner diameters are performing better at lower speeds (< 25000 rpm) and medium diameter configuration till 30000 rpm. Although there is an optimum value for inner disk diameter, the dependence on efficiency

on inner disk diameter is relatively weak. The best compromise between the active surface and radial velocity loss at the exit.

3.2   Air 3kW Tesla Expander Prototype

In this section, a larger-size prototype is designed by introducing novelties based on observations from the previous 100 W machine. This is the first ever Tesla turbine built with an integrated high-speed generator in a single housing (Figure 3.7), which makes it compact and easier for tests. An experimental campaign is carried out to assess the performance of the turbine. Therefore, objectives of this prototype are: (i) Demonstration of modular Tesla turbine with flexible test rig with integrated high-speed generator (ii) Assessment of nozzle number on the performance of the turbine and (iii) Experimental characterization of losses (covered in Chapter 4).

3.2.1 Turbine Components and Experimental Set-up

The test rig used to characterize Tesla expander performance is shown in Figure 3.8. The working fluid is dehumidified air in order to avoid condensation in the rotor. The test rig consists of expander and high-speed generator in single shaft arrangements, turbine casing support, air feeding system, mass flow controllers and power dissipation system. The Tesla turbine prototype used in this experimental campaign is carefully designed considering previous experience with 100 W prototype. The rotor is designed using the 0-D design tool. Table 3.4 shows the geometrical parameters of the turbine. The rotor consists of flat, smooth disks with central opening for exhaust. The constant gap between disks is maintained using spacers. The entire shaft is supported by ball bearings placed at the ends of the generator while the turbine is cantilever. The turbine has two exhaust outlets. Air from one of the exhaust outlets is used as cooling fluid for generator.

The high-speed generator is fitted in the same casing and connected to turbine shaft as shown in Figure 3.7. Generator performance data is given in Table 3.4. The high-speed generator is used to apply load on the turbine by maintaining constant rotational speed. The power generated by the turbine is dissipated through thermal load resistors. The turbine is fed through

air connection lines which comes from the three mass flow controllers. These mass flow controllers are used to feed desired amount of air in the turbine with high accuracy.
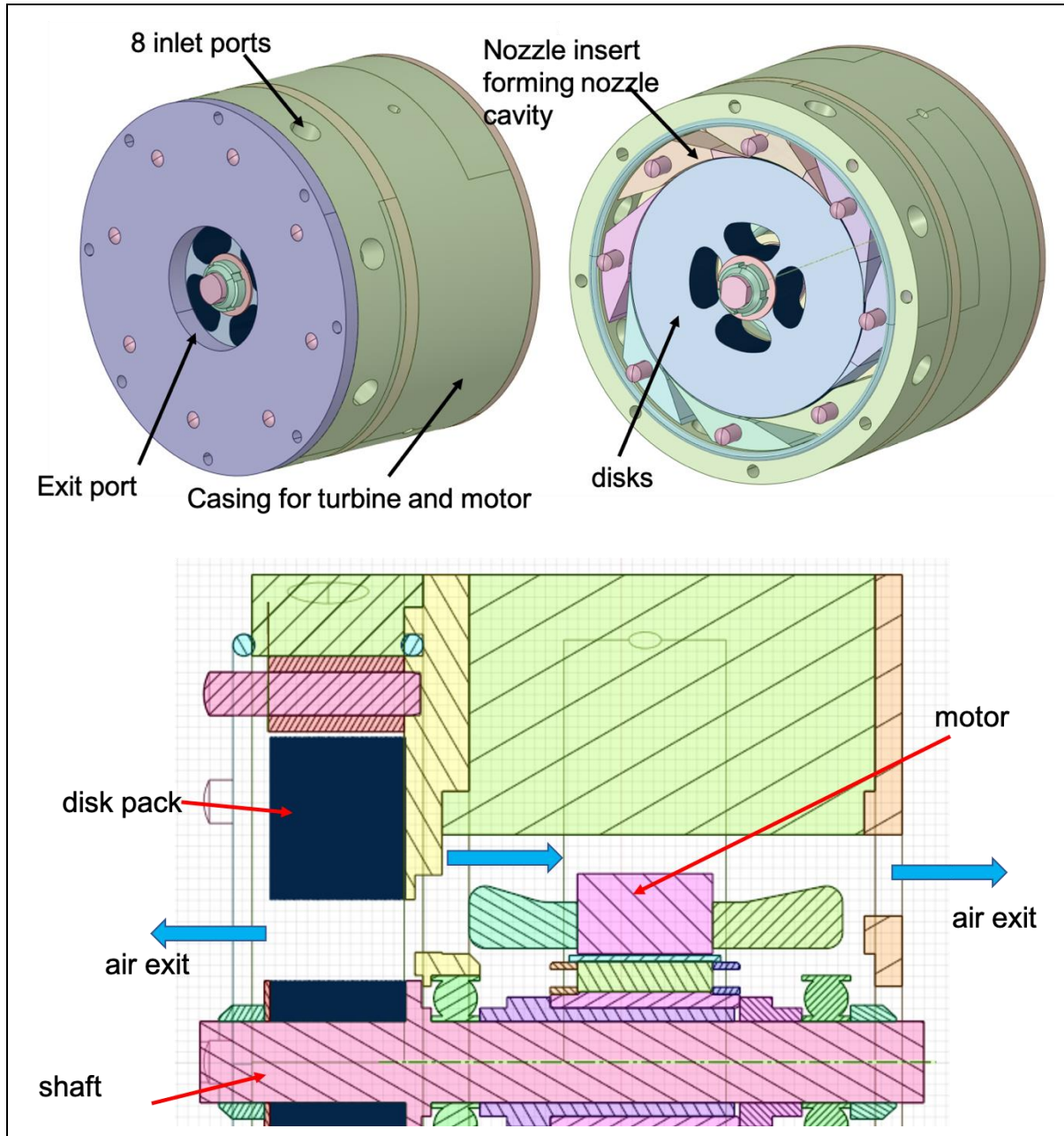
Figure 3.7 3D drawing of air 3kW expander showing different components

The turbine is flexible to change number of disks, gap between disks and the geometry of the nozzle without changing the other turbine components. The nozzle geometry is designed to allow tangential flow at the entry of the rotor, small clearance between rotor and stator and minimum frictional losses. The nozzles are manufactured and assembled in such a way that it

is easy to change these nozzle inserts when required, as shown in Figure 3.8(i). The complete stator thickness is equal to that of the pack of disks and spacers. The end disk and the casing wall are maintained at a clearance to avoid high leakage flow and viscous friction loss. There are total 8 nozzles. In this study, performance with 1, 2 and 4 nozzles have been investigated.
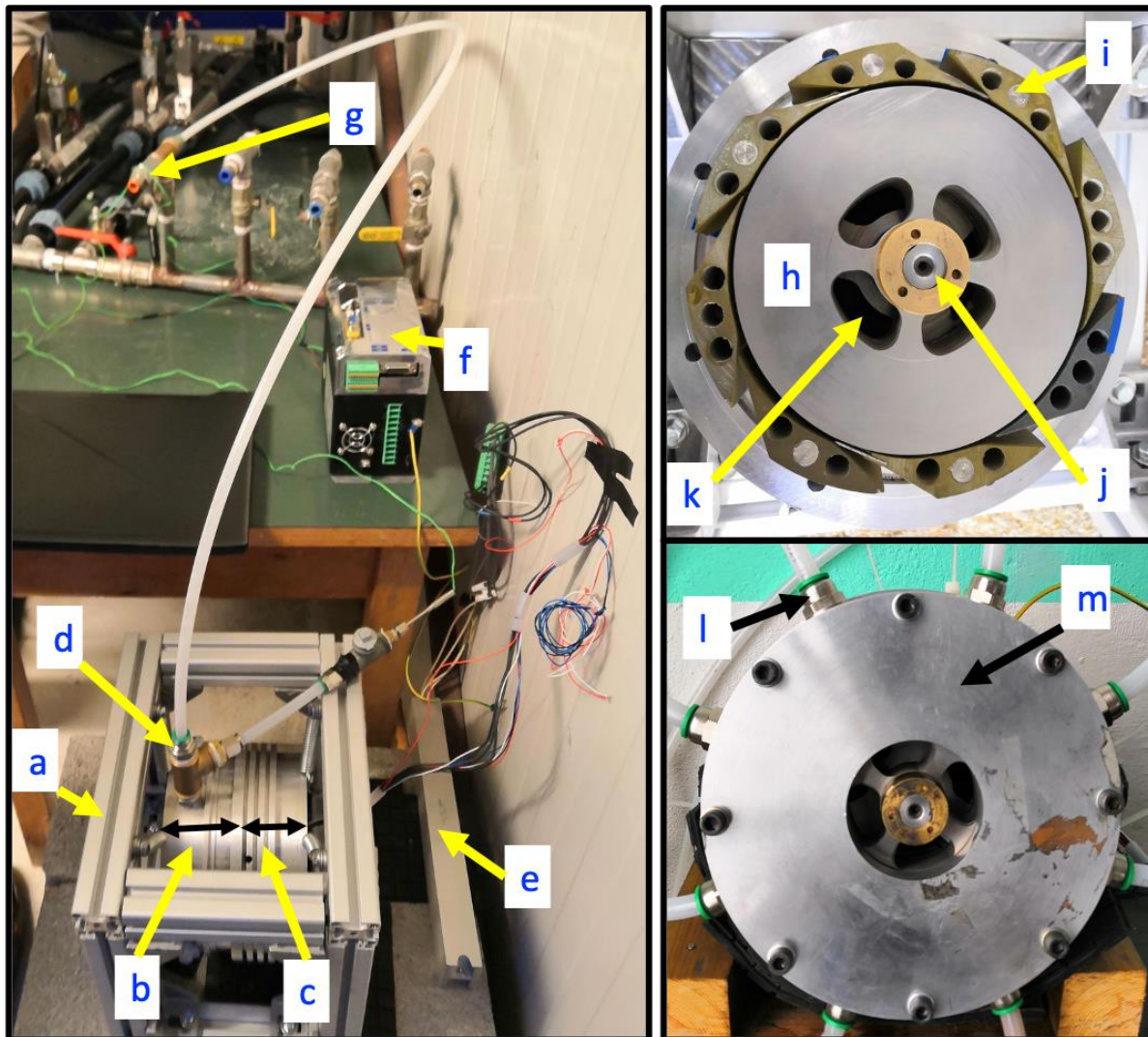
Figure 3.8 Experimental test rig: (a) turbine support; (b) casing with turbine; (c) casing with generator; (d) inlet connection to turbine; (e) thermal resistance to dissipate generated power; (f) generator controller; (g) flow divider for two nozzles; (h) turbine rotor disks; (i) nozzle; (j) rotor shaft; (k) exit holes for air exhaust; (l) nozzle inlet ports; (m) turbine front casing

Table 3.4 Turbine geometrical data and generator performance data

Turbine	
Outer diameter of disk, mm	120
Inner diameter of disks, mm	60
Number of nozzles	1, 2 and 4
Gap between disks, mm	0.1
Disk thickness, mm	0.1
Number of disks	120
Inlet flow angle, degree	2.2
Type of nozzle	Convergent
Generator @rated point	
Power, kW	3
Speed, rpm	40000
Efficiency, %	96
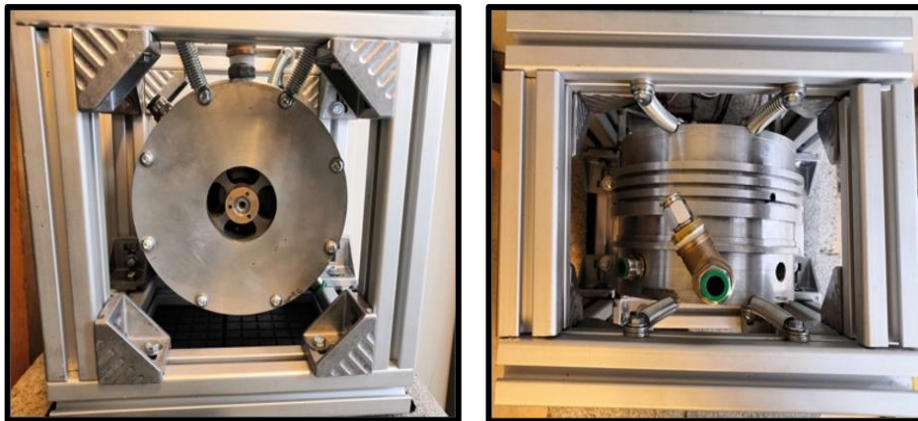
Figure 3.9 Front and top view of turbine casing support structure with springs

The casing houses turbine and generator, on which shaft line is equipped with two end plates on either side for assembly and maintenance, as shown in Figure 3.8(m). The entire casing is supported using 4 springs which are connected to main supporting structure as shown in Figure 3.9. This arrangement allows easy access to all air feeding lines (through 8 ports) and decouples the vibrations of the turbine from the resonances of its support.

Measurement System

The experimental test rig is built to measure parameters necessary to determine the performance of the turbine. Air is taken from compressed air line to the inlet of mass flow controllers after passing through dehumidifiers. Three mass flow controllers and meters are used to get the required mass flow rate. Air then passes through a flexible pipe till inlet of the nozzle. Pressure and temperature are recorded at the inlet of the nozzle. K-type thermocouple and pressure sensors are placed in the fitting just before the entrance of the nozzle. Temperature measurement is done also at the outlet of the turbine. Static pressure is measured at the exit of the nozzle by a pressure sensor placed at the next unused nozzle.

Table 3.5 Measurement accuracy of sensors

Sensors	Range	Accuracy
Pressure		
Nozzle inlet	0 - 16 bar	±2.5%
Stator and rotor	6-600 mbar	±1%
Mass flow meter		
Mass flow meter 1	1500 ln/min	±1%
Mass flow meter 2	1500 ln/min	±1%
Mass flow meter 3	2000 ln/min	±1%
Temperature	-55 C to 125 C	±0.5 C
Current measurement by generator for torque	0 to 9 Amp	±0.5
Speed sensor in generator	8000 to 60000 rpm	±0.01 %

High speed generator driver is used to record rotational speed and power. Load on the turbine is applied by controlling the speed of the generator. All sensors and generator are connected to the common data acquisition system through which all data is recorded and controlled. Table 3.5 shows the measurement accuracies of various sensors used in the measurement system.

Performance of the turbine is evaluated in terms of total to static efficiency and power. The thermocouples at the exhaust of the turbine measure the static temperature (i.e. not considering the fluid speed contribution), while pressure is the ambient one. Since the turbine is not

provided with exhaust system to recover kinetic energy at the disk outlet, it is not possible to calculate or derive the total temperature and total pressure at the exhausts. Knowing the total properties at the entrance and those at static discharge, we considered the parameters useful to the calculation of the performance as total to static.

The power of the turbine is directly obtained from data collected from generator. Generator manufacturer has provided correlation between current generated and conversion factor to derive the torque. Also, generator efficiency varies with rotational speed and output power. The mechanical power output from the turbine is calculated by considering the generator losses. It is therefore possible to calculate the mechanical power using torque of the rotor and angular velocity as:

$$P_{exp} = \frac{\tau.\omega.}{\eta_g}$$

(3.10)

Uncertainty analysis on complete data leads to maximum error in efficiency as $\pm 1.8\%$ with 95.5% confidence interval.

3.2.2 Results and Discussion

Several attempts were made for the smooth operation of the Tesla expander due to operational difficulties encountered. Initially, compressed air is passed through the turbine to avoid heating of generator coil. Then, turbine rotor is set to a constant rotational speed which is controlled through generator driver.

Attempt 1: Turbine was made to run at 30000 rpm and inlet mass flow was varied to record performance. When turbine speed was around 10000 rpm or lower, a disk rubbing noise started coming along with smoke. When turbine was opened, it was found that end disks rubbed against the casing wall. There was a pattern of hot spots on the end disks as shown in Figure 3.10. By initial inspection at the spot pattern on the disk, we concluded that it may be due to disk fluttering. We changed the end disks and performed the experiment again. We observed a similar behaviour of failure of end disks in the same way. Further investigation through CFD and Finite Element Modelling (FEA) revealed that the initial guess was right. When disk rotates

at high speed, centrifugal forces on the disks keep it straight. CFD results showed that there was a pressure variation across end disks due to leakage flow between extreme disks and casing. The axial pressure difference on the disk tip area generated a force in the direction of the casing. This force overcome the centrifugal force of the disk at lower speed. In order to avoid fluttering of disks at lower rotational speeds, a novel method is applied to mitigate the problem by introducing specially featured end disks. As a result, the new rotor used for the following tests has been modified against the Table 3.4 data (number of disks have been reduced with respect to the original number and two specially featured end disks added at the extremes).

Figure 3.10 Rotor failure at low rotational speeds (a) casing after disk fluttering (b) end disk failure (c) breakage of end disk tip due to hot spot generation

Attempt 2: After introducing end disk fluttering mitigation mechanism inside the rotor, we observed that turbine ran without any noise or any disk flutter even at lower rotational speeds with air fed to nozzles. When turbine was run at higher rotational speeds, ~ 33000 rpm, rotor

became unstable and rotor started vibrating with high amplitude leading to failure of bearings. A study on this revealed that there was a change of natural frequency of the rotor and unbalance in the rotor due to end disk mitigation mechanism. This was one of the reasons which leads to change in critical speed of the rotor, leading to resonance at ~ 33000 rpm.

Attempt 3: Rotor was carefully balanced along with end disk flutter mitigation mechanism. In this attempt turbine worked for entire speed range of the test without any issues. Tests were carried out for different loads applied to the turbine using generator. Mass flow rate in the turbine was varied using mass controller and readings are recorded for different rotational speeds.

Table 3.6 shows the maximum efficiency points for 1, 2 and 4 nozzles configuration. In both the cases, maximum efficiency was obtained for low rotational speed, and efficiency drops at higher rotational speeds. Maximum turbine total to static efficiency of 36.5% is recorded for two nozzle case, which is the highest efficiency achieved till date for Tesla turbine prototypes with air as a working fluid. By measuring the nozzle exit pressure, it was possible to characterise the losses in the nozzle and its impact on the performance (detailed analysis of losses can be found in Chapter 4).

Table 3.6 Maximum efficiency points for one nozzle and two nozzles tests

Speed	Mass flow	Pressure at nozzle upstream	Efficiency	Power
rpm	g/s	bara	%	W
1 Nozzle				
10000	24.7	2.00	27.9%	376.3
2 Nozzles				
10000	24.7	1.35	36.5%	224.5
4 nozzles				
10000	49.0	1.59	22.7%	397.3

Figure 3.11 shows the mass flow and reduced mass flow variation with inlet nozzle pressure for different number of nozzles. We can see that mass flow rate of four nozzles is slightly less than the 4 times mass flow rate for one nozzle. This is may be due to the higher back pressure at nozzle exit (clearance between rotor and stator) in case of 4 nozzles configuration, as shown in Figure 3.11. This increase in back pressure caused higher pressure difference in the end-
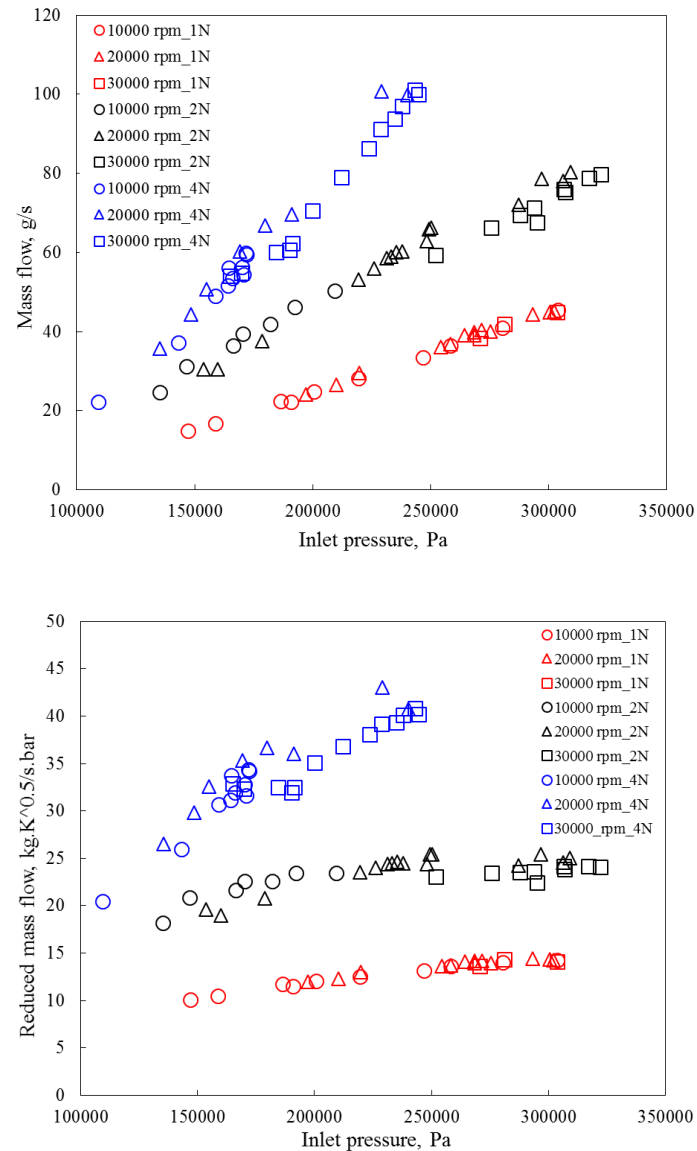
Figure 3.11 Variation of mass flow and reduced mass flow vs nozzle inlet pressure for different rotational speeds for 1, 2 and 4 nozzles configuration

-gaps leading to higher leakage flows. It also shows the choking of the nozzle with respect to inlet pressure. Nozzles starts choking at 2.5 bar inlet pressure and it attains sonic conditions. However, at the exit of the nozzle there is sudden increase in area due to clearance between nozzle and rotor. This increase in area immediately after the throat leads to further expansion of the air creating a supersonic flow condition along with shock waves. This supersonic flow may cause additional total pressure losses which are discussed in the following section, and which may significantly affect the performance of turbine at high flow conditions.

Nozzle loss characterisation using nozzle loss coefficient and nozzle efficiency parameter helps to understand performance behaviour of Tesla turbine. We will see (section 4.2.2) that nozzle losses are higher for higher rotational speeds and inlet pressure. The other major sources of loss include ventilation, leakage and exhaust losses. It is shown that viscous fiction between end disk and casing is significant at high rotational speeds. Leakage flow can be as high as 40% (preliminary estimation based on 100W prototype) depending on the pressure between stator and rotor gap. Nozzle losses together with ventilation and leakage losses influence strongly the peak efficiency of curves.
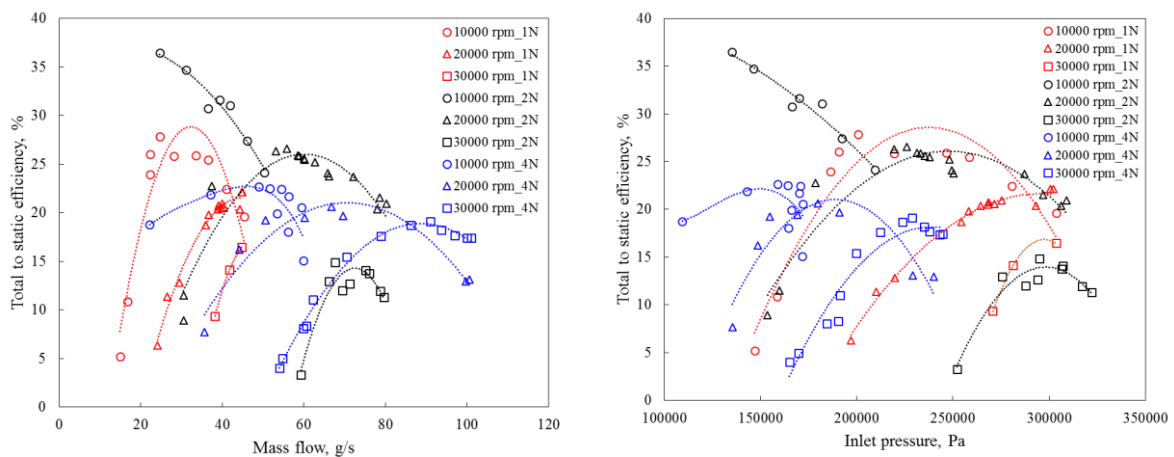
Figure 3.12 Variation of total to static efficiency vs mass flow and nozzle inlet pressure for different rotational speeds for 1, 2 and 4 nozzle configurations

Figure 3.12 shows the experimental results for total to static efficiency for 3kW Tesla machine for different number of nozzles. The first observation is that the peak efficiency of the turbine is at low rotational speeds and it decreases at higher rotational speeds. The CFD of this machine

shows the peak efficiency obtained at higher rotational speeds. Hence, the main reason behind this trend is due to high ventilation losses, leakage and exhaust losses.

Figure 3.12 also shows that efficiency with two nozzles is higher than 1 and 4 nozzle cases. Guha and Sengupta [25] have shown by numerical analysis that efficiency of the turbine increases with number of nozzles at constant mass flow. In fact, as number of nozzles increases, inflow condition to the rotor is more uniform and tangential velocity distribution is more axisymmetric. However, we see that experimental efficiency is maximum for two nozzle configurations at constant mass flow condition.
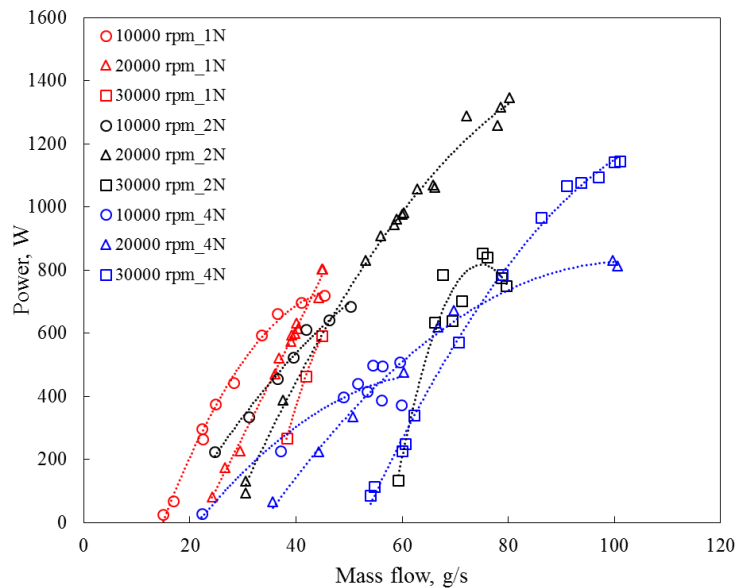
Figure 3.13 Variation of turbine power vs mass flow for different rotational speeds for 1, 2 and 4 nozzles configuration

According to Guha's numerical analysis, the performance of the four nozzles configuration should have been better. We can explain this behaviour with following hypothesis. Numerical analysis does not consider leakage losses. Nozzle exit pressure in case four nozzles, for the same mass flow condition, is higher. This creates higher pressure difference across the turbine between end disk and casing. The leakage flow across the turbine is higher than 2-nozzle configurations. This leakage flow has significant impact on the efficiency of the turbine at 4-nozzle configuration. This is also evident in power curve as shown in Figure 3.13 where lower power is obtained in case of 4-nozzle case at same mass flow conditions.

3.3 Water 1kW Tesla Expander Prototype

3.3.1 Turbine Components and Test Rig

In this section, experimental tests of water expander with "Ultra-Efficient" Tesla rotor design is presented. The turbine specifications are reported in Table 2.4. The different components of the water expander can be seen in Figure 3.14. The turbine consists of following main components:

1. Inlet port: inlet port is the inlet piping connection for the water to enter into the turbine. Water from inlet port enters into nozzles. There are two inlet ports used in this turbine.

2. Stator: there are 24 nozzles placed around the circumference of the rotor, which increase the velocity of the incoming water. High-speed jets of water enter into the rotor. Stator is manufactured using 3D printing technology into one single piece.

3. Rotor: turbine rotor consists of metal thin disks parallelly mounted on the shaft. The disks are separated by spacers, which maintain the desired gap between disks along with rotating shaped disks, as discussed in previous chapter.

4. Radial diffuser: radial diffuser at the exit of the turbine is used to convert exit kinetic energy of the water into pressure energy.

5. Collector: the water coming out of radial diffuser has tangential velocity and to redirect the flow into single channel/pipe, collector is used. The role of collector is to smoothly transfer water from radial diffuser to exit pipe.

This Tesla turbine was designed to operate at speeds up to 10,000 rpm. Given the need to seal the turbine casing, the rotor has a cantilevered (as shown in Figure 3.15(b)) arrangement to allow the use of a single mechanical seal. The mechanical seal has been placed to avoid the water exit where the 15mm diameter shaft is coming out the turbine casing for connecting to the generator through a joint. The rotor is supported by three spindle bearings placed on the generator side between the mechanical seal and the joint, while on the opposite side the cantilevered disc pack is held together by a shaped ring nut. The turbine has 3 chambers: the cylindrical inlet manifold, connected externally to the 2 inlet pipes, surrounds the stator and the chamber containing the rotating discs, finally the liquid that comes out of the turbine is

collected in an exhaust manifold and exits from the 2 pipes drain. All the machine components are kept together by flanges and 6 threaded rods with a 12mm diameter.

Figure 3.15(c)(d) shows the rotor and stator assembly. Stator is made with plastic as well as metal using 3D printing technology. Figure 3.16 shows the whole assembly of the expander with inlet and exhaust piping arrangements. Following measurements are done to evaluate performance of the turbine – inlet pressure, outlet pressure, mass flow using ultrasonic instrument for greater accuracy and generator power using current and torque convertor factor provided by the manufacturer.
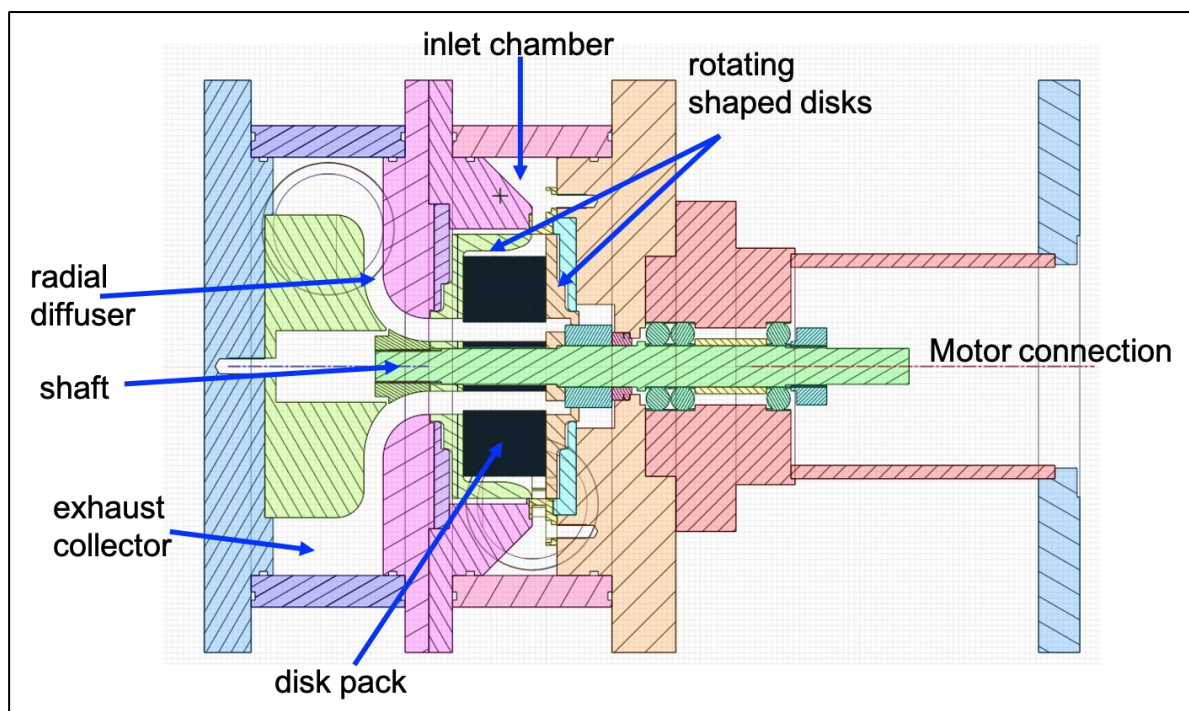
Figure 3.14 3D drawing of water 1kW expander
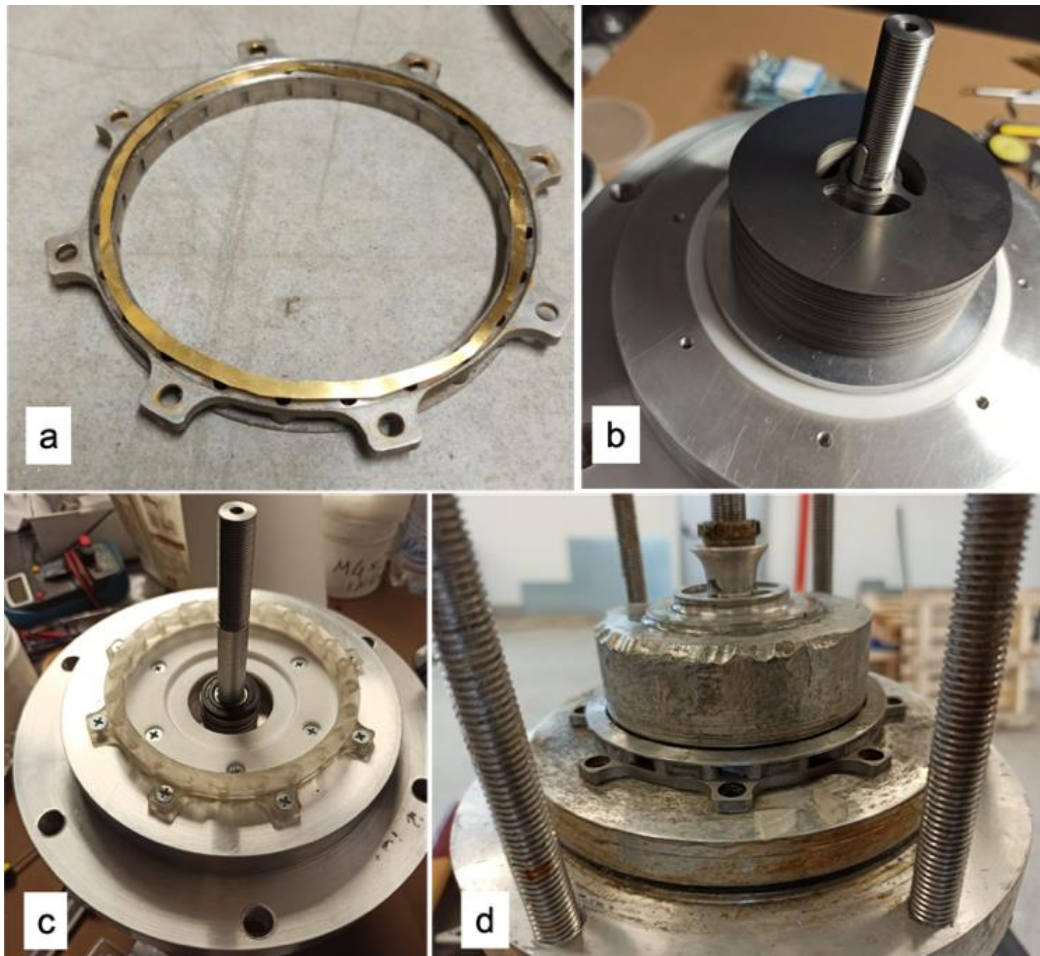
Figure 3.15 Water Tesla expander components: (a) metallic stator, (b) rotor assembly, (c) rotor with plastic stator, (d) rotor with metallic stator

Water test rig set up: Water test rig is the set-up of piping required for the water circulation through turbine. The inlet pressure to the turbine is provided by high pressure water pump to maintain 14 bar pressure difference between turbine inlet and turbine exit as shown in Figure 3.17. The water test rig system is controlled by various valves to control the operation of the system.
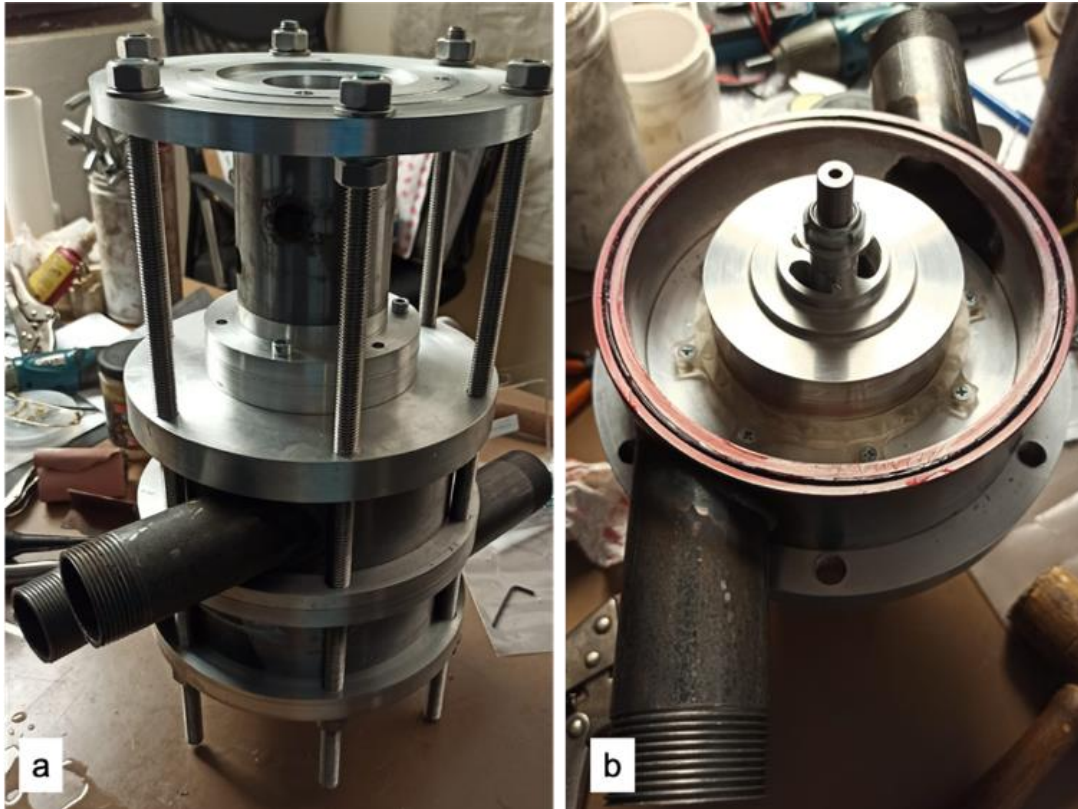
Figure 3.16 Water expander: (a) assembly, (b) turbine showing rotor and inlet ports

Figure 3.17 Water expander experimental test rig

3.3.2 Results and Discussion

Test 1: Experiments are conducted for various pressure drops across the turbine, i.e. 2 bar to 15 bar inlet pressures. The generator attached to the turbine records rotational speed and current. The power is calculated using current and torque coefficient (obtained from manufacturer for generator used).

Figure 3.18 and Figure 3.19 show the mechanical power produced by the turbine for different rotational speeds and mass flows. The dashed lines represent the power without ventilation losses (experimentally measured, as discussed in Chapter 4) and solid lines represents the actual recorded power. We see that major source of losses are ventilation losses. This is due to the large surface area available at the interface between rotor and casing. Similarly, Figure 3.19 shows the cases of the power for 100% and 90% flow (at the maximum pressure produced by the pump, 13 bar) through the turbine with respect to rotational speed. The dashed line, which are power without ventilation loss, shows increasing trends and may have peak at higher rotational speeds. It means that turbine will have high performance if ventilation losses are reduced significantly (which can be reduced through conventional solutions).

Similar trends can be seen in the efficiency plots as show in Figure 3.20 and Figure 3.21. The dashed lines represent performance without ventilation loss, which shows promising higher values. Also, with respect to rotational speeds, these curves tend to show increasing trends for higher rotational speed i.e. towards design speed of 10000 rpm.

The trends shown in the experimental results are promising as they indicate the possibility of higher performance at higher speed and mass flow. The turbine is designed for 14 bar pressure difference, 2 kg/s mass flow rate and at 10000 rotational speed. In the present test campaign turbine could not produce desired mass flow at pressure difference of 14 bar. This is due to the undersized nozzles (tolerance errors in 3D printing of nozzles – manufacturing limitation to have small nozzle dimensions). The analysis of ventilation loss which is the man cause of lower turbine performance is primary focus of further investigation for this prototype.
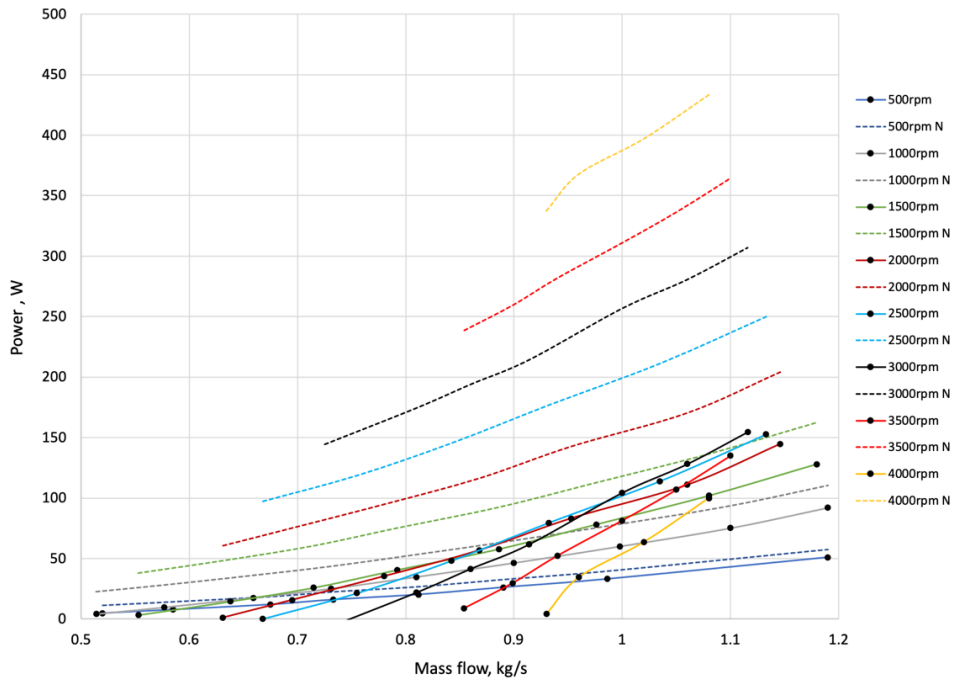
Figure 3.18 Constant speed curves showing power versus mass flow
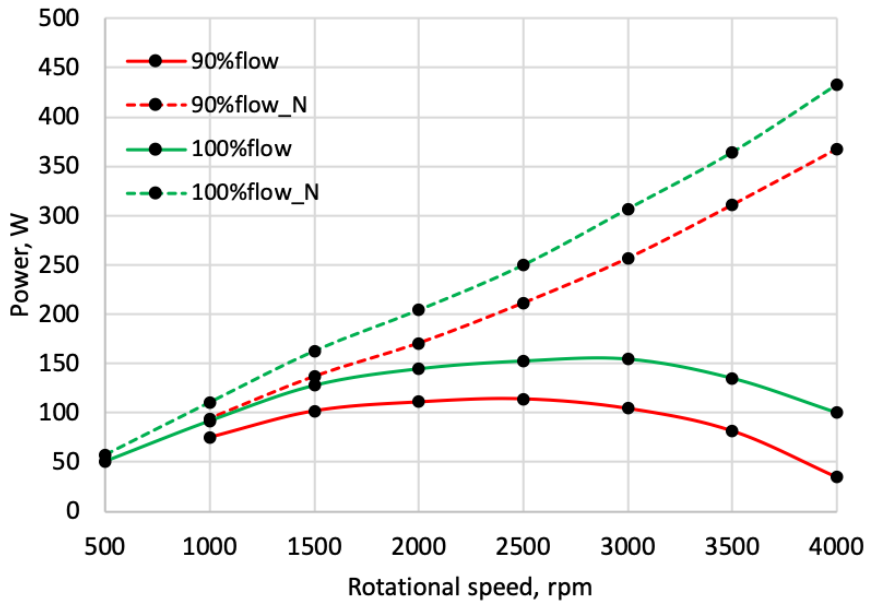
Figure 3.19 Mechanical power vs rotational speed at different flows i.e. 90% and 100% of
water pump speed (100% pump speed corresponds to 1.1 kg/s mass flow)
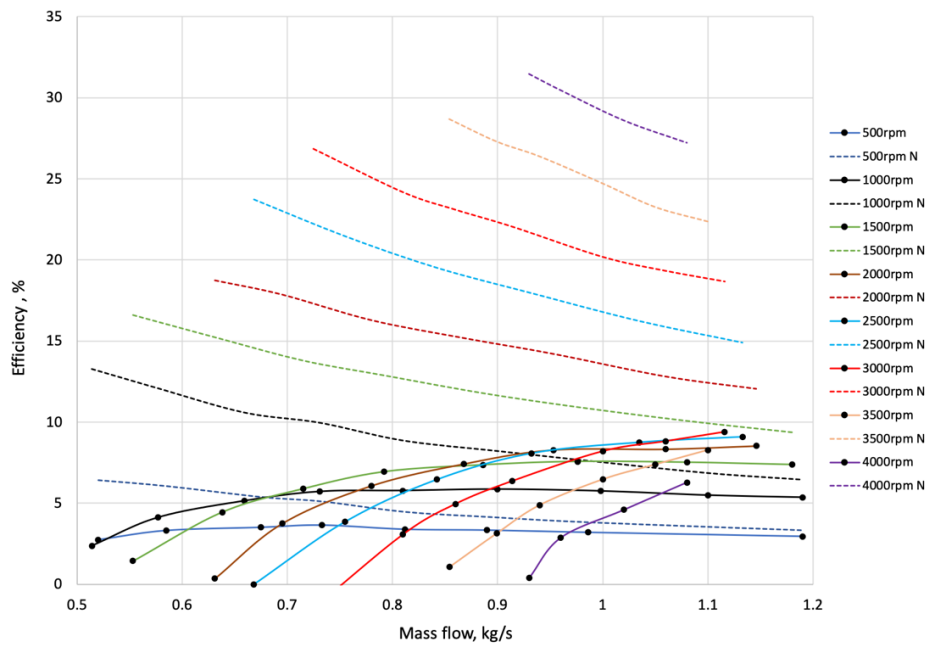
Figure 3.20 Constant speed curves showing Efficiency versus mass flow
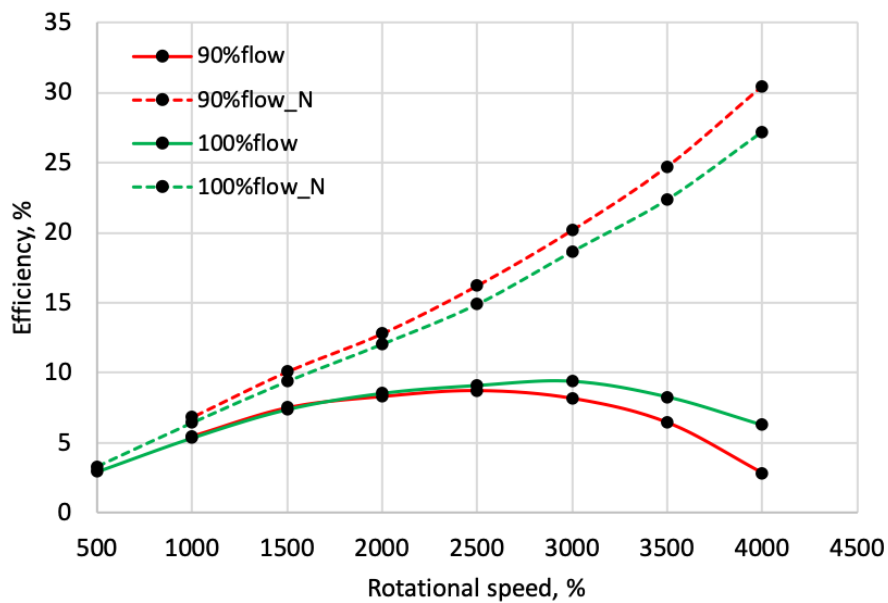
Figure 3.21 Efficiency vs rotational speed at different flows i.e. 90% and 100% pump speed (100% pump speed corresponds to 1.1 kg/s mass flow)

Test 2: In the previous experimental test, 3D printed nozzles with 0.4 mm throat height was used. This throat section was deigned based on the required mass flow and pressure difference. However, in the test, at14 bar of Δp, mass flow of 1.1 kg/s was obtained. In the analysis on the turbine it was found that there were two main reasons for such low mass flow.

i.   Due to very small dimensions, 3D printing produced higher tolerances making effective total nozzle area smaller than designed one – in the new test nozzles are printed with higher throat height (~ 0.8mm)

ii. Leakage flow from inlet plenum chamber (before the nozzle ring) to inside the casing via contact between nozzle ring and the casing - Provisions are made in the new nozzle ring to insert static seals (gasket/O-ring) between nozzle ring and casing to minimize leakage.

In the thorough turbine inspection, it was also found that the geometry of rotating shaped end disks was not manufactured as per drawings. In the new test, the rotating shaped end disks were also manufactured in order to align it with the drawings.

In the new test, important changes were made as discussed before, however, no improvements were carried out to tackle the ventilation loss issue to assess the causes separately and systematically. Figure 3.22 shows the pressure difference across turbine versus mass flow for
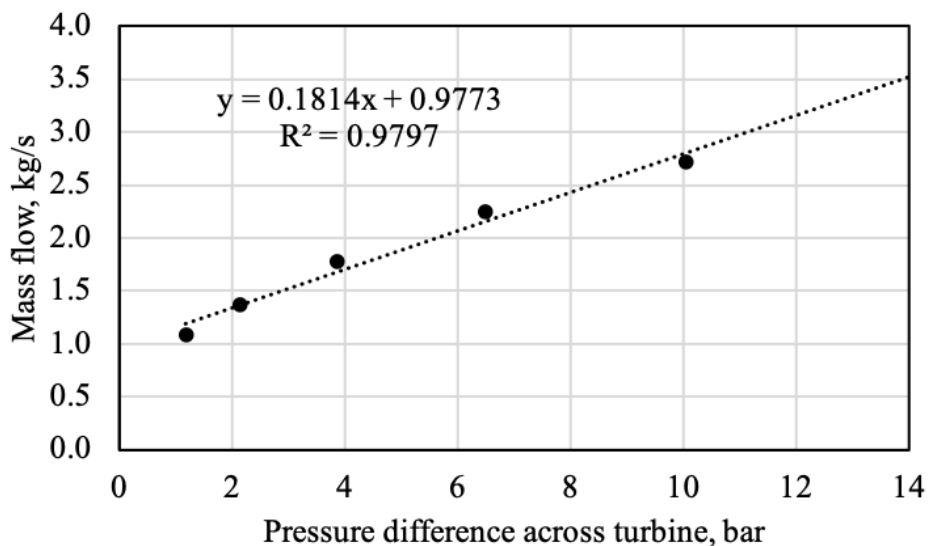
Figure 3.22 Pressure difference across turbine versus mass flow for water 1kW expander

new tests. It can be seen that with new nozzle higher mass flow is obtained compared to previous tests for same Δp. This indicates that the leakage between nozzle ring and casing is significantly reduced and the new 3D printed nozzles may have larger throat section due to 3D printing tolerances which increases mass flow more than double than the design values.

New tests were also performed in similar way as previously discussed. Figure 3.23 and Figure 3.24 shows the performance results i.e. efficiency and power versus rotational speed with different mass flows. It can be seen that there is significant improvement in the performance of the expander reaching maximum efficiency of ~30% (10% in old test) with power of 690 W (150 W in old test). One of the main reason for high performance is the changes in the rotating shape end disk which is made according to design in the current test.
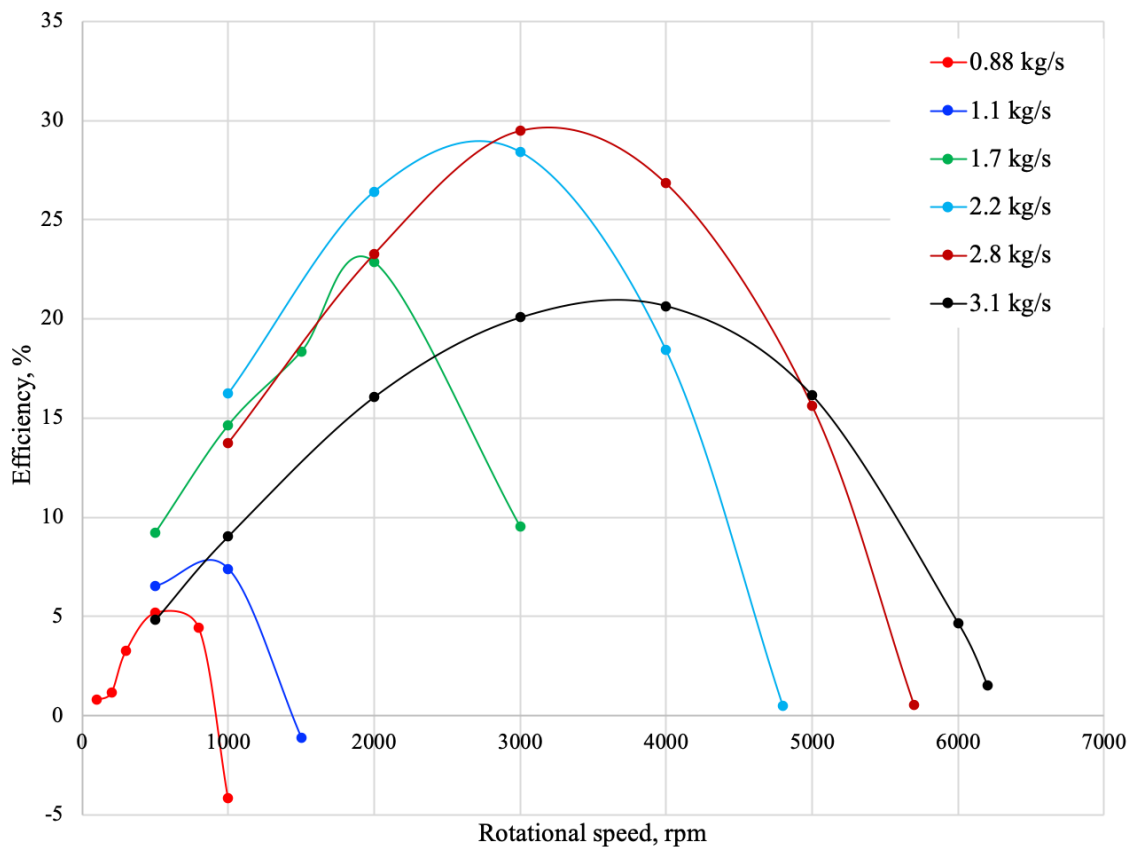
Figure 3.23 Total to static efficiency versus rotational speed at different mass flow for water 1kW expander
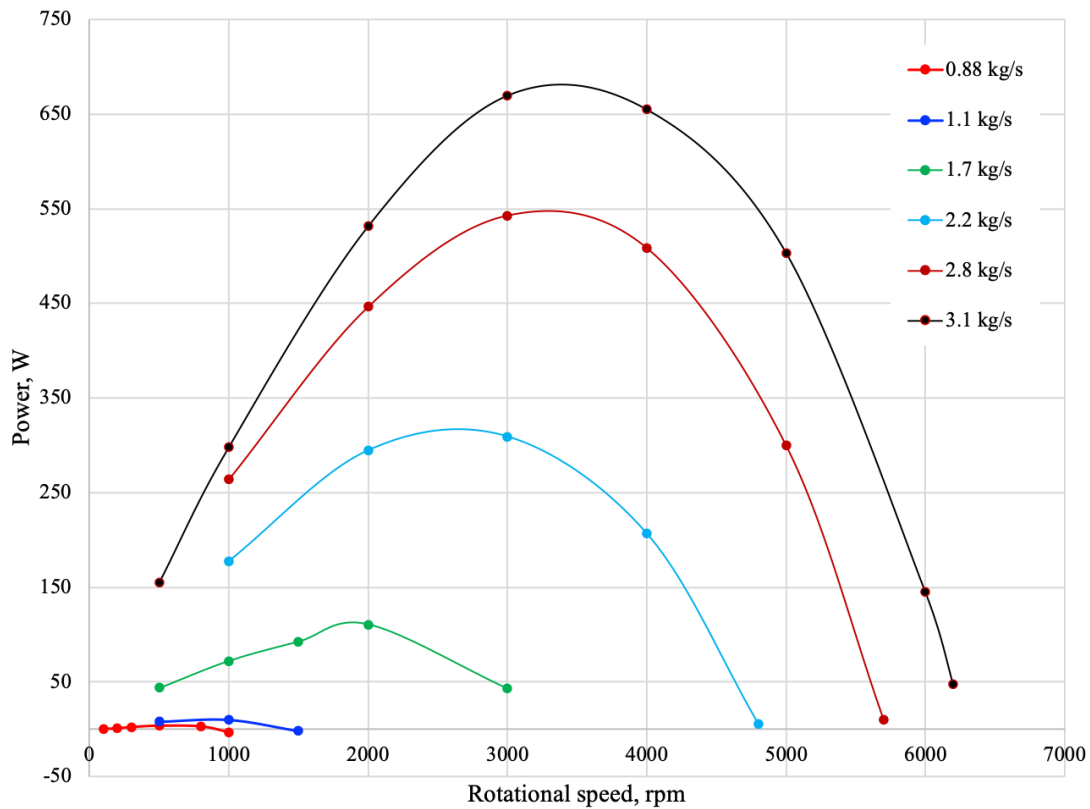
Figure 3.24 Mechanical power versus rotational speed at different mass flow for water
1kW expander

The design performance was still not achieved in the new tests due to possible following reasons:

i. The turbine is tested in far from design condition due to tolerances in the 3D printed nozzle. At higher mass flow, in this case more than double, performance of Tesla rotor drops significantly.

ii. Ventilation losses are found to be very high (discussed in detail in Chapter 4). The power lost due to ventilation is significant, dragging the rotor even at high mass flow due to which design rotational speed was not achieved.

iii. The exhaust losses are not measured in the current tests. A noval radial diffuser technology is used in this turbine (first time for tesla expander) for which performance is not measured and could be one of the reasons of lower performance.

Performance of the turbine will be investigated in future considering above mentioned factors.

Chapter 4　　Losses in Tesla Expanders

The following study aims at the experimental loss characterization in Tesla turbines. The loss mechanisms are studied extensively for conventional turbomachinery, which gives the insights into contribution of each component to the performance of the turbine. By understanding loss mechanisms, one can design and optimize turbine components to improve the performance. In the realm of Tesla turbines, no loss characterization has been carried out systematically on experimental basis. There is little literature on the causes of losses in Tesla turbines. Here, based on real prototypes, the major contributors of losses in Tesla turbines are identified and quantified experimentally. The losses are classified mainly into three parts: stator losses, ventilation losses and leakage losses.
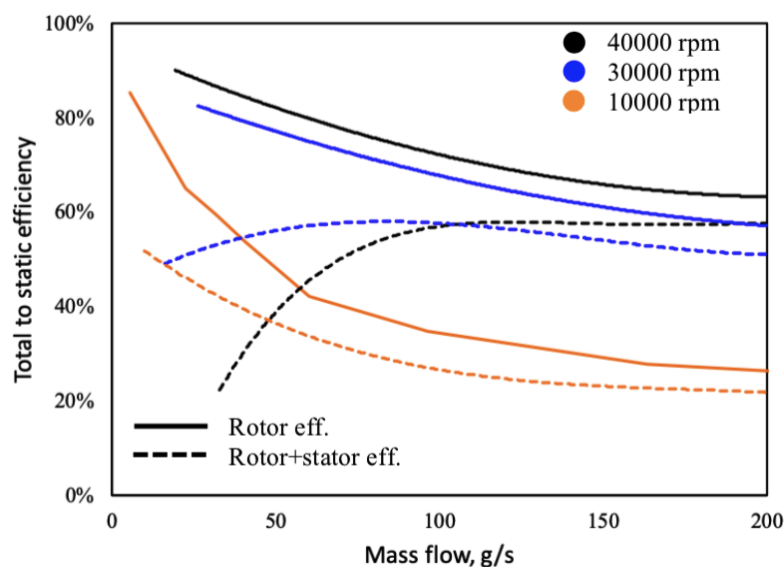
Figure 4.1 Numerical (CFD) performance comparison of rotor(2D) and rotor+stator (3D) efficiencies for air 3kW prototype with respect to mass flow at 10000, 30000 and 40000 rpm

Figure 4.1 shows the total to static efficiency evaluated using CFD for 8 nozzles with air as a working fluid. It shows the comparison between "rotor" and "rotor+stator" efficiencies at different rotational speed. It is evident that the stator losses play a significant role in the performance of the turbine: in this chaptor, it will be demonstrated that rotor-stator interaction losses are the major source of losses for Tesla expanders.

4.1 Loss Components in Bladeless Expander

Losses in bladeless turbomachines can be broadly categorised into three sections: losses in stator, the clearance between rotor and stator, rotor. Table 4.1 shows the complete breakdown of losses in each category, specifying the losses experimentally evaluated in this thesis, with reference to the air 3kW prototype.

The stator losses consist of turbine inlet loss, nozzle losses due to friction and turbulence and rotor-casing peripheral viscous friction loss. In this thesis, experimental characterization is done by measuring static pressure at the nozzle inlet and the "next" nozzle passage (adjacent nozzle in the direction of rotation), which gives the static pressure between rotor and cavity when such "next" nozzle is not operated. This method gives us the combined losses A2, A3 and A4 as shown in Table 4.1.

The lateral cavity between stator and rotor also constitutes an important part of losses in bladeless turbine. It consists of viscous friction losses between end disk-casing passage and fluid leakage flow loss through end clearance.

The rotor of bladeless turbine can be highly efficient if designed properly. The flow angle at the entry of the rotor is crucial for the effective energy transfer between fluid and disks. There are losses in the rotor due to finite disk thickness, friction losses due to radial velocity component, losses due to partial admission at rotor inlet due to discrete nozzles and kinetic energy loss at the exit of the rotor. These losses are not evaluated experimentally due to requirement of complex measurement systems however, they can be estimated by analytical or numerical means.

Table 4.1 Loss Components

		Loss analysis	
	Types of losses	**Experimental**	**Analytical/ Numerical**
A	**STATOR**		
A1	Nozzle entry loss / losses in inlet plenum		X
A2	Viscous friction loss on nozzle	X	
A3	Rotor-casing peripheral viscosu l	X	
A4	losses between stator-rotor cavity	X	
B	**VENTILATION LOSS**		
B1	End wall viscous friction loss	X	X
B2	Leakage loss	X	
C	**ROTOR**		
C1	Rotor entry loss due to finite disk thickness		X
C2	Energy transfer loss between fluid and disk		X
C3	Viscous friction loss due to radial velocity		X
C4	Rotor exit kinetic energy loss		X

Basing on the built prototype, following losses are investigated in this section <u>experimentally</u>:

   i.   Stator losses: these losses include, turbine inlet chamber geometry, friction loss inside nozzle, peripheral viscous friction between stator and rotor and stator-rotor interaction loss

  ii.   Ventilation losses: these losses consist of viscous friction losses between end disks and casing wall

 iii.   Leakage losses: these losses include the power loss due to leakage flow around the disk pack and additional frictional torque on the end disk due to leakage flow.

4.1.1 Losses in the Stator

The rotor of Tesla machines shows high efficiencies, up to 95%, as calculated using analytical methods, where flow at the inlet of the rotor is considered tangential. In other words, to achieve high efficiencies for Tesla machines, the flow at the exit of stator should be nearly tangential

to the rotor. The function of nozzle is to accelerate the flow and direct it almost tangentially to the rotor. The subsonic conditions are favoured generally to avoid any total pressure loss. The conventional convergent nozzle with, subsonic flow generally exhibits higher efficiency. As discussed in the Chapter 1, the stator has been found one of the reasons for the low efficiency of the Tesla turbines. The following requirements for stator make its design particularly challenging:

a. Highly tangential flow requirement at stator exit – the stator/nozzle exit flow should be as tangent to the rotor as possible in order to exists the rotor inlet condition defined in analytical model. The low angle of stator with respect to the rotor periphery makes stator design difficult. At this condition, the fluid jet at the stator exit interacts with the casing generating friction losses. These losses are found to be quite significant as shown in Chapter 2, in the numerical analysis.

b. Expansion and contraction losses – the fluid exiting stator sudden expansion due to clearance between stator and the rotor. This expansion generates losses, which can be predicted using conventional expansion loss models. Also, due to finite thickness of disks, high velocity jet of fluid undergoes contraction losses while entering into disk gap.

4.1.2 Losses in the Rotor

The losses inside the rotor can be divided into two parts: efficient transfer of fluid energy to the disk and losses due to undesired friction (friction due to radial velocity component). These losses can be explained as follows:

a. Transfer of energy between fluid and disk – the energy of the fluid between the disks is transferred to the disk through shear between fluid layers. In order to have effective transfer of this energy without losses, laminar flow between the two disks is necessary. Hasinger [51] has defined the "energy transfer coefficient" , E_t, which depends on flow rate between the disk, gap between disks, viscosity and inner radius of the disk. In order to keep the energy transfer losses at reasonable level E_t must be kept low (~1). This has also been showed by Rice [5] in his analytical solution of flow between corotating disk. The energy transfer coefficient is given by,

$$E_t = \frac{q.d}{v.r_i{}^2} \tag{4.1}$$

Energy transfer coefficient is taken into account while designing the rotor of Tesla turbine or compressor.

b. Friction losses due to radial velocity: the boundary layer between the disks generates shear force i.e. tangential shear force due to tangential velocity (torque on the rotor), and radial shear force, due to radial velocity. The radial shear force is undesired friction which should be minimised for efficient operation of rotor. The pressure loss due to radial frictional force can be calculated using Hagen-Poiseuille equation applied within a radius increment, *dr*

$$d(dp) = \frac{12.\mu.v_r.dr}{\delta^2} \tag{4.2}$$

Bu substituting, $v_r = v_{ro}\,(r_o/r)$, and by integrating we get

$$dp = \frac{12.\mu.v_{ro}.r_o.\ln\frac{r_o}{r_i}}{\delta^2} \tag{4.3}$$

If we normalise by using the Euler work , $\rho*u_o*v_{to}$, we get friction loss coefficient of rotor, $\zeta_{rotor.radial}$,

$$\frac{dp}{\rho \cdot u_o \cdot v_{to}} = \zeta_{rotor.radial} = \frac{12.\mu.v_{ro}.r_o.\ln\frac{r_o}{r_i}}{\delta^2.\rho.u_o v_{to}} \tag{4.4}$$

Defining flow coefficient as the ratio of radial velocity of fluid to the disk speed at disk outer radius, v_{ro}/u_o, and inlet velocity ratio, Ψ (slip), as the ratio of tangential velocity of fluid to the disk speed at disk outer radius, v_{to}/u_o we get:

$$\zeta_{rotor.radial} = \frac{12.\varphi.\ln\frac{r_o}{r_i}}{Re_\delta.\psi} \tag{4.5}$$

where, Re_δ is Reynolds number based on gap between two disks

$$Re_\delta = \frac{\delta.\delta.\omega}{\nu} \qquad (4.6)$$

Hence, the losses in the rotor depends on following main factors:

(i) φ, flow coefficient based on outer disk edge – flow coefficient represents the amount of flow passing through gap between disks. Higher the flow coefficient, higher will be the losses in the rotor due to radial velocity.

(ii) $\ln\frac{r_o}{r_i}$, radius ratio – the friction losses in the rotor is proportional to the logarithmic radius ratio. Higher the radius ratio means higher available area for the friction loss due to radial velocity.

(iii) Re_b, Reynolds number based on gap between disks – Reynolds number based on gap between disks is calculated using fictitious velocity, $\delta.\omega$, with characteristic length of b. It directly represents the laminar condition of the flow, which should be maintained in the rotor for maximum efficiency. It also represents the boundary layer thickness and, consequently, velocity profile between two disks. Breiter and Pohlhausen [42] has shown the similarity parameter, P, $\frac{\delta}{2}\sqrt{\frac{\omega}{\nu}}$,which determines the shape of the radial and tangential flow profiles between the disks. It has been shown that radial profile just deviating from parabolic shape appears to be optimum.

4.1.3 Ventilation and Mechanical Losses

Ventilation losses are viscous friction losses between rotor and casing surfaces. This power loss can be measured by two methods: steady-state (only for low density fluids) and unsteady state. In case of steady-state experiment, rotor is brought to a desired speed of rotation using electric generator/motor. The rotor is allowed to stay at that speed for some time in order to reach the steady state, until no fluctuation in electric power is observed. This motoring power, required to keep the rotor at the steady state, is recorded and is the direct measurement of losses present in the turbine at that configuration. In this way a power loss at each operating speed is

recorded. In case of unsteady-state experiment, rotor is accelerated from initial stationary state to the maximum speed by setting content angular acceleration in the generator. Recorded speed and time are used to derive the angular acceleration of the rotor. The accelerating torque can be found out by multiplying the angular acceleration with the inertia of the rotor of turbine and the generator. The inertia of the turbine rotor is calculated using CAD software and inertia of generator rotor is obtained from motor manufacturer. The total power recorded by the generator is the sum of accelerating power and frictional resistance by the fluid present inside the turbine. The power lost due to frictional resistance of the fluid inside the turbine is evaluated by subtracting the accelerating power from the actual power recorded by the generator.

With reference to the air 3 kW prototype, the unsteady and steady approach of calculating power are analysed by running a turbine without nozzles and inlet air flow. In this case, turbine acts as a compressor where air enters through the inner port of the disks and leaves through periphery of the rotor. All the air inlet ports were opened for this test so that air leaves radially outward through the inlet ports. To obtain unsteady data, rotor is accelerated with constant angular acceleration to reach the desired speed and data is recorded. During steady state, rotor is run at discrete speeds to obtain the power required for the generator to drive the rotor.

Figure 4.2 shows the plot of angular velocity of rotor versus the ventilation power loss. It shows the comparison of two unsteady runs with one steady run. We can see that data points for all three test runs are well consistent. This test confirms that both approaches could be used to analyse the losses in the turbine for fluids at low density such as air. At higher fluid densities, inertia of the rotating fluids must be added in the unsteady state loss analysis.

A run-down experiment is performed by switching off the supply of compressed air when turbine is running at desired speed. Due to frictional forces and resistance from the ventilation fluid, and bearing friction, rotor decelerates. The complete deceleration of the rotor in the form of rotor speed and time is recorded. The resistive torque is then calculated by numerically differentiating angular velocity to obtain angular acceleration and multiplying it with moment of inertia of rotor. From the experimental curve of angular velocity and time, power loss vs speed is plotted using Eq. (4.7),

$$P_{loss} = -\tau_{res}\omega = -I\dot{\omega}\omega \tag{4.7}$$

Fitted curve shown in Figure 4.3 is used to calculate coefficients needed to estimate Power loss.

Power loss can be expressed by

$$P_{loss} = P_{loss\_ref} \left(\frac{N}{N_{ref}}\right)^a \tag{4.8}$$

where, P_{loss} is the total power lost due to friction and ventilation, P_{loss_ref} is the power lost at the reference speed N_{ref}, rpm, a is an exponent.
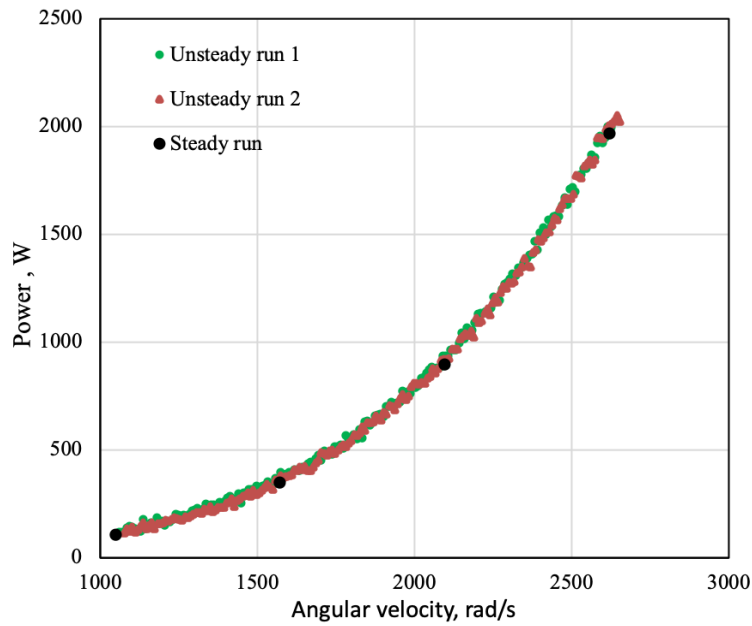
Figure 4.2 Ventilation power loss versus angular velocity of rotor for steady and unsteady cases for air 3 kW prototype

4.1.4 Leakage Losses

Tesla turbine, similar to bladed radial turbines has leakage mass flow around the end disk tip to the outlet. In radial turbines leakages are mostly controlled by labyrinth seals. In case of

Tesla turbines, a portion of the nozzle flow may directly enter the end gaps and leave the outlet of the turbine without contributing to the power. If the end gap clearances are not controlled, then there is possibility of high leakage mass flow.

4.1.5 Turbine Inlet and Exhaust Losses

Exhaust losses can be divided into two main parts: (i) the losses on the inner edge of the disks and (ii) the losses of the actual exhaust duct connecting to external environment. Both losses can be considered as minor losses (low density fluids and low velocity), which can generally be evaluated as:

$$\Delta p = \beta \rho \frac{v^2}{2} \tag{4.9}$$

These losses are therefore proportional to the square of the velocity, either relative (inside the rotor) or absolute (inside the static exhaust duct), which depends on the flow rate, the density and the passage section. The losses at the exhaust can be regarded as proportional to the square of the ratio between the flow rate and density. In the exhaust line, both the rotating and stationary section, velocity might not be negligible due to the tangential speed which depends onto the rotor disk inner diameter.

4.2 Characterisation of Losses

4.2.1 Losses in air 100W Expander

For the air 100 W expander, ventilation losses are experimentally evaluated, and other losses are calculated numerically to understand the overall performance of the expander as outlined in Table 4.2

Table 4.2 Loss components analysed for air 100 W expander

		Loss analysis	
	Types of losses	**Experimental**	**Analytical/ Numerical**
A	**STATOR**		
A1	Nozzle entry loss / losses in inlet plenum		X
A2	Viscous friction loss on nozzle walls		X
A3	Rotor-casing peripheral viscosu loss		X
A4	losses between stator-rotor cavity		
B	**VENTILATION LOSS**		
B1	End wall viscous friction loss	X	X
B2	Leakage loss		X
C	**ROTOR**		
C1	Rotor entry loss due to finite disk thickness		X
C2	Energy transfer loss between fluid and disk		X
C3	Viscous friction loss due to radial velocity		X
C4	Rotor exit kinetic energy loss		X

Figure 4.3 shows the run-down test performed using methodology given in section 4.1.3. The experimental data is fitted in an empirical correlation using Eq. (4.8).

Eq. (4.8) becomes the following empirical correlation.

$$P_{loss} = 34.77 \left(\frac{N}{40000}\right)^{1.845} \tag{4.10}$$

The exponent of Eq. (4.10) is close to 2. There are two possible explanations for this: (i) overall losses are equally distributed between roll bearings (expected to have a linear power loss with speed – obtained from manufacturer data) and ventilation turbulent losses (expected to have a cubic trend); (ii) losses are dominated by laminar losses. It is believed that the second hypothesis is the most likely, as bearing losses should be small compared to the measured total values, and friction losses with casing occur in very thin gaps, where laminar regime can develop. Verification of this hypothesis is done in the next section with air 3 kW and water 1 kW expander prototype.
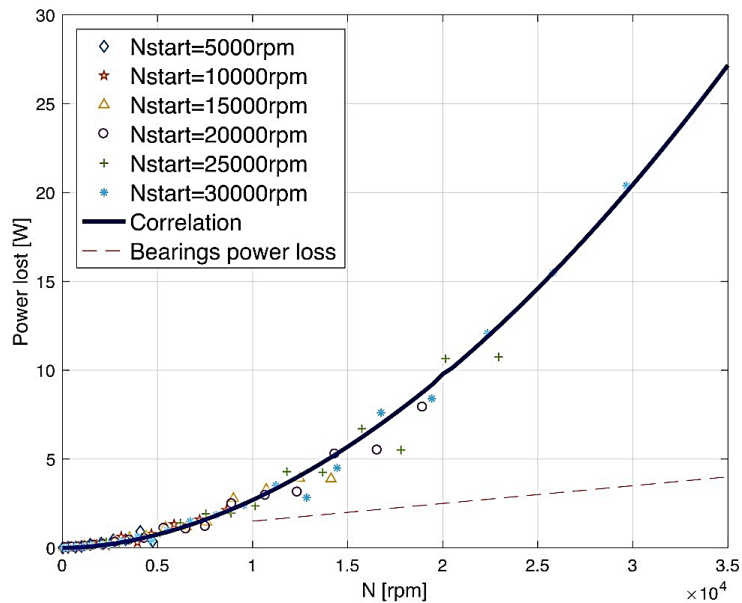
Figure 4.3 Ventilation and bearing power loss (obtained from manufacturer datasheet) as a function of rotor speed, air 100W prototype

In this specific case, the four major sources of losses in turbine are: leakages losses, nozzle loss, rotor losses and ventilation losses (for high rotational speed). The analytical solution [52][53][54] for the Tesla rotor is used along with losses correlations to plot the impact of losses on the overall performance of the expander[45]. The pie chart of Figure 4.4 illustrates the percentage of each loss on the ideal isentropic power for one configuration[44]. This condition, at which the pie chart is plotted, has been chosen since it is one of the most efficient case for which the model fits properly[44]. stator losses, exhaust loss and rotor losses are evaluated analytically and numerically while ventilation loss and leakage loss are measured experimentally. In this expander, stator and leakage losses found to be dominating, contributed more than 50% of the total loss. Since the fraction of leakage is 46.7%, it could be expected that the power lost due to leakage is almost half of the ideal expansion power, but the leaking mass flow only bypasses the rotor and contributes, despites partially, the work exchange.
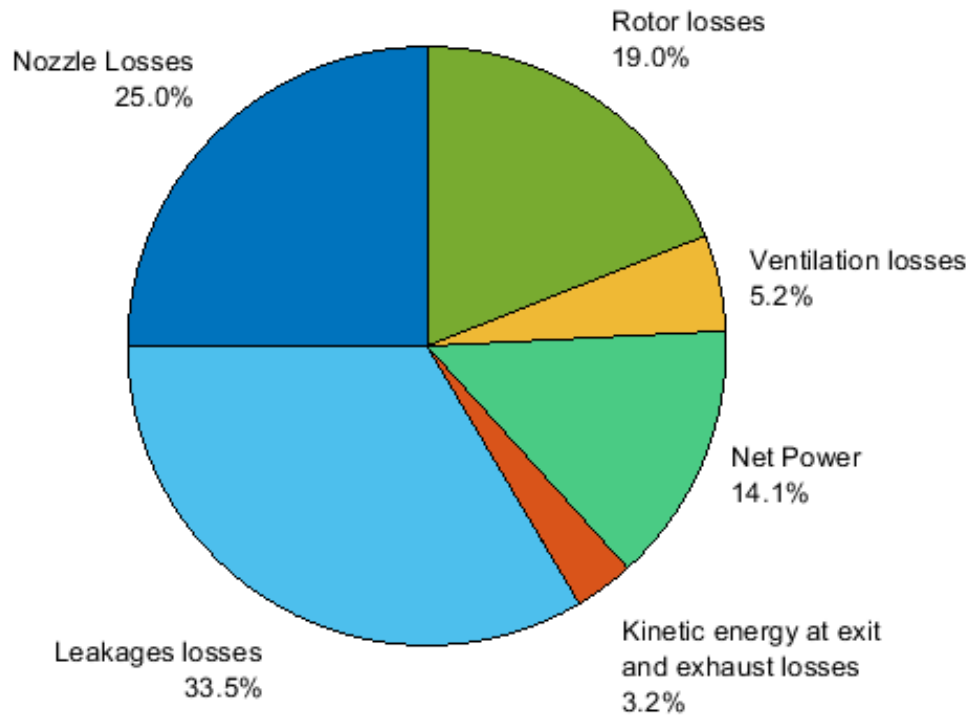
Figure 4.4 Losses contribution for N=30000rpm, b=0.3mm and d_i=25mm, $\dot{m}$=5.1g/s, air 100W prototype

Ventilation losses are one of the main sources of loss, especially at high rotational speeds and low mass flows, Figure 4.5 shows a comparison between the computed efficiency and the efficiency computed without the ventilation losses. It shows that ventilation losses impact significantly both in absolute values and trends of efficiencies: in particular, if ventilation losses are not considered (or reduced in an improved design), the Tesla turbine seems to best perform at the lowest mass flow rates. We can see very interesting phenomena in Figure 4.5: efficiency curves with ventilation losses (real) shows peaks of curve on the high mass flow side of the graph. While the efficiency curves without ventilation loss show peaks towards low mass flow side of the graph. This means that ventilation losses have significant role to play at low mass flow where we see drastic change in the efficiency. As mass flow increases, both the curves, with and without ventilation losses, converges. The negative efficiencies are produced by the model since the ventilation losses are probably overestimated at low mass flow rate. Firstly, the model computes the power that is transferred from the flow to the rotor, that has

always positive values, then to obtain the net power, power loss due to ventilation is subtracted (evaluated according to Eq. (4.10).
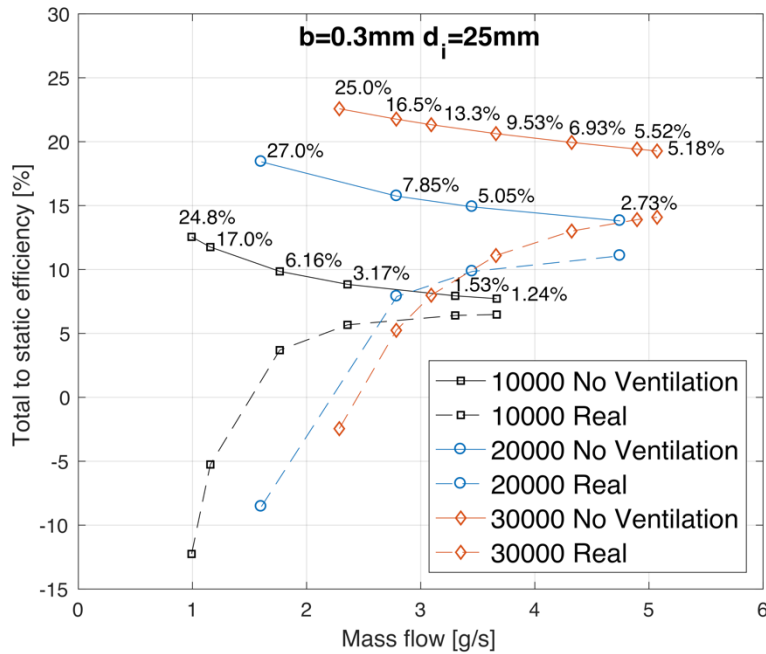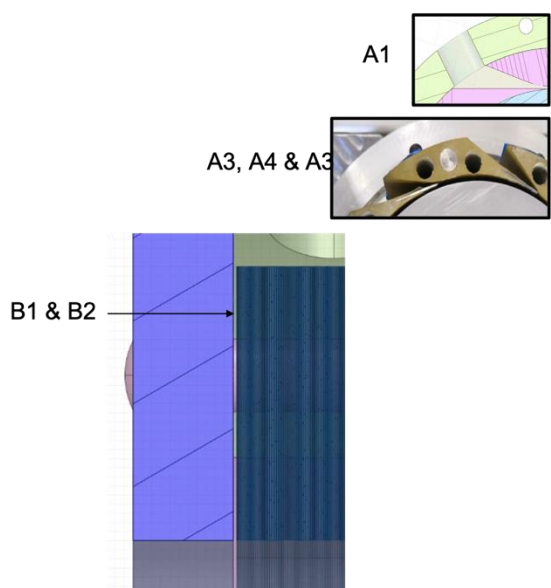
Figure 4.5 Trends of efficiency with and without the ventilation losses (labels show the percentage contribution of ventilation losses to isentropic power)

4.2.2 Losses in air 3 kW Expander

In the previous chapter of experimental test campaign, a complete performance test is carried out on 3 kW turbine with high speed generator with air as a working fluid. The total to static efficiency of 36.5% is obtained which is the best ever achieved efficiency for Tesla turbine prototypes fed by air. In the literature, efficiencies of around 25% are common for these turbines.

Following section presents experimental estimation for A and B losses of Table 4.3. These losses are then discussed with respect to the impact on overall turbine performance.

Table 4.3 Loss components for 3 kW air expander

		Types of losses	Loss analysis	
			Experimental	Analytical/ Numerical
A		**STATOR**		
	A1	Nozzle entry loss / losses in inlet plenum		X
	A2	Viscous friction loss on nozzle	X	
	A3	Rotor-casing peripheral viscosu l	X	
	A4	losses between stator-rotor cavity	X	
B		**VENTILATION LOSS**		
	B1	End wall viscous friction loss	X	X
	B2	Leakage loss	X	
C		**ROTOR**		
	C1	Rotor entry loss due to finite disk thickness		X
	C2	Energy transfer loss between fluid and disk		X
	C3	Viscous friction loss due to radial velocity		X
	C4	Rotor exit kinetic energy loss		X

Stator and stator-rotor clearance loss evaluation

Stator constitute the major part of the losses in the Tesla turbines. Unlike in conventional turbines, Tesla turbine needs to have highly tangential flow at the inlet of the rotor to achieve high efficiency. This makes the stator very swirled, long and inefficient. The turbine used in this experiment has the nozzle designed to have exit flow angle of ~2 degree, mass averaged. Guha and Smiley [8] have studied the effect of inlet and nozzle in Tesla turbines experimentally. They reduced the losses in the inlet and nozzle system from 13-24 percent to 1 percent with the improved design. Hence, it is very important to analyse the performance of the stator experimentally in order to better understand its contribution to the overall performance of the turbine. The stator losses are divided into three parts: (i)nozzle entry loss, (ii)nozzle loss and (iii)rotor-casing peripheral viscous friction losses.

The compressed air is delivered to the turbine through a hose of diameter 12.7 mm. The pressure sensor is attached to this hose which measures the static pressure. This hose is then connected to the circular section on the casing of diameter 15 mm, as shown by #1 in Figure 4.6 (right). This hole in the casing aligns with the inlet section of the nozzle insert. Air then passes through the nozzle (shown by #2 in Figure 4.6 (left)), converting pressure energy into

kinetic energy. This high velocity jet of air enters the rotor tangentially. The static pressure at the next nozzle is also measured, which is shown by #3 in Figure 4.6 (left). The test is carried out with different inlet pressure and rotational speeds.

There is total pressure drop due to losses in the inlet of the turbine. Firstly, losses due to abrupt enlargement from 12.7 m to 15 mm section and then the losses due to change in the flow direction from circular section in the casing to inlet of nozzle insert. The losses due to abrupt enlargement and change in flow direction are calculated using following equation[55]:

$$dp_{in} = \frac{k.\rho v_i^2.}{2} \tag{4.11}$$

$$k = \left(1 - \left(\frac{A_i}{A_o}\right)^2\right)^2 \tag{4.12}$$

where, subscripts *i* and *o* are inlet and exit section of the flow.
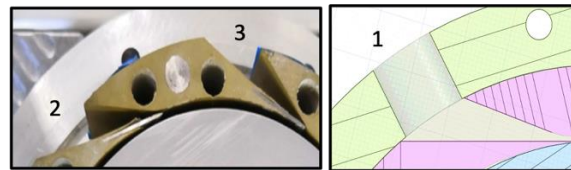
Figure 4.6 Nozzle inserts (left) and radial
feeding hole (right)

The calculated pressure loss based on Eq. (4.11) is 3% of inlet total pressure. These losses can be reduced significantly by improving the inlet system.

The nozzle used in this turbine is convergent-only and the inlet pressure at which choking happens is 2.65 barg at one nozzle configuration. At this pressure, flow is sonic at stator throat and there is no increase in non-dimensional mass flow (as discussed in Figure 3.11 in Chapter 3). The further increase in inlet pressure might create supersonic condition due to enlargement of the area just after the throat due to stator-rotor cavity profile. Supersonic flow with expansion waves is expected to occur for further pressure drops. This phenomenon needs further investigation and is out of scope of the present study.

In order to characterize the losses in the nozzle, static pressure at the nozzle exit is measured as shown in Figure 4.7. It was difficult to measure the static pressure at the nozzle exit; hence probe was put at the next unused nozzle. In this case, nozzle losses are overestimated as these losses also involves losses due to friction and interaction between casing and nozzle. One of the findings in our previous research on a 100 W Tesla expander prototype was a major source of loss, which occurs in the nozzle and nozzle-rotor interaction. Stator and stator-rotor interaction, hence, very important aspect in the design of efficient Tesla turbine.
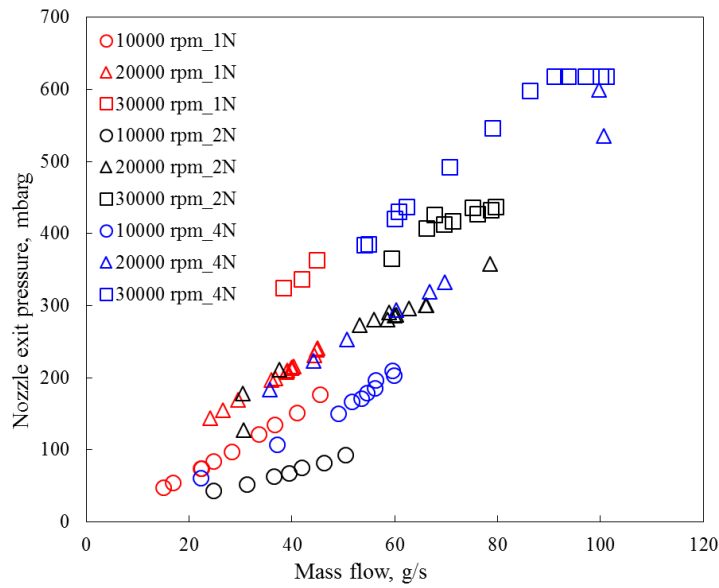
Figure 4.7 Variation of nozzle exit pressure (static, gauge) vs nozzle inlet pressure (total, absolute) for different rotational speeds for 1, 2 and 4 nozzles configuration

In order to evaluate the losses in the nozzle and viscous friction on the casing, total pressure at next nozzle (#3 in Figure 4.6 (left)) is calculated using compressible fluid relations [50].

$$P_{ex.tot} = p_{ex.st} \cdot \left[\frac{1}{2} + \sqrt{ \frac{1}{4} + \left(\frac{(k-1)}{2k} \right) \cdot \left(\frac{\dot{m}}{A_{ex.nozz} \cdot p_{ex.st}} \right)^2 \cdot \left(\frac{R.T_{tot}}{g} \right) } \right]^{\frac{k}{(k-1)}} \tag{4.13}$$

All the quantities required to calculate the total pressure at the exit of the nozzle are known. An approximate estimation of nozzle efficiency can be carried out using total pressure at inlet

and exit of the nozzle. This parameter mainly represents the losses in the expansion process due to nozzle abrupt enlargement into the rotating disk casing.
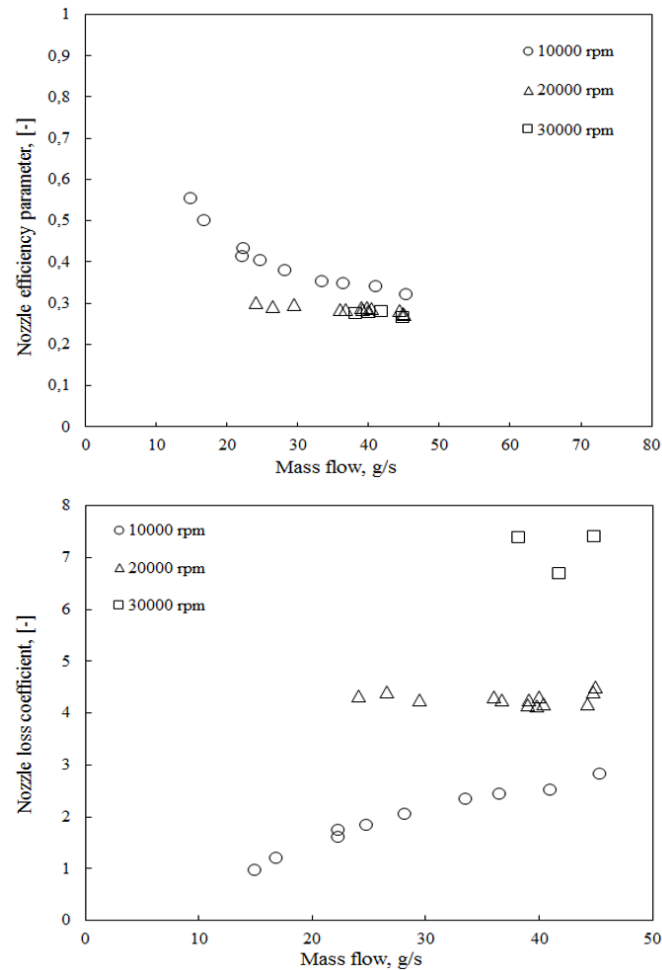
Figure 4.8 Variation of nozzle efficiency parameter and nozzle loss coefficient with respect to mass flow

Nozzle efficiency parameter is calculated by:

$$\eta_{nozz} = \frac{p_{ex.tot}}{p_{in.tot}} \tag{4.14}$$

Another loss coefficient is defined in terms of static pressure at the exit. This loss coefficient is used to understand losses due to friction in the nozzle and stator-rotor interaction. Nozzle loss coefficient is calculated as follows [50]

$$Y_N = \frac{\left(\dfrac{p_{in.tot}}{p_{ex.tot}}\right) - 1}{1 - \left(\dfrac{p_{ex.st}}{p_{ex.tot}}\right)} \tag{4.15}$$

Figure 4.8 shows the nozzle loss coefficient and nozzle efficiency parameter with respect to mass flow. Nozzle loss coefficient is increasing with mass flow and then it becomes constant and shows the dependence on the rotor speed. Higher the rotor speed, higher the nozzle loss coefficient. At higher mass flow rate, nozzle velocity is higher, which increases the wall friction loss at the nozzle and casing. Also, with increase in rotor speed the viscous friction between rotor tip and the casing increases leading to higher nozzle loss coefficient. The increase in nozzle loss coefficient is significant in case of higher rotational speed.
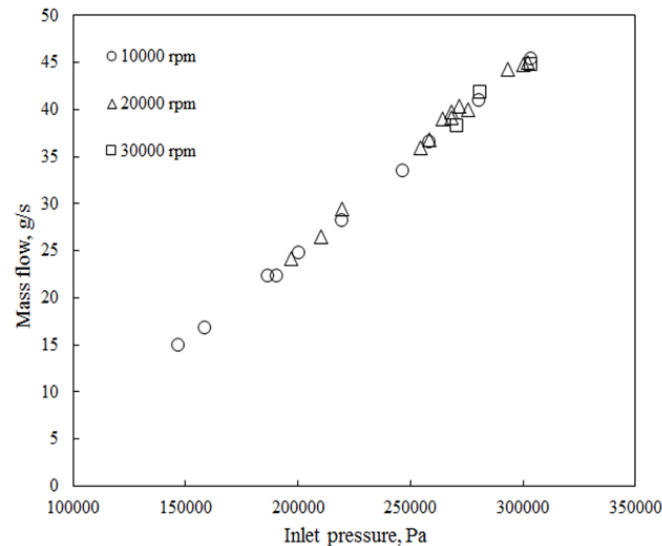
Figure 4.9 Mass flow versus nozzle inlet pressure at different rotational speeds

The clearance between rotor and stator, i.e. the peripherical cavity in between the disk tip and the stationary stator profiles/casing, plays an important role in controlling these losses as a smaller clearance will lead to more viscous friction losses at higher rotor speed; Guha et al [25] numerically demonstrated that an optimum exists for such clearance, as a compromise between viscous losses and fluid turbulence losses in such cavity. Figure 4.8 shows the nozzle efficiency parameter which is the measure of expansion efficiency of the nozzle. We see that expansion efficiency of the nozzle is higher at lower inlet pressure or lower mass flow rate. When the nozzle is choked, at the inlet pressure of 2.65 barg or mass flow rate of 40 g/s, nozzle efficiency

tends to become flat. This may be due to the choking of the nozzle and efficiency remains stable. We observe that overall efficiency of the nozzle is very low at higher mass flow conditions. This implies that stator and stator-rotor interaction losses play a major role in driving the performance of the turbine.

End wall losses – Ventilation loss evaluation

In this section, losses between the two rotating end disks, at the extremes of the rotor, and casing are analysed. Figure 4.10 shows the experimental test rig to perform loss characterisation. To perform this test, we needed to close the inlet and outlet openings of disk pack (rotor), to avoid any pumping effect. One of the easiest ways to do is to close it with the help of masking tape as shown in Figure 4.10 (c). The problem with the masking tape is that at higher rotational speed of the rotor (greater than 20000 rpm), the masking gets removed. This is the reason why the data for the power loss are presented till 20000 rpm. Closing inlet and outlet opening of rotor ensures that there is not flow inside rotor from any direction ensuring no participation of rotor for producing or consuming power. The air flow is allowed only between end disks and casing. Also, all the nozzle inserts are removed, and inlet ports of the turbine are opened to atmosphere. When the turbine is driven using motor, it draws the air from the inner opening of casing, passing through end disks and casing clearance, and exiting through inlet ports to the atmosphere. In this mode turbine acts as a compressor having only two end gaps. In this way ventilation losses between end disks and casing can be evaluated.

This test is run in two configurations:

1) turbine with one casing wall as shown in Figure 4.10 (c) #7 (the other casing plate is removed)

2) turbine with both the casing plates.

The first configuration with one casing wall will give the losses between one end disk and casing gap along with mechanical losses due to bearings. The second configuration with both the casing plates will give the losses for both end gaps along with bearing losses. If we subtract the losses from configuration 2 to configuration 1, we get the ventilation losses on one side of the end disk (opposite to motor side).
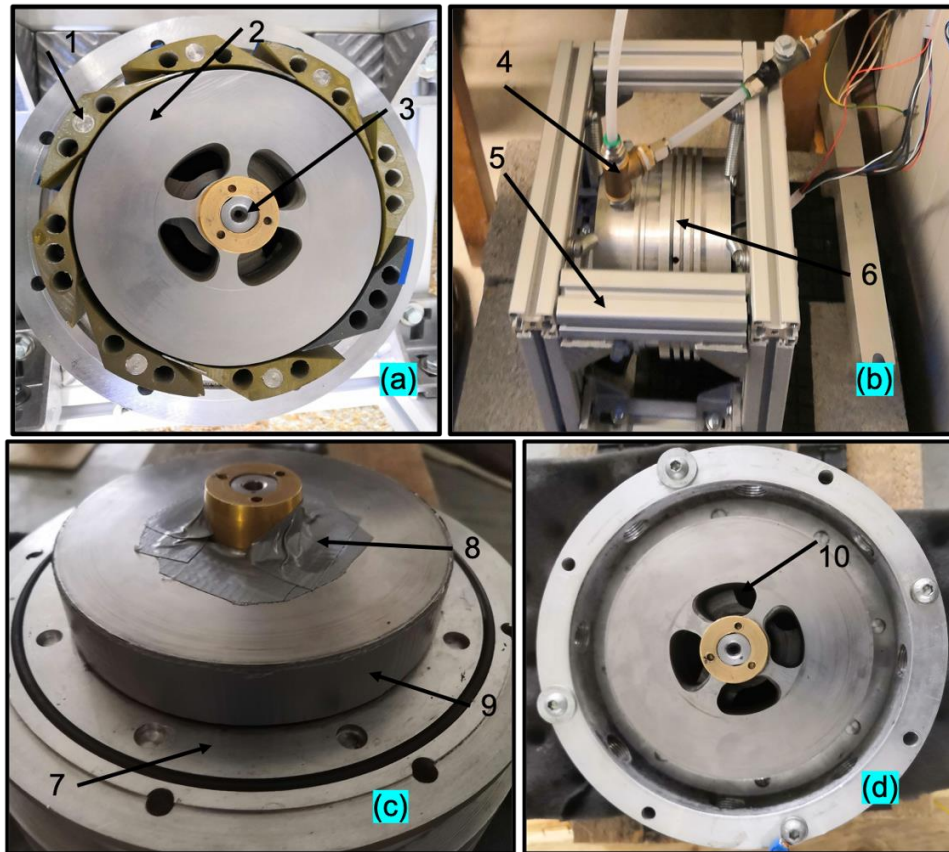
Figure 4.10 Experimental test rig for loss characterization: (a) turbine with nozzles: 1) nozzle; 2) disks; 3) shaft; (b) turbine housing: 4) pressure probe; 5) support frame; 6) turbine and generator housing; (c) rotor with closed inlets outlets: 7) end casing wall 8) masking tape to close outlet; 9) masking tape to close rotor inlet; (d) turbine without nozzles: 10) rotor exit

Figure 4.11 shows the end wall losses measured for the two configurations mentioned above. Configuration 2 represents the total end wall loss along with losses in bearings. The end wall loss on one side has been calculated by subtracting the config.1 from config.2. We observe that end wall losses together with bearing losses are significant if we compare with overall power of the turbine. The losses are following a quadratic trend with rotational speed. It is difficult to distinguish the bearing losses and end wall losses on both sides separately as the clearance on both end wall gaps are kept different due to assembly constraints. During test, it is observed that end disks were deformed which significantly reduces the end wall gap during operation and might have rubbed against the casing. This metal to metal friction may have also caused

such high friction power losses. This behaviour has been observed during experiment in the form of end disk tip cracks. This analysis gives us insight into the share of these losses into overall performance of the turbine. It is crucial to ensure the desired axial clearance between end disks and casing to minimise these losses.
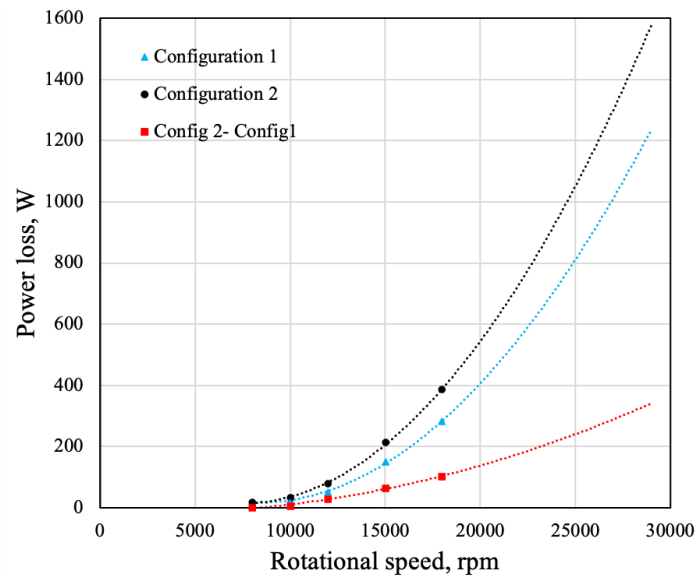
Figure 4.11 End wall loss: power loss in configuration 1, configuration 2 and relative difference versus rotor speed

Following polynomial regressions are used to predict the data at higher rotational speeds as shown in Figure 4.11:

For configuration 1:

$$y = 3 \cdot 10^{-6}x^2 - 0.0473 \cdot x + 212.84 \tag{4.16}$$

$R^2 = 0.9992$

For configuration 2:

$$y = 3 \cdot 10^{-6}x^2 - 0.0503 \cdot x + 201.82 \tag{4.17}$$

$R^2 = 0.9991$

For config.2- config.1:

$$y = 3 \cdot 10^{-6}x^2 - 0.0503 \cdot x + 201.82 \tag{4.18}$$

$R^2 = 0.9936$

where, y is power loss in Watts and x is rotational speeds in rpm.

Leakage losses

In the current turbine, no sealing system is used. Due to assembly constraints we kept end gap clearance of 0.2 mm and 0.5 mm, on motor side and free opening side, respectively. There is trade-off between lower clearance required for leakage and higher clearance required for ventilation losses.

Hoya and Guha [7] have measured the pressure between the end wall gap and the nozzle exit pressure. They found that the pressure being in the same range. This means that part of the jet of the nozzle were passing through the end gaps leading to leakage flow. However, they have not established the correlation between leakage flow and nozzle exit pressure. Also, the effect of this mass flow in the end gap on the power loss due to ventilation is not investigated. In order to characterise both these phenomena, an experiment scheme is realised to provide deeper insight into these losses.

In this test, the turbine is operated in normal mode with rotor closed using masking tape so that air does not pass through the rotor, but it passes through the end gaps. Mass flow and static pressure at the nozzle exit is measured. As the air is only passing through the end gaps, this represents the leakage flow corresponding to nozzle exit pressure. While measuring end disk gap leakage flow rates, the flow path inside rotor is blocked by masking tape to make sure that flow after coming from nozzle passes through end disk gaps. In this turbine, length of the nozzle is same as length of the disk pack. The characteristics of the end gap leakages depends on the pressure difference between nozzle exit and the turbine exhaust. The turbine exhaust being same i.e. atmospheric, the leakage flow is measured for different nozzle exit pressure. However, the nozzle inlet pressure in this case can be different than the actual turbine running case. In order to eliminate the effect of skin friction of the masking tape around the turbine disk

120

pack, all other nozzle inserts are removed while doing the experiment except two to feed air. Absence of nozzle inserts creates big gap between masking tape and casing wall. Hence, the skin friction effects can be fairly assumed negligible. The readings are recorded at different rotational speeds.

Figure 4.12 shows the leakage flow through turbine with respect to nozzle exit pressure at different rotational speeds. We see that leakage flow is a weak function of rotational speed. The leakage flow follows approximately a linear trend with nozzle exit pressure. It is driven by the pressure difference between nozzle exit pressure and turbine outlet pressure without significant influence of rotor speed. It can be seen that the overall amount of leakage flow is significant, if compared to the design flow of the machine (Table 3.6).
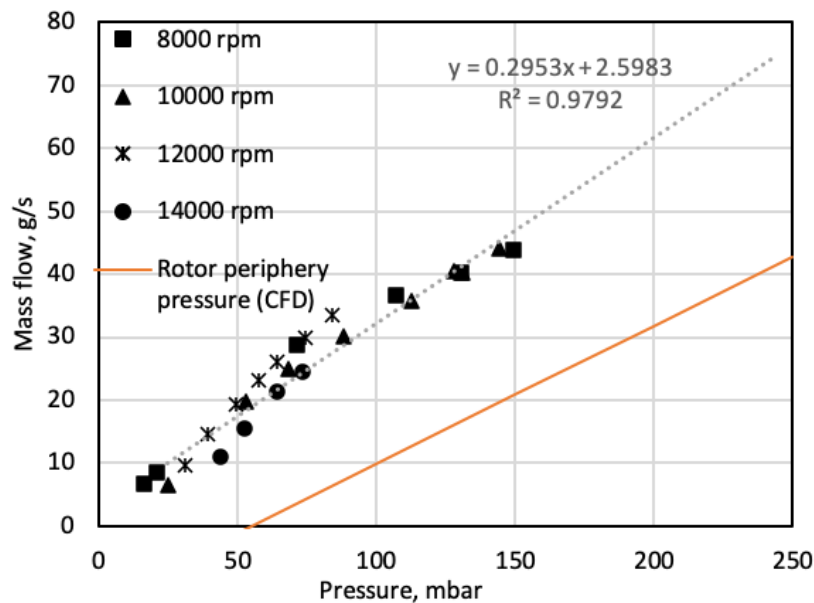
Figure 4.12 Leakage losses: leakage flow with respect to (i) experimental static pressure at inactive nozzle at different rotational speeds, (ii) experimental leakage flow correlated with average rotor peripheral pressure using CFD
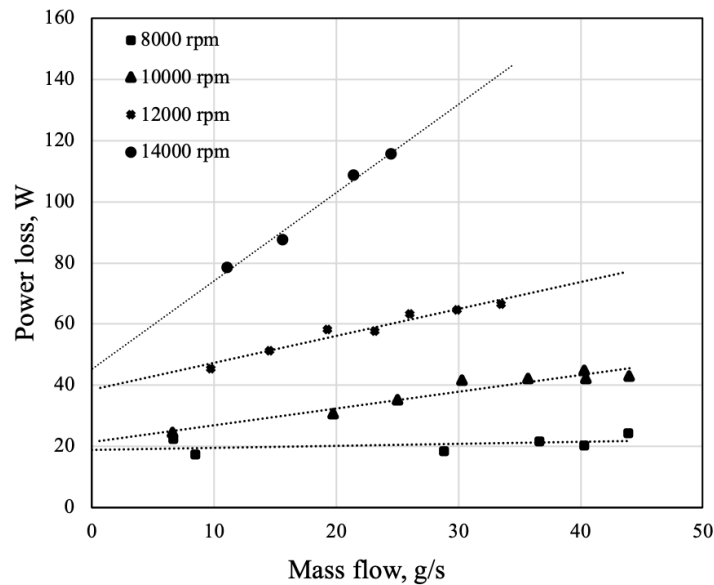
Figure 4.13 Leakage losses: power loss due to leakage flow at different rotational speeds

Figure 4.13 shows the effect of leakage flow on the ventilation power loss in the end gaps. Surprisingly, there is a distinct influence of leakage mass flow on motoring power, i.e. end-disk ventilation loss (see paragraph 4.2.2): therefore, previous analysis on end-wall ventilation loss, being performed with zero leakage might have underestimated the actual power losses than leakage is present. Previous analysis (Figure 4.11) is consistent with zero-leakage(y-axis) values of Figure 4.13. We observe that at low rotational speed the effect of leakage flow is negligible. However, as the rotational speed increases, the power loss increases almost linearly. This behaviour can be explained as follows. The flow phenomenon between stationary and rotating disk is very complex in nature. It involves both laminar and turbulent flow regimes. The leakage flow further complicates the flow structure for example by inducing additional angular momentum. The clearance between end disks and casing also significantly affects the way losses occur. For small clearances, a strong viscous affected shear flow develops while in case of higher clearances a flow with two boundary layers with a core region establishes. Daily and Nece [56] examine the flow between stationary and rotating disk in an enclosed cavity both analytically and experimentally. From the experimental data they were able to distinguish between four different flow regimes that can occur inside the gap based on the circumferential Reynolds number ($Re_\phi = \Omega\, r_o^2/\nu$) and gap ratio ($G = b/r_o$) as shown in Figure 4.14. In the

present turbine case, we have gap ratio G = 0.003 and 0.008, and Re_ϕ < 750000 (maximum rotational speed of 30000 rpm).
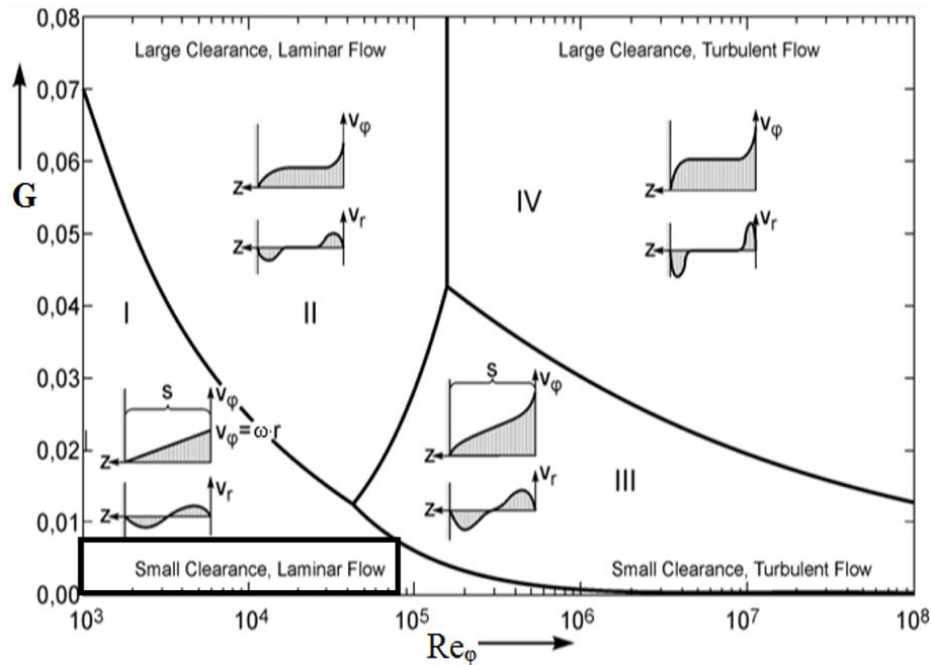
Figure 4.14 Flow regimes between stationary and rotating disks [56] . Black rectangular box showing turbine end gap operating zone

We can see from Figure 4.14 that during the entire operation of the turbine, end gaps are subject to flow regime I, which is small clearance-laminar flow. Daile and Nece[56] showed experimentally that the frictional torque is higher in regime I due to strong viscous shear force. Very few researches are available on the flow in rotor-stator system with superimposed leakage flow, which is the actual scenario in the turbomachine applications.

As the incoming leakage flow is turbulent in nature, the flow between stator-rotor disks gets influenced and transition from laminar may occur. This transition of flow switched the flow regime from I to III (small clearance -turbulent flow). Hu et al [57] have experimentally and theoretically shown the dependency of leakage flow through end disks on the torque of the rotor. The flow regime investigated in the analysis is III. The friction rotor torque increased linearly with respect to leakage flow.

From the above discussion we realise that the leakage flow has strong influence on the ventilation at the casing-disk end gaps. The clearance between end disks and casing needs to (end-wall ventilation) optimized by considering both leakage flow and power loss due to viscous friction.

Impact of losses on overall turbine performance

In the previous sections we have seen the experimental loss characterisation of entire turbine. In this section, a quantitative division of losses are shown in terms of total to static efficiency. Operating curve of the turbine at maximum total to static efficiency point is selected, which corresponds to 2-nozzles configuration. The operating speed of the curve is 10000 rpm. The maximum total to static efficiency is $36.5\pm1.8\%$.
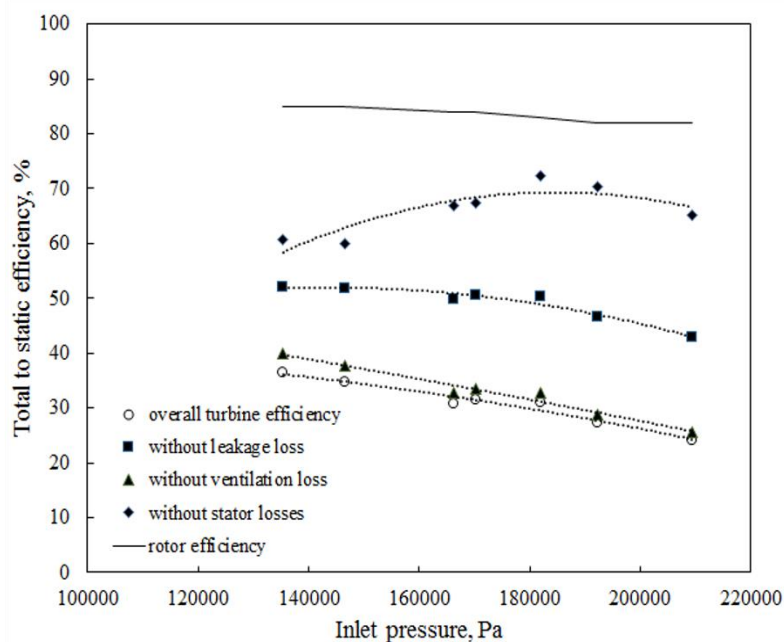
Figure 4.15 Total to static efficiency versus turbine inlet pressure with different losses (all the curves are evaluated experimentally except rotor efficiency which is obtained using CFD)

Figure 4.15 shows the total to static efficiency of the turbine with and without losses. Following curves are plotted:

a. Overall turbine efficiency: this curve shows the turbine efficiency including all the losses. It shows the maximum efficiency at low inlet pressure (low flow) and decreases as flow increases.

b. Without leakage and ventilation losses: this curve represents the efficiency of the turbine without leakage mass flow and ventilation losses. We observe that the effect of leakage flow is linear with the inlet pressure. Without leakage and ventilation losses the efficiency of the turbine increases by more than 15 points. The impact on turbine performance is significant. It is necessary to optimize the end gap clearance and introduce a sealing mechanism to control the leakage flow (which increases the ventilation losses, as previously demonstrated)

c. Without stator losses: this curve represents the efficiency of the turbine without nozzle inlet loss, nozzle loss and losses in the peripheral cavity between rotor and stator. We observe that this type of loss is the most significant for the overall performance of the turbine. It shows that improvement in the efficiency as high as 40 point can be achieved if this loss is reduced. We have previously shown (Figure 4.4) using 1-D tool loss analysis that the stator losses and leakage losses being dominant factor in the Tesla turbine performance.

d. Without ventilation losses (and bearing losses): this curve shows the efficiency of the turbine without ventilation losses due to end gaps. We see that the ventilation losses are not very high as this curve is for 10000 rpm (low rotational speed). However, we have seen in previous sections that ventilation losses can be significant if the operating condition of the turbine is at higher rotational speed.

f. rotor efficiency: This curve shows the rotor-only efficiency evaluated numerically. It shows that the rotor efficiency is very high (> 80%). The overall performance of the turbine is very low (< 40%) compared to rotor-only expected performance. This indicates that, improved stator system is required to match the performance of the Tesla turbines with the conventional bladed turbines.

4.2.3 Losses in Water 1 kW Turbine

As per preliminary experimental tests (described in Section 3.3), the performance of water expander was not as expected by numerical results. In order to understand the cause, as the first

intuition for the major source of losses to be ventilation due to higher available surface of rotating parts with respect to casing, run down experiment is performed. The run-down experiment is performed both with air (i.e. empty turbine) and water.
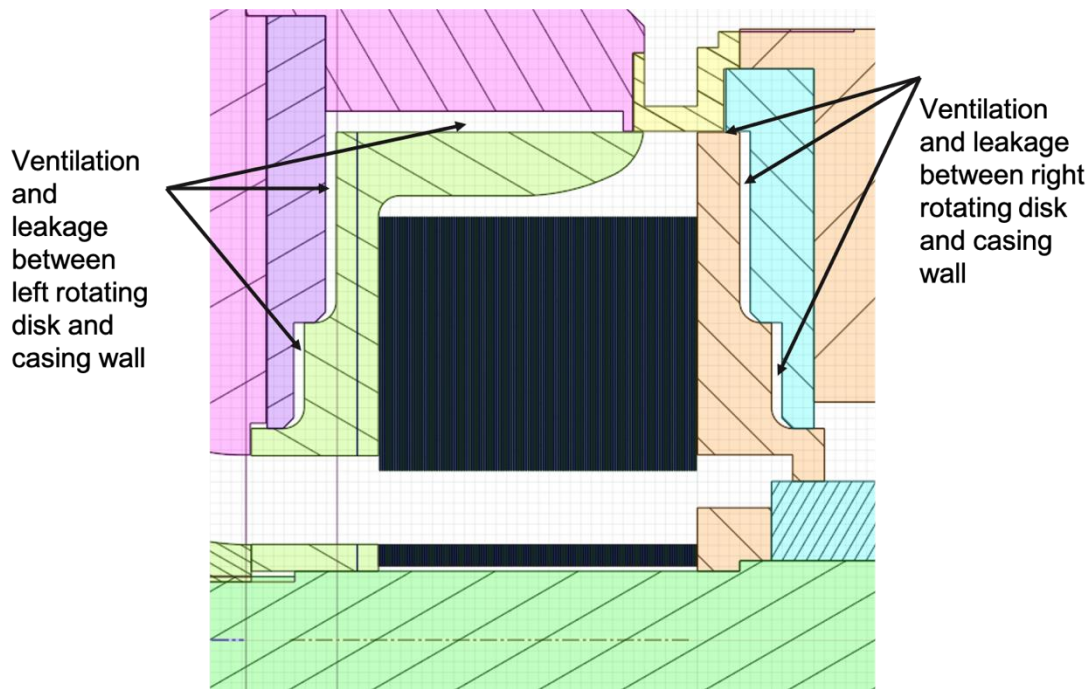
Figure 4.16 ventilation loss for water 1 kW turbine

Figure 4.17 shows the run-down test performed with both air and water. The run-down test is performed in similar way as done for previous air expanders. Run-down test with air on the current expander gives clear understanding of losses due to mechanical sealing and the bearings. This is because, as the gap between rotating surface and casing is ~1 mm, we expect ventilation power loss would be negligible in this case. Run down is started with rotational speed of 5500 rpm and when the water supply is cut off, the rotor comes to rest due to viscous resistances in the stator-rotor cavity. In case of air, the rotor is brought to 5500 rpm using generator because there are no inlet air flow arrangements in the water test rig.
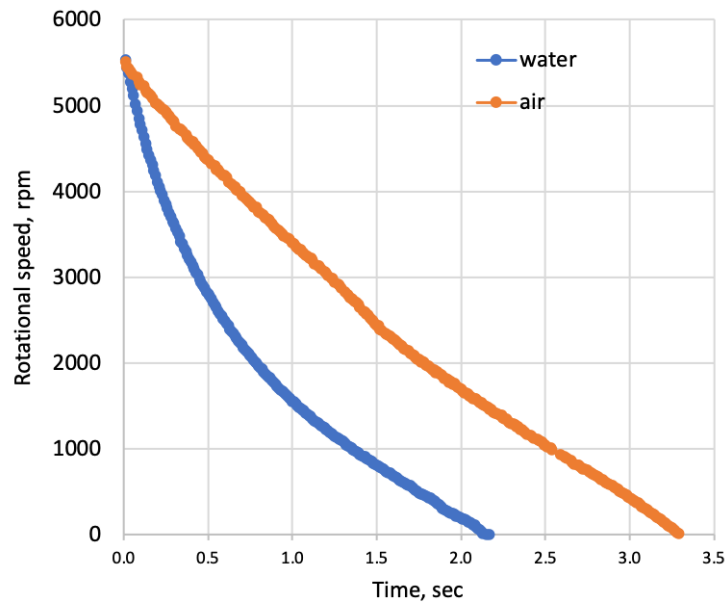
Figure 4.17 Run down test with water and air

Figure 4.18 shows the run-down test data calculated in terms of ventilation power with respect to rotational speed. The ventilation loss for water shows strong quadratic trend with respect to rotational speed. We can see that ventilation losses are significant if we compare the design power of the machine, which is 1.4 kW @10000 rpm. The ventilation power loss is greater than design power. Hence there is no production of positive power at higher rotational speed. The positive power produced by the turbine at lower rotational speed, as shown in Figure 3.18, is due to lower ventilation losses. On the other hand, when turbine is empty and it's rotating in air, it is clear that ventilation viscous losses are now almost negligible. The ventilation power loss in air represents the mechanical power loss in the expander. This is validated as the mechanical seal used in the expander has nominal power loss of 300 W @10000 rpm as per seal catalogue. Hence, when water is present, the major source of losses in the expander is ventilation loss due to rotating surfaces and casing.
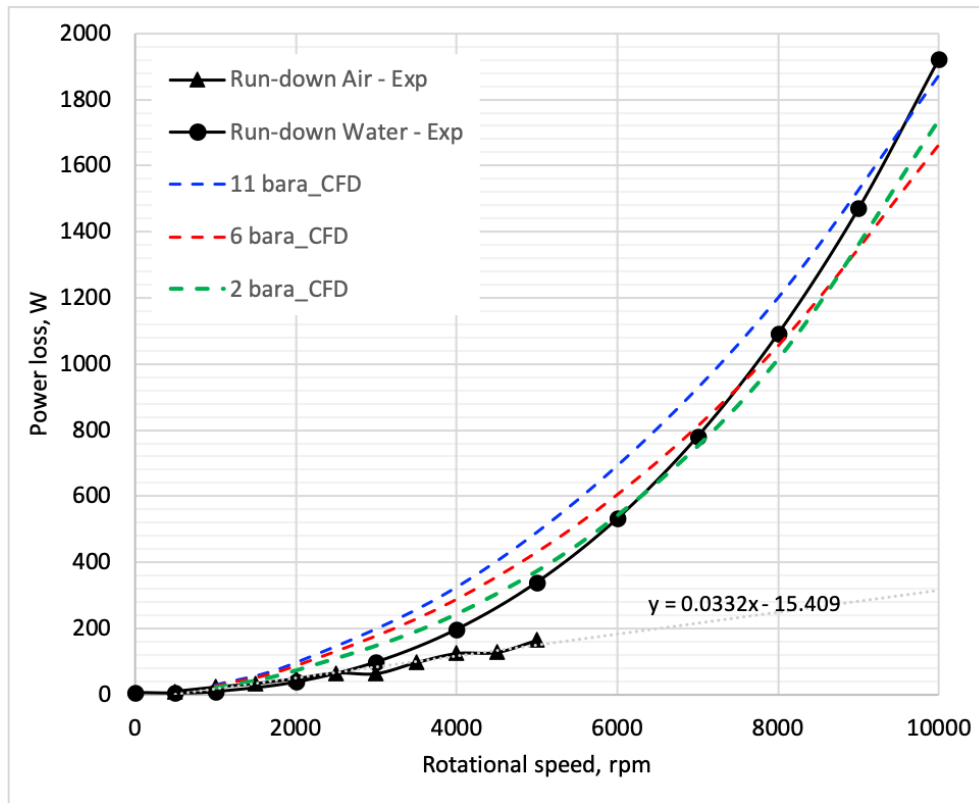
Figure 4.18 Ventilation loss with water and air

In order to reduce and optimise the ventilation loss in water expander, numerical validated model of stator-rotor cavity is needed. A 2-D CFD simulation with rotor and stator is performed and compared with the experimental data.

The 2 D CFD geometry and mesh is shown in Figure 4.19. The mesh is done in such a way that the Y+ ~ 1 and it is not sensitive to output variables like torque and outlet velocity. Steady, incompressible and axisymmetric 2-D analysis is performed using coupled solver for faster convergence. The turbulence model k-w SST is used to accurately capture wall parameters.
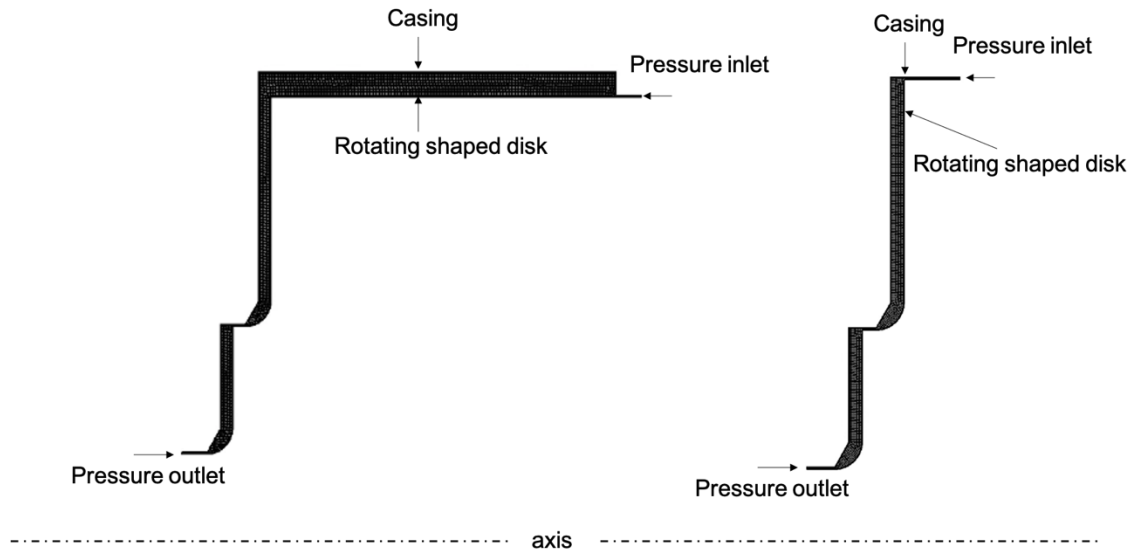
Figure 4.19 2-D CFD model for both sides of rotor

The simulation is run for different inlet boundary conditions of inlet pressure and rotational speeds. The results for ventilation power loss for 10 bara, 6 bar and 2 bar are shown in Figure 4.18 along with experimental ventilation loss curve. During the experimental run-down test, the peripheral pressure of the rotor changes continuously as the rotational speed goes down. Hence the CFD simulation is run for different inlet pressures. The mechanical power loss in the turbine, i.e. ventilation power loss measured in air, is added to the CFD calculated power loss to get the total ventilation power loss, which is comparable to experimental power loss. We can see that there is very good match between numerical and experimental curves. It is interesting to see the intersection between CFD power loss curves at different peripheral rotor pressures and experimental power loss curve. Power loss curve with 10 bara pressure intersects the experimental curve at higher rotational speed ~9500 rpm, 6 bara CFD curve intersects at lower rotational speed, ~ 7500 rpm, and 2 bara CFD curve intersects at ~6000 rpm. This behaviour is expected as in the experimental run-down test peripheral static pressure increases with rotational speed.

In the near future, the validated 2-D model can be further used to optimise and reduce the power loss due to ventilation, applying conventional approaches (e.g. increase in clearance and high surface finish) as well as innovative concepts (e.g. superficial features).

Chapter 5   Comprehensive conclusions

5.1   Conclusions

This thesis focused on the development of a systematic approach to Tesla expander design, supported by a detailed experimental investigation of bladeless micro expander prototypes - 100W air, 3kW air and 1 kW water.

A 0-D algorithm for Tesla rotor design is presented. This algorithm is used in the initial design phase of Tesla expanders. The geometry and thermodynamic parameters evaluated from the algorithm are compared with 2-D CFD results. The geometry parameters indeed produce a highly efficient rotor design as verified with 2-D CFD analysis. Moreover, the algorithm predicts the power and efficiency in an acceptable range. This tool is used in the design of the Tesla prototypes studied in this thesis.

The performance of the three prototypes is evaluated using 3D numerical simulation. This study also summarizes the comparison of numerical models with experimental results for three prototypes. There is good agreement between the CFD model and experimental data.

The stator and rotor of both air expanders are numerically characterised using the following parameters: total pressure loss coefficient, degree of reaction, tip velocity ratio, number of nozzles, rotational speed and streamline plots for the number of turns of fluid inside the rotor.

Total pressure loss coefficient between the inlet of nozzle till rotor periphery is evaluated computationally, which correlates to the overall stator efficiency. Using this coefficient, rotor and stator efficiencies are computed separately. It is seen that the total pressure loss coefficient is higher for low rotational speeds for the same nozzle inlet conditions. Corresponding rotor efficiencies are also low at a low rotational speed. In general, stator and stator-rotor interaction losses are demonstrated to play the major role in rotor efficiency reduction.

Degree of reaction, which indicates the static pressure drop in the rotor with respect to the overall pressure drop in the stage, is computed for different cases. Higher degrees of reaction is observed at higher expander efficiency cases. The optimum degree of reaction for the expander is found to be between 0.3-0.4.

It is confirmed that a higher number of nozzles improves the performance of the expander for the same mass flow condition in each discrete number of nozzles case. In this study, the effect of a number of nozzles with the same inlet nozzle pressure is illustrated, with the following conclusions:

   a. Axisymmetric inflow condition at rotor inlet - increases with the number of nozzles

   b. Total pressure loss coefficient - decreases with the number of nozzles

   c. Degree of reaction – Increases with number of nozzles

All the above parameters increase the performance of the expander at a higher number of nozzles, however, there is also the influence of mass flow, which negatively impacts rotor efficiency. Due to the higher mass flow at a higher number of nozzles, there is a peak of rotor efficiency with respect to the number of nozzles. Even if the rotor is independently designed with high efficiency, stator flow influences greatly the rotor inflow conditions, which significantly degrades the rotor efficiency as shown in the case of 100W and 3 kW expanders for high inlet pressure cases.

Experimental campaign tests are presented for all three prototypes.

100W Air turbine: Experimental analysis focused mainly on the efficiency features of this expander, showing the impact on performance of different disk gaps, disk thickness, discharge holes, exhaust geometry, as a function of speed and mass flow. Maximum adiabatic efficiency of 18% has been measured, with many other points in the 10-15% range. Results show that the three largest sources of losses are the stator losses (which include the nozzle and nozzle-rotor interaction losses), the leakages losses (due to flow bypassing the rotor at the extremes gaps), and ventilation losses. The nozzle losses account, alone, for about 2/3 of overall losses. Therefore, it is clear that future efforts for improving bladeless turbomachinery performance necessarily need to focus on nozzle design, rotor casing design, and nozzle-disk interaction analysis.

3 kW air turbine: This is the first-ever Tesla turbine designed and successfully tested with the integrated high-speed generator at a 3-kW design power scale.

- Maximum isentropic efficiency is obtained for the two-nozzle case which is 36.5% at 10000 rpm. This is the highest Tesla turbine efficiency recorded till now for actual prototypes with air as a working fluid.
- Stator losses have been characterized using nozzle loss coefficient and nozzle efficiency parameter. In this nozzle design, a lower nozzle loss coefficient has been obtained for the Tesla turbine compared to the literature. Nozzle efficiency parameter as high as ~ 0.9 is obtained.
- Two nozzles mounted in diagonally opposite direction perform better than a single nozzle due to couple effect on the rotor and axisymmetric flow which improves the inflow rotor conditions.
- Ventilations loss, rotor inflow conditions and leakage losses play a very important role in shifting the peak efficiency of the turbine.

The experimental loss characterisation of such 3-kW air turbine prototype with high-speed generator is carried out. The losses studied are (i) stator losses, (ii) ventilation losses and (iii) leakage losses.

- Stator losses have the maximum contribution in lowering the performance of the Tesla turbine. These losses can lower the efficiency of the turbine by 40 points.
- Ventilation losses depend on the clearance between the casing and the last disk(s). These losses increase quadratically with the rotational speed of the rotor.
- Leakage mass flow is correlated with nozzle exit pressure. As there is no specific sealing system used in the turbine prototype, we have seen these losses impacting as high as 15 points on the overall efficiency of the turbine.
- The contribution of each loss mechanism, on the overall performance of the turbine, is shown.

Water expander: In this turbine novel design features are used and tested. The performance of the expander was found to be lower than predicted numerically. This is due to the significant ventilation power loss and leakage loss between rotor and stator cavities. The 2-D CFD

simulation of ventilation loss shows very good agreement with experimentally evaluated power loss. The validated 2-D CFD methodology can be used to optimise the ventilation losses which can be likely reduced in the near future, conventional approaches.

Finally, Ventilation losses and leakage losses maybe both effectively addressed by employing a proper sealing system. Stator losses have been demonstrated to mostly affect the Tesla expander performance; therefore, they need to be carefully addressed for overcoming the traditional low-performance feature of bladeless expanders.

5.2   Future Work

In the context of the study presented in this thesis, the following work is recommended to be carried out for the further understanding of Tesla turbomachinery:

1. Improvement in the 0-D model to accurately evaluate the inlet total pressure at the rotor, either by implementing it with a 1-D analytical solution for the rotor or by experimental correlations.
2. Implementation of supersonic nozzles for Tesla expanders and detailed studies about shock wave interaction with Tesla rotor and its effect on the performance.
3. Optimisation of rotor-casing cavities to reduce the ventilation losses for high-density fluids such as water and supercritical CO_2.
4. To develop design and optimisation methodology for radial diffusers of Tesla expanders.

References

[1] Tesla, N., 1913, "Turbine", US Patent 1061206.

[2] Tesla, N.,1913, "Fluid Propulsion", US Patent 1061142.

[3] Armstrong, J. H., 1952, "An Investigation of the Performance of a Modified Tesla Turbine", Ph.D. Thesis, Faculty of the Division of Graduate Studies, Georgia Institute of Technology, USA.

[4] Beans, E. W., 1961, "Performance Characteristics of a Friction Disk Turbine", *Ph.D Thesis*, The Pennsylvania State University, USA.

[5] Rice, W., 1965, "An Analytical and Experimental Investigation of Multiple Disk Turbines", *Journal of Engineering for Power,* Vol. 87(1), pp. 29–36.

[6] Bloudíček, P., and Paloušek, D., 2007, "Design of Tesla Turbine", Konference diplomových prací, Brno, Česká republika.

[7] Hoya, G. P., and Guha, A., 2008, "The Design of a Test Rig and Study of the Performance and Efficiency of a Tesla Disc Turbine", *Journal of Power and Energy*, Vol. 223 Part A, pp. 451–65.

[8] Guha, A., and Smiley, B., 2009, "Experiment and Analysis for an Improved Design of the Inlet and Nozzle in Tesla Disc Turbines", *Journal of Power and Energy*, Vol. 224 Part A, pp. 261–277.

[9] Vedavalli, K., Zoghora, I., and Michel, M., 2011, "A Micro Tesla Turbine for Power Generation from Low Pressure Heads and Evaporation Driven Flows", *IEEE, Transducers'11*, Beijing, China, pp. 1851-1854.

[10] Peshlakai, A., 2012, "Challenging the Versatility of Tesla Turbine-Working Fluid Variations and Turbine Performance", Master Thesis, Arizona State University, Arizona, USA.

[11]   Holland, K., 2015, "Design, Construction and Testing of a Tesla Turbine", Master Thesis, Laurentian University Sudbury, Ontario, Canada.

[12]   Li, R., Huanran, W., Erren, Y., Meng, L., and Weigang, N., 2017, "Experimental Study on Bladeless Turbine Using Incompressible Working Medium", *Advances in Mechanical Engineering, Vol. 9(1),* pp. 1–12.

[13]   Schosser, C., 2016, "Experimental and Numerical Investigations and Optimisation of Tesla Radial Turbines", Master Thesis, Universität der Bundeswehr München Fakultät für Luft und Raumfahrttechnik Institut für Thermodynamik, Germany.

[14]   Manfrida, G., Pacini L., and Talluri, L., 2017, "A Revised Tesla Turbine Concept for ORC Applications", *Energy, Vol. 129*, pp. 1055–1062.

[15]   Rusin, K., Wroblewski, W., and Strozik, M., 2018, "Experimental and Numerical Investigation of Tesla Turbine", *Journal of Physics*: Conf. series 1101 012029.

[16]   Okamoto, K., and Goto, K.,2017, "Experimental Investigation of Inflow Condition Effects on Tesla Turbine Performance", *ISABE, International Symposium on Air Breathing Engine*, pp. 1-11.

[17]   Manfrida, G., Pacini L., and Talluri, L., 2018, "An Upgraded Tesla Turbine Concept for ORC Applications", *Energy*, Vol. 158, pp. 33-40.

[18]   Ladino, A.F.R., 2004, "Numerical Simulation of the Flow Field in a Friction–Type Turbine (Tesla Turbine)", M.Sc. Thesis, Vienna University of Technology.

[19]   Ladino, A.F.R, 2004, "Numerical Simulation of the Flow Field in a Friction–Type Turbine (Tesla Turbine)", Technical report, Vienna University of Technology.

[20]   Lemma, E., Deam, R.T., Toncich, D., and Collins, R., 2008, "Characterisation of a Small Viscous Flow Turbine", *Experimental Thermal and Fluid Science*, Vol. 33, pp 96–105.

[21]   Lampart, P., Kosowski, K., Piwowarski, M., and Jedrzejewski, L., 2009, "Design Analysis of Tesla Micro–turbine Operating on a Low–boiling Medium", Polish Maritime Research, pp. 28–33.

[22]   Rusin, K., Wróblewski, W., and Strozik, M., 2018, "Experimental and Numerical Investigations of Tesla Turbine", *Journal of Physics*, Conf. Series 1101 (2018) 012029.

[23]   Qi, W., Deng, W., Chi, Z., Hu, L., Yuan, Q., and Feng, Z., 2019, "Influence of Disc Tip Geometry on the Aerodynamic Performance and Flow Characteristics of Multichannel Tesla Turbines", *Energies*, Vol. 12, pp. 572.

[24]   Wang, B., Okamoto, K., Yamaguchi, K., and Teramoto, S., 2014, "Loss Mechanisms in Shear-Force Pump with multiple corotating disks", *Journal of Fluids Engineering*, Vol. 136, 081101-1

[25]   Sengupta, S., and Guha, A., 2008, "Inflow-rotor interaction in Tesla disc turbines: Effects of discrete inflows, finite disc thickness, and radial clearance on the fluid dynamics and performance of the turbine", *Proc IMechE Part A: J Power and Energy*, 0(0), 1-21

[26]   Steidel, R., Weiss H., 1976, "Performance Test of a Bladeless Turbine for Geothermal Applications". Technical Report, UCID–17068, California Univ., Livermore (USA), Lawrence Livermore Lab.

[27]   Patel, N., Schmidt, D.D., 2002, "Biomass Boundary Layer Turbine Power System", *Proceedings of International Joint Power Generation Conference*, Phoenix, USA.

[28]   Deam R.T., Lemma E., Mace B., and Collins R., 2008, "On Scaling Down Turbines to Millimeter Size", *Transaction of ASME*, *Journal of Engineering for Gas Turbines and Power*, Vol. 130, pp. 1–9.

[29]   Valente, A., 2008, "Installation for Pressure Reduction of Hydrocarbon Gases in a Near Isothermal Manner", Proceedings of Abu Dhabi International Petroleum Exhibition and Conference.

[30]   Crowell, R., 2009, "Generation of Electricity Utilizing Solar Hot Water Collectors and a Tesla Turbine", Proceedings of the ASME 3rd International Conference of Energy Sustainability, California.

[31]   Cirincione, N., 2011, "Design, Construction and Commissioning of An Organic Rankine Cycle Waste Heat Recovery System with a Tesla Hybrid Turbine Expander", M.Sc. Thesis, Colorado State University.

[32]   Ho–Yan, B.P., 2011, "Tesla Turbine for Pico Hydro Applications", *Guelph Engineering Journal*, Vol. 4, pp. 1–8.

[33]   Zhao, D., Khoo, J., 2013, "Rainwater and Air Driven 40 MM Bladeless Electromagnetic Energy Harvester", *Appl. Physics Letters*, Vol. 103, pp. 1–4.

[34] Ruiz, M., 2015, "Characterization of Single Phase and Two–Phase Heat and Momentum Transport in a Spiralling Radial Inflow Micro Channel Heat Sink", Ph.D. thesis, Berkeley University, California.

[35] Thawichsri, K., and Nilnont, W., 2015, "A Comparing on the Use of Centrifugal Turbine and Tesla Turbine in An Application of Organic Rankine Cycle", *International Journal of Advanced Culture Technology*, Vol. 3, pp. 58–66.

[36] Bankar N., Chavan A., Dhole S., and Patunkar P., 2016, "Development of Hybrid Tesla Turbine and Current Trends in Application of Tesla Turbine", *International Journal for Technological Research in Engineering*, Vol. 3, pp. 1504–1507.

[37] Umashankar, M., Anirudh, V., and Pishey K., 2017, "Investigation of Tesla Turbine", in: *International Journal of Latest Technology in Engineering, Management & Applied Science*, Vol. 6, pp. 23–27.

[38] Manfrida, G., Pacini, L., and Talluri L., 2018, "An Upgrade Tesla Turbine Concept for ORC Applications", in: *Energy*, Vol. 158, pp. 33–40.

[39] Traverso, A., Barberis, S., Larosa, L., and Silvestri, P., 2018, "Reverse Cycle Machine Provided with a Turbine", World Patent, WO2018/127445A1.

[40] Traverso, A., Silvestri, P., Reggio, F., and Efstathiadisa, T., 2019, "Theoretical and Experimental Investigation on Rotor Dynamic Behaviour of Bladeless Turbine for Innovative Cycles", Proceedings: ASME TurboExpo'19, Phoenix, USA

[41] Schlichting, H., Boundary Layer Theory, McGraw-Hill Book Co., Inc., New York, NY, fourth Ed.,1962, p- 547.

[42] Breiter. M. C, and Pohlhausen. K., "Laminar Flow Between Two Parallel Rotating Disks", Aeronautical Research Laboratories, Wright-Patterson AFB, Ohio, Report No. ARL 62-318

[43] Balje O.E., Turbomachines, a guide to design, selection and theory, John Wiley and sons, New York, 1981.

[44] Renuke, A., Vannoni, A., Traverso, A., and Pascenti, M., 2019, "Experimental and Numerical Investigation of Small-Scale Tesla Turbines", *ASME. Journal of Engineering Gas Turbines Power*, Vol. 141(12), 121011.

[45]   Renuke, A., Reggio, F., Pascenti, M., Silvestri, P and Traverso, A., 2020, "Experimental Investigation on a 3 kW Tesla Expander with High Speed Generator", ASME. TurboExpo'20, GT2020-14572, London, England.

[46]   Arduino Hardware, https://www.arduino.cc/, last access 01/11/2018

[47]   Moffat, R. J., 1985, "Using Uncertainty Analysis in the Planning of an Experiment", *Journal of Fluids Engineering*, *Vol 107*, pp 173–178.

[48]   Taylor, J. R., 1997, "An Introduction to Error Analysis: The Study of Uncertainties in Physical Measurements", University Science Books, Sausalito, CA.

[49]   Idelchik, I. E., 1960, "Handbook of Hydraulic Resistance, Coefficients of Local Resistance and of Friction", Gosudarstvennyi.

[50]   Cohen, H., Rogers, G. F. C., and Saravanamuttoo, H. I. H. Gas turbine theory, 4th edition, 1996 (Longman Group Ltd, Cornwall).

[51]   Hasinger. S. H, Kehrt. L.G, "Investigation of Shear Force Pumps", *Journal of Engineering for Power*, Trans. ASME series A, Vol-85, July-1963, pp -201-207

[52]   Carey, V., P., 2010, "Assessment of Tesla Turbine Performance for Small Scale Rankine Combined Heat and Power Systems", *Journal of Engineering for Gas Turbines Power, Vol. 132*, pp. 1–8.

[53]   Romanin, V., D., 2012, "Theory and Performance of Tesla Turbines", Ph.D. Thesis, UC Berkeley, USA.

[54]   Song, J., Ren, X., Li, X., Gu, C., and Zhang, M., 2018, "One-dimensional model analysis and performance assessment of Tesla turbine", *Applied Thermal Engineering, 134, pp 546-554.*

[55]   Benedict, R. P., Wyler, J. S., Dudek, J. A., and Gleed, A. R., 1996, "Generalized Flow Across an Abrupt Enlargement." Trans. ASME, J. Eng. Power, Vol 98, pp 327–334.

[56]   Daily, J.W., and Nece, R.E., 1960, "Chamber Dimension Effects on Induced Flow and Frictional Resistance of Enclosed Rotating Disks", ASME, *Journal of Basic Engineering*, pp. 217-230.

[57]   Hu, Bo., Brillert, D., Dohmen, H,J., and Benra, F, 2017, "Investigation on the Flow in a Rotor-Stator Cavity with Centripetal Through-Flow", *International Journal of Turbomachinery Propulsion and Power*, Vol. 2, pp. 18

Bibliography

A complete bibliography on Tesla expanders in chronological order.

1900 – 1950

Tesla N., Turbine, U.S. Patent No. 1 061 206, 1913.

Tesla, N., Fluid propulsion", US Patent 1061142, 1913

Leaman A.B., The design, construction and investigation of a Tesla turbine, M.Sc. Thesis, University of Maryland, 1950.

Armstrong J.H., An Investigation of the Performance of a Modified Tesla Turbine, M.Sc. Thesis, Georgia Institute of Technology, 1952.

1950 – 2000

Beans E.W., Performance characteristics of a Friction Disc Turbine, Ph.D. Thesis, Pennsylvania State University, 1961.

Breiter, M. C., and Pollhausen, K., Laminar Inward Flow Between Two Parallel Rotating Disks, Report No. ARL 62-218, Aeronautical Research Laboratories, Wright-Patterson Air Force Base, Dayton, Ohio, March 1962.

Rice W., "An analytical and experimental investigation of multiple–disk turbines", in: ASME Journal of Engineering for Power, 87, 29–36, 1965.

Beans E.W., "Investigation into the performance characteristics of a friction turbine", in: J. Spacecraft, 3, 131–134, 1966.

Matsch L., Rice W., "Potential flow between two parallel circular disks with partial admission", in: Transactions of the ASME, Journal of Applied Mechanics, 1967.

Matsch L., Rice W., "Flow at low Reynolds number with partial admission between rotating disks", in: Transactions of the ASME, Journal of Applied Mechanics, 1967.

Boyd K.E., Rice W., "Laminar inward flow of an incompressible fluid between rotating disks, with full peripheral admission", in: Journal of Applied Mechanics, 229–237, 1968.

Matsch L., Rice W., "An asymptotic solution for laminar flow of an incompressible fluid between rotating disks", in: Transactions of the ASME, Journal of Applied Mechanics, 1968.

Adams R., Rice W., "Experimental investigation of the flow between corotating disks", in: Transactions of the ASME, Journal of Applied Mechanics, 844–849, 1970.

Boyak B.E., Rice W., "Integral method for flow between corotating disks", in: ASME Journal of Basic Engineering, 93, 350–354, 1971.

Lawn M.J., An investigation of multiple–disk turbine performance parameters, M.Sc. Thesis, Arizona State University, 1972.

Lawn M.J., Rice W., "Calculated design data for multiple–disk turbine using incompressible fluid", in: Transactions of the ASME, Journal of Fluid Engineering, 252–258, 1974.

Pater L.L., Crowther E., Rice W., "Flow regime definition for flow between corotating disks"in: Transactions of the ASME, Journal of Fluid Engineering, 29– 34, 1974.

Bassett C.E., "An integral solution for compressible flow through disc turbines", in: Proceedings of the 10th Intersociety Energy Conversion Engineering Conference, Newark, Delaware, 1975.

Garrison P.W., Harvey D.W., Catton I., "Laminar compressible flow between rotating disks", in: Transactions of the ASME, Journal of Fluid Engineering, 382– 388, 1976.

Steidel R., Weiss H., "Performance test of a bladeless turbine for geothermal applications". Technical Report Report No. UCID–17068, California Univ., Livermore (USA), Lawrence Livermore Lab., 1976.

Truman C.R., Rice W., Jankowski D.F., "Laminar throughflow of varying–quality steam between corotating disks", in: Transactions of the ASME, Journal of Fluid Engineering, 194– 200, 1978.

Truman C.R., Rice W., Jankowski D.F., "Laminar throughflow of a fluid containing particles between corotating disks", in: Transactions of the ASME, Journal of Fluid Engineering, 87– 92, 1979.

Allen J.S., A model for fluid between parallel, co–rotating annular disks, M.Sc. Thesis, University of Dayton, Ohio, 1990.

Rice W., "Tesla Turbomachinery", in: Proceedings of IV International Nikola Tesla Symposium, 1991

2000 - 2010

Sandilya P., Biswas G., Rao D.P., Sharma A., "Numerical simulation of the gas flow and mass transfer between two coaxially rotating disks", in: Numerical Heat Transfer, 39, 285–305, 2001.

Patel N., Schmidt D.D., "Biomass boundary layer turbine power system", in: Proceedings of International Joint Power Generation Conference, Phoenix, 2002.

Lezsovits F., "Decentralized energy supply possibilities based on biomass", in: PERIODICA POLYTECHNICA SER. MECH. ENG., 47, 151–168, 2003.

Ladino A.F.R., "Numerical simulation of the flow field in a friction–type turbine (Tesla turbine)", Technical Report, Vienna University of Technology, 2004.

Ladino A.F.R, Numerical simulation of the flow field in a friction–type turbine (Tesla turbine), M.Sc. Thesis, Vienna University of Technology, 2004.

Couto H.S., Duarte J.B.F., Bastos–Neto D., "The Tesla turbine revisited", in: 8th Asia–Pacific International symposium on Combustion and Energy Utilization, Sochi, 2006.

Batista M., "A note on steady flow of incompressible fluid between two co–rotating disks", in: Physics, Cornell University Library, 2007.

Bloudicek P., Palousek D., "Design of Tesla turbine", in: Proceedings of Konference diplomovych praci, Brno, 2007.

Deam R.T., Lemma E., Mace B., Collins R., "On scaling down turbines to millimeter size", in: Transaction of ASME, Journal of Engineering for Gas Turbines and Power, 130, 1–9, 2008.

Lemma E., Deam R.T., Toncich D., Collins R., "Characterisation of a small viscous flow turbine", in: Experimental Thermal and Fluid Science, 33, 96–105, 2008.

Valente A., "Installation for pressure reduction of hydrocarbon gases in a near isothermal manner", in: Proceedings of Abu Dhabi International Petroleum Exhibition and Conference, 2008.

Crowell R., "Generation of electricity utilizing solar hot water collectors and a Tesla turbine", in: Proceedings of the ASME 3rd International Conference of Energy Sustainability, California, 2009.

Hoya G.P., Guha A., "The design of a test rig and study of the performance and efficiency of a Tesla disc turbine", in: Proc. IMechE, Part A: J. Power and Energy, 223, 451–465, 2009.

Guha A., Smiley B., "Experiment and analysis for an improved design of the inlet and nozzle in Tesla disc turbines", in: Proc. IMechE, Part A: J. Power and Energy, 224, 261–277, 2009.

Lampart P., Kosowski K., Piwowarski M., Jedrzejewski L., "Design analysis of Tesla micro–turbine operating on a low–boiling medium", in: Polish Maritime Research, 28–33, 2009.

Carey V.P., "Assessment of Tesla Turbine Performance for Small Scale Rankine Combined Heat and Power Systems", in: J. Eng. Gas Turbines Power, 132, 1–8; 2010.

Carey V.P., "Computational/Theoretical Modelling of Flow Physics and Transport in Disk Rotor Drag Turbine Expanders for Green Energy Conversion Technologies", in: Proc. of the ASME 2010 International Mechanical Engineering Congress & Exposition, Vancouver, Canada; 2010.

Emran T.A., Alexander R.C., Stallings C.R., DeMay M.A., Traum M.J., "Method to accurately estimate Tesla turbine stall torque for dynamometer or generator load selection", in: ASME Early Career Technical Journal, Atlanta, 2010.

Puzyrewski R., Tesch K., "1D model calibration based on 3D calculations for Tesla turbine", in: Task quarterly, scientific bulletin of academic computer centre in Gdansk, 14, 237–248, 2010.

Romanin V., Carey, V.P., Norwood, Z., "Strategies for performance enhancement of Tesla turbines for combined heat and power applications", in: Proceedings of the ASME 4th International Conference on Energy Sustainability, Phoenix, 2010.

2010- 2022

Batista M., "Steady flow of incompressible fluid between two co–rotating disks", in: Appl. Mathematical Modelling, 35, 5225–5233, 2011.

Choon T.W., Rahman A.A., Jer F.S., Aik L.E., "Optimization of Tesla turbine using Computational Fluid Dynamics approach", in: IEEE Symposium on Industrial Electronics and Applications (ISIEA2011), 2011.

Cirincione N, Design, construction and commissioning of an organic Rankine cycle waste heat recovery system with a Tesla hybrid turbine expander, M.Sc. Thesis, Colorado State University, 2011.

Emran T.A., Tesla turbine torque modelling for construction of a dynamometer and turbine, M.Sc. Thesis, University of North Texas, 2011.

Ho–Yan B.P., "Tesla turbine for Pico Hydro applications", in: Guelph Engineering Journal, 4, 1–8, 2011.

Krishnan V.G., Iqbal Z., Maharbiz M.M., "A micro Tesla turbine for power generation from low pressure heads and evaporation driven flows", in: Proceedings of Transducers '11, Beijing, 2011.

Lampart P., Jedrzejewski L., "Investigations of aerodynamics of Tesla bladeless microturbines", in: Journal of Theoretical and Applied Mechanic, 49, 2, 477–499, 2011.

Podergajs M., The Tesla Turbine, Seminar notes, University of Ljubiana, 2011.

Romanin V.D., Carey V.P., "An integral perturbation model of flow and momentum transport in rotating microchannels with smooth or microstructured wall surfaces", in: Physics of Fluids, 23, 1–11, 2011.

Borate H.P., Misal N.D., "An effect of surface finish and spacing between discs on the performance of disc turbine", in: International Journal of Applied Research in Mechanical Engineering, 2, 25–30, 2012.

Peshlakay A., Challenging the versatility of the Tesla turbine: Working fluid variations and turbine performance, M.Sc. Thesis, Arizona State University, 2012.

Romanin V.D., Krishnan V.G., Carey V.P., Maharbiz M.M., "Experimental and analytical study of a sub–watt scale Tesla turbine performance", in: Proceedings of the ASME 2012 International Mechanical Engineering Congress & Exposition, Houston, 2012.

Romanin V.D., Theory and Performance of Tesla turbines, Ph.D. Thesis, Berkeley University, California, 2012.

Sengupta S., Guha A., "A theory of Tesla disc turbines", in: Proc. of the Institution of Mechanical Engineers, Part A: Journal of Power and Energy, 226, 651–663, 2012.

Bao G., Shi Y., Cai N., "Numerical modelling research on the boundary layer turbine using organic working fluid", in: Proceeding of International Conference on Power Engineering (ICOPE–13), Wuhan, China, 2013.

Deng Q., Qi W., Feng Z., "Improvement of a theoretical analysis method for Tesla turbines", in: Proceedings of ASME Turbo Expo 2013: Turbine Technical Conference and Exposition, San Antonio, 2013.

Guha A, Sengupta S, "The fluid dynamics of the rotating flow in a Tesla disc turbine", in: European Journal of Mechanics B/Fluids, 37, 112–123, 2013.

Gupta H.E., Kodali S., "Design and Operation of Tesla turbo machine – A state of the art review", in: International Journal of Advanced Transport Phenomena, 2, 7– 14, 2013.

Khan M.U.S., Ali E., Maqsood M.I., Nawaz H., "Modern improved and effective design of boundary layer turbine for robust control and efficient production of green energy", in: 6th Vacuum and surface conference of Asia and Australia, Journal of Physics conference series 349, 2013.

Khan M.U.S, Maqsood M.I., Ali E., Jamal S., Javed M., "Proposed applications with implementation techniques of the upcoming renewable energy resource, the Tesla turbine", in: 6th Vacuum and surface conference of Asia and Australia, Journal of Physics conference series 349, 2013.

Krishnan V.G., Romanin V.D., Carey V.P., Maharbiz M.M., "Design and scaling of microscale Tesla turbines", in: Journal of Micromechanics and Microengineering, 23, 2013.

Sengupta S., Guha A., "Analytical and computational solutions for three– dimensional flow– field and relative pathlines for the rotating flow in a Tesla disc turbine", in: Computers & Fluids, 88, 344–353, 2013.

Yang Z., Weiss H.P., Traum M.J. "Dynamic dynamometry to characterize disk turbines for space–based power", in: Proceedings of the Wisconsin Space conference, 2013.

Zhao D., Khoo J., "Rainwater and air driven 40 mm bladeless electromagnetic energy harvester", in: Appl. Physics Letters, 103, 1–4, 2013.

Guha, A., Sengupta S., "Similitude and scaling laws for the rotating flow between concentric discs", in: Proceedings of the Institution of Mechanical Engineers, Part A, Journal of Power and Energy, 28, 429–439, 2014.

Guha, A., Sengupta S., "The fluid dynamics of work transfer in the non–uniform viscous rotating flow within a Tesla disc turbomachine", Physics of Fluids, 26, 1–27, 2014.

Hasan A., Benzamia A., "Investigating the impact of air temperature on the performance of a Tesla turbine – using CFD modelling", in: International Journal of engineering Innovation & Research, 3, 794–802, 2014.

Pandey R.J., Pudasaini S., Dhakal S., Uprety R.B., Neopane H.P., "Design and Computational Analysis of 1 kW Tesla turbine", in: International Journal of Scientific and Research Publications, 4, 1–5, 2014.

Schosser C., Lecheler S., Pfizner M., "A test rig for the investigation of the performance and flow field of Tesla friction turbines", in: Proceedings of ASME Turbo Expo 2014: Turbine Technical Conference and Exposition, Dusseldorf, 2014.

Shimeles S., Design, simulation of fluid flow and optimization of operational parameters in Tesla multiple–disk turbine, M.Sc. Thesis, Addis Ababa University Institute of Technology, 2014.

Siddiqui M.S., Ahmed H., Ahmed S., "Numerical simulation of a compressed air driven Tesla turbine", in: Proceedings of the ASME 2014 Power Conference, Baltimore, 2014.

Singh A., "Inward flow between stationary and rotating disks", in: Journal of Fluids Engineering, 136, 1–5, 2014.

Thawichsri K., Nilnont W., "A study on performance comparison of two–size Tesla turbines application in Organic Rankine Cycle machine", in: International Symposium on the Fusion Technologies, Jeonju, 2014.

Zhao D., Ji C., Teo C., Li S., "Performance of small–scale bladeless electromagnetic energy harvesters driven by water or air", in: Energy, 74, 99–108, 2014.

Baginski P., Jedrzejewski L., "The strength and dynamic analysis of the prototype of the Tesla turbine", in: Diagnostyka, 16, 17–24, 2015.

Holland K., Design, construction and testing of a Tesla Turbine, M.Sc. Thesis, Laurentian University, Sudbury, 2015.

Kölling A., Lisker R., Hellwig U., Wildenauer F., "Friction expander for the generation of electricity (fege)". In: International Conference on Renewable Energies and Power Quality (ICREPQ'15), La Coruna, 2015.

Krishnan V., Design and Fabrication of cm–scale Tesla Turbines, Ph.D. Thesis, Berkeley University, California, 2015.

Neckel A.L., Godinho M., "Influence of geometry on the efficiency of convergent– divergent nozzles applied to Tesla turbines", in: Experimental Thermal and Fluid Science, 62, 131–140, 2015.

Nedelcu, D., Guran P., Cantaragiu A., "Theoretical and experimental research performed on the Tesla turbine", in: Analele Universitatii Eftimie Murgu resita, 22, 255–263, 2015.

Raje A., Singh B., Churai R., Borwankar P., "A review of Tesla turbine", in: International Journal of Mechanical Engineering and Technology, 6, 28–31, 2015.

Ruiz M., Characterization of single phase and two–phase heat and momentum transport in a spiralling radial inflow micro channel heat sink, Ph.D. thesis, Berkeley University, California, 2015.

Ruiz M., Carey V.P., "Experimental study of single phase heat transfer and pressure loss in a spiralling inflow micro channel heat sink", in: ASME Journal of Heat Transfer, 137, 1–8, 2015.

Schosser C., Pfitzner M., "A numerical study of the three–dimensional incompressible rotor airflow within a Tesla turbine", in: Conference on Modelling Fluid Flow (CMFF'15), Budapest, 2015.

Thawichsri K., Nilnont W., "A comparing on the use of centrifugal turbine and Tesla turbine in an application of organic Rankine cycle", in: International Journal of Advanced Culture Technology, 3, 58–66, 2015.

Bankar N., Chavan A., Dhole S., Patunkar P., "Development of hybrid Tesla turbine and current trends in application of Tesla turbine", in: International Journal for Technological Research in Engineering, 3, 1504–1507, 2016.

Herrmann–Priesnitz B., Calderon–Munoz W.R., Salas E.A., Vargas–Uscategui A., Duarte–Mermoud M.A., Torres D.A., "Hydrodynamic structure of the boundary layers in a rotating cylindrical cavity with radial inflow", in: Physics of fluids, 28,1– 16, 2016.

Jose R., Jose A., Benny A., Salus A., Benny B., "An experimental study on the various parameters of Tesla turbine using CFD", in: International Advanced Research Journal in Science, Engineering and Technology, Thiruvananthapuram, 2016.

Jose R., Jose A., Benny A., Salus A., Benny B., "A theoretical study on surface finish, spacing between discs and performance of Tesla turbine", in: International Advanced Research Journal in Science, Engineering and Technology, Thiruvananthapuram, 2016.

Joshi K.N., Sanghvi M.N., Dave T.D., "Hybrid Tesla Pelton wheel turbine", in: International Journal of Scientific & Engineering Research, 7, 1702–1707, 2016.

Qi W., Deng Q., Feng Z., Yuan Q., "Influence of disc spacing distance on the aerodynamic performance and flow field of Tesla turbines", in: Proceedings of ASME Turbo Expo 2016: Turbomachinery Technical Conference and Exposition, Seoul, 2016.

Schosser C., Fuchs T., Hain R., Lecheler S., Kahler C., "Three–dimensional particle tracking velocimetry in a Tesla turbine rotor using a non–intrusive calibration method", in: 18th International Symposium on the Application of Laser and Imaging Techniques to Fluid Mechanics, Lisbon, 2016.

Schosser C., Experimental and numerical investigations and optimisation of Tesla– radial turbines, Ph.D. Thesis, Bundeswehr University, Munich, 2016.

Sengupta, S., Guha A., "Flow of a nanofluid in the micro-spacing within co–rotating discs of a Tesla turbine", in: Appl. Mathematical Modelling, 40, 485–499, 2016.

Zahid I., Qadir A., Farooq M., Zaheer M.A., Qamar A., Zeeshan H.M.A., "Design and analysis of prototype Tesla turbine for power generation applications", in: Technical Journal, University of Engineering and Technology, Taxila, 2016.

Alrabie M.S., Altamimi F.N., Atlarrgemy M.H., Hadi F., Akbar M.K., Traum M.J., "Method to design a hydro tesla turbine for sensitivity to varying laminar Reynolds number modulated by changing working fluid viscosity", in: Proceedings of the ASME Power and Energy Conference, Charlotte, 2017.

Damodhar R., Mruthyunjava K.N., Naveen K., Prabhakar P., Rakhesh H.S., "Design and fabrication of portable water turbine", in: International Research Journal of Engineering and Technology, 4, 2584–2590, 2017.

Guha A., Sengupta S., "A non–dimensional study of the flow through co–rotating discs and performance optimization of a Tesla disc turbine", in: Proc. IMechE Part A: Journal of Power and Energy, 1–18, 2017.

Li R., Wang H., Yao E., Li M., Nan W., "Experimental study on bladeless turbine using incompressible working medium", in: Advances in Mechanical Engineering, 9, 1–12, 2017.

Lisker R., Hellwig U., Wildenauer FX., "Thin film condensation in a Tesla Turbine", in: Wiss Beitr TH Wildau, 21, 71–76, 2017.

Mandal A., Saha S., "Performance analysis of a centimetre scale Tesla turbine for micro–air vehicles", in: International Conference on Electronics, Communication and Aerospace Technology, 2017.

Polisetti S., Charan S.V., Miryala M., "Fabrication and study of the performance affecting the efficiency of a bladeless turbine", in: International Journal of Scientific Research in Science and Technology, 3, 78–82, 2017.

Schosser C., Lecheler S., Pfitzner M., "Analytical and numerical solutions of the rotor flow in Tesla turbines", in: Periodica Polytechnica Mechanical Engineering, 61, 12–22, 2017.

Shah V., Dhokai S., "Tesla turbine experiment", in: International Journal of Science and Research, 6, 113–116, 2017.

Shah V., Dhokai S., Patel P., "Bladeless turbine – a review", in: International Journal of Mechanical Engineering and Technology, 8, 232–236, 2017.

Song J., Gu C.W., "1D model analysis of Tesla turbine for small scale organic Rankine cycle (ORC) system", in: Proceedings of ASME turbo Expo: Turbomachinery Technical Conference and Exposition, Charlotte, 2017.

Song J., Gu C.W., Li X.S., "Performance estimation of Tesla turbine applied in small scale Organic Rankine Cycle (ORC) system", in: Appl. Therm. Eng., 110, 318–326, 2017.

Thiyagarajan V., GokulKumar V., Karthickeyan B., Kumar NE., Nikilaesh A., "Tesla turbine powered solar refrigerator", in: International Journal of Recent Trends in Electrical & Electronics, 4, 50–55, 2017.

Umashankar M., Anirudh V., Pishey K., "Investigation of Tesla turbine", in: International Journal of Latest Technology in Engineering, Management & Applied Science, 6, 23–27, 2017.

Variava J.M., Bhavsar A.S., "Evaluation of Tesla turbo machine as turbine", in: International Journal of Advance Research and Innovative Ideas in Education, 3, 3670–3682, 2017.

Sengupta S., Guha A., "Inflow–rotor interaction in Tesla disc turbines: Effects of discrete inflows, finite disc thickness, and radial clearance on the fluid dynamics and performance of the turbine", in: Proc. IMechE Part A: Journal of Power and Energy, 1–21, 2018.

Song J., Ren X.D., Li X.S., Gu C.W., Zhang M.M., "One–dimensional model analysis and performance assessment of Tesla turbine", in: Appl. Therm. Eng., 134, 546–554, 2018.

Traum M.J., Hadi F., Akbar M.K., "Extending 'assessment of Tesla turbine performance' Model for sensitivity–focused experimental design", in: ASME Journal of Energy Resources Technology, 140, 1–7, 2018.

Manfrida G., Pacini L., Talluri L., "A revised Tesla turbine concept for ORC applications", in: Energy Procedia, 129, 1055–1062, 2017.

Manfrida G., Talluri L., "Fluid dynamics assessment of the Tesla turbine rotor", in: Thermal Science, 2018.

Manfrida G., Pacini L., Talluri L., "An upgrade Tesla turbine concept for ORC applications", in: Energy, 158, 33–40, 2018.

Talluri L., Fiaschi D., Neri G., Ciappi L., "Design and optimization of a Tesla turbine for ORC applications", in: Appl. Energy, 226, 300–319, 2018.

Appendix A Tesla expanders with exotic fluids

A.1   Tesla expanders - Two phase fluids

An attempt has been made in the past to introduce expanders in the reverse cycle applications, however the high realisation costs and reduced flexibility of the machinery design hindered their commercial success. The energy recovery using Tesla expanders in heat pump applications has potential in terms of improving overall efficiency of the heat pump with affordable cost. A potential application of Tesla turbine is described by Traverso et al [39] as energy recovery of the pressure difference between the condenser and the evaporator of refrigeration systems or heat pumps. Introduction of such expanders in refrigeration cycle can increase COP (Coefficient of Performance) up to 20%.

The expander utilizes the pressure difference between condenser and evaporator in the heat pump by production of useful power. This expansion is thermodynamically between isentropic (Figure A.1 (right) – CD') and isenthalpic line (Figure A.1 (right) – CD). The introduction of expander into the system reduces the consumption of mechanical energy of the compressor and reduces the quality (vapor mass fraction with respect to the total mass in liquid and vapor phases) of the working fluid at the evaporator inlet thus increasing the available enthalpy load $(h_A\text{-}h_{D'})$ available at the evaporator.

The increase in performance of a heat pump can be measured by an increase in coefficient of performance (COP). COP is defined as the ratio between the heat absorbed by the evaporator and the compressor work.

$COP = (h_A\text{-}h_{D'})\,/\,(h_B\text{-}h_A)$ (typical values of COP may range in the 2-10 interval depending upon the application, size and refrigerant)
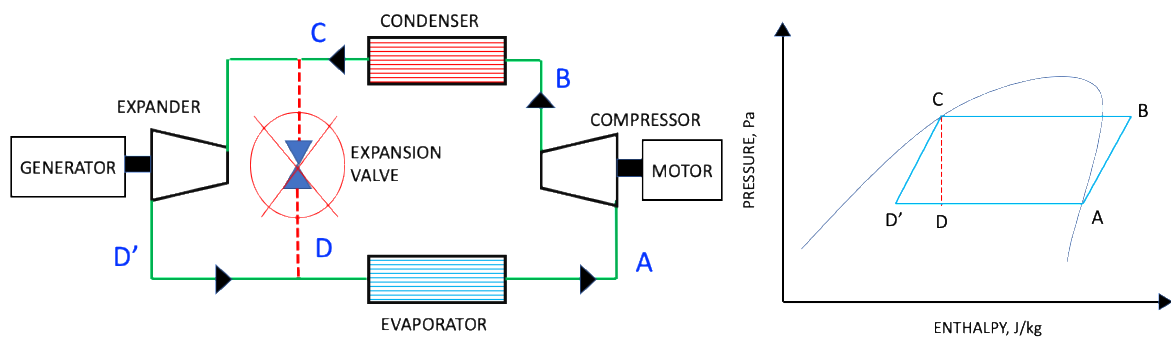
Figure A.1 Schematic of reverse Rankine cycle (left) and pressure-enthalpy chart (right)

Regarding the Tesla expander assisted heat pumps, the methodology presented in the Chapter 2 – 0-D design approach, for Tesla expander rotor is used (i.e. two-phase is considered as a uniform flow). The design conditions are shown in the Table A.1:

Table A.1 Design conditions for different two-phase expanders

Project	Fluid	dp across expander, bar	Mass flow, g/s	Rotational speed, rpm	Isentropic Power, kW
EU Horizon-20 PUMP-HEAT[1]	R-600 (Butane)	5	60	40000	0.9
EU Horizon-20 ENVISION[2]	R-134a	15	395	15000	1
Thessaloniki[3]	R410a	8	60	8000	0.13

1 = The expander is currently undergoing further testing.

2 = The expander manufacturing is done, and it will be installed in heat pump for testing

3 = Designed for Aristotle University of Thessaloniki during 2021 summer internship

Regarding the PUMP-HEAT, prototype consists of two-phase nozzle, Tesla rotor and integrated high-speed generator on same shaft and exhaust volute to recover exit kinetic energy.

A two-phase flow nozzle based "an improved homogeneous equilibrium model" developed at UNIGE consists of a convergent and divergent sections along with droplet enhancer. The droplet enhancer, developed at UNIGE, is technique used to increase the performance of the two-phase nozzle.

Figure A.2, A.3 and A.4 shows the CAD model and/or manufactured expander along with the p-h chart showing the two-phase expansion.
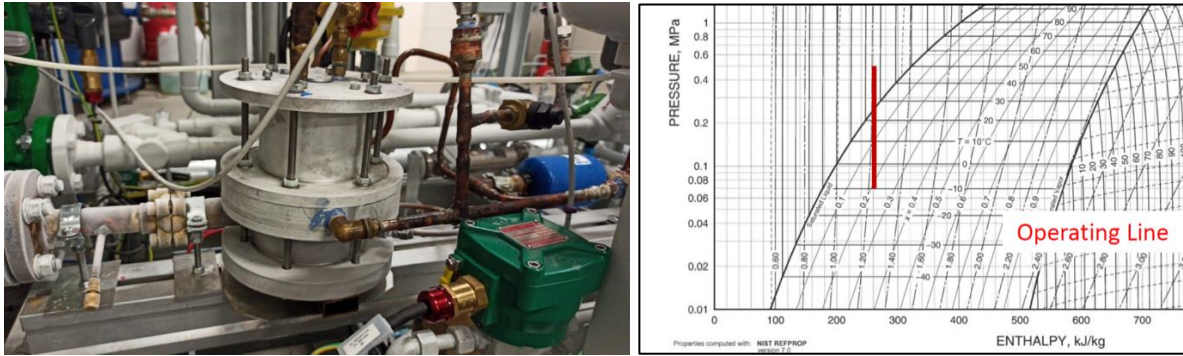
Figure A.2 R-600 two-phase expander installed inside a heat pump circuit and its design condition (PUMP-HEAT project) shown in p-h chart
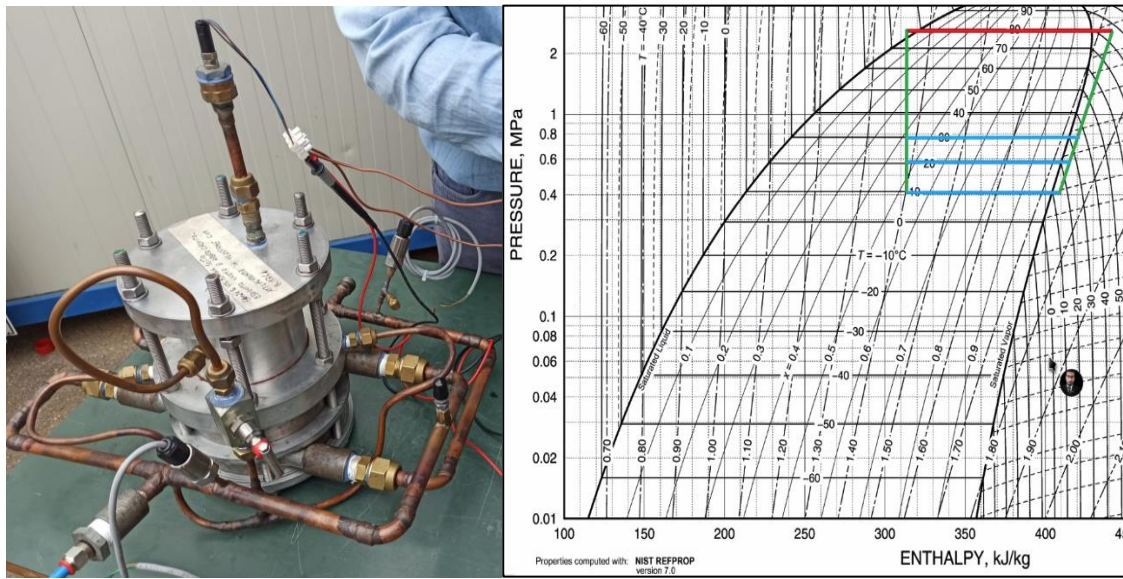

Figure A.3 R-134a two-phase expander installed inside heat pump and its design condition (ENVISION project) shown in p-h chart
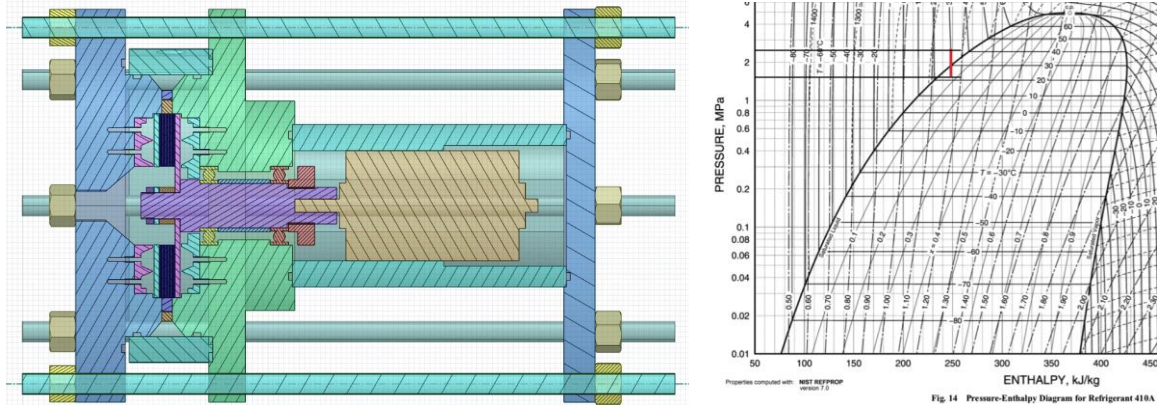
Figure A.4 R-410A two-phase expander CAD model and its design condition shown in p-h chart (Thessaloniki)

A.2   sCO₂ Tesla expander – A feasibility study

Supercritical carbon dioxide (sCO$_2$) plants are attracting a strong interest, particularly for distributed power generation, thanks to the high-power density, allowing high compactness and efficiencies due to the particular features of the fluid conditions near the critical point. Here, feasibility of Tesla expanders is evaluated for the first European demonstrator of MW size, coupling small volumetric flows with technological simplicity, typical of these types of plant (SOLARSCO2OL EU project). In particular, the possibility of replacing conventional turbines with bladeless expanders is studied, proposing a design in line with those achievable by small radial and axial turbomachines.

The design of rotor is carried out using 0-D model presented in Chapter 2. 3D numerical analysis is carried out using commercial computational fluid dynamic software as per solver and mesh set-up presented in Chapter 2. K-w SST turbulence model with coupled solver is used because of the high temperature at inlet. Ideal gas properties for carbon dioxide are used. The critical pressure and temperature for carbon dioxide 31 °C and 73.8 bar respectively. In this study, a sCO2 case is chosen from the SOLARSCO2OL project where both radial and axial stages are chosen for complete expansion of the fluid. The design conditions are specified in Table A.1, which shows the boundary conditions for the 3D CFD simulation of Tesla expander. Table A.2 shows the geometric parameters of Tesla expander rotor.

Table A.1 Design boundary conditions for Tesla expander

Total inlet pressure	180	bar
Total inlet temperature	565	°C
Static outlet pressure	80	bar
Mass flow	20,5	kg/s
Isentropic Power	2	MW

For the complete expansion of fluid in single stage Tesla turbine, 0-D tool gives the following rotor dimensions for rotor efficiency of ~80%. The efficiency, gap between disks and mass flow is selected based on axial length of the rotor. Based on the design flow rate of 20.5 kg/s, the density given by the operating conditions, and the optimum velocity ratio required for the Tesla rotor as discussed earlier, a throat section height for convergent nozzle of 0.23mm was calculated.

Table A.2 Geometric parameters of Tesla expander rotor

rotor outer diameter	160	mm
rotor inner diameter	70	°C
Gap between disks	0.1	mm
Number of nozzles	12	-
Nozzle throat height	0.23	mm
Number of disks	~1300	-

Figure A.3 shows the expected performance of sCO2 Tesla expander calculated through CFD. The results show ~55% total to static efficiency of the bladeless expander at 38000 rpm for approximately 1.25MW output power. The total to total efficiency is 64.5%, which signifies the importance of exhaust kinetic energy recovery. Figure A.3 also shows the efficiencies evaluated for rotor only. The gap between rotor only total to total efficiency and rotor+stator efficiency is more than 10 points. This gap in efficiency is due to losses between stator - rotor cavity and the partial admission of the fluid flow at the rotor inlet due to discrete number of

nozzles. The performance of Tesla expander looks promising for sCO2 applications. This work has also laid the basis for the development of a machine equipped with the same rotor disk pack implemented in water expander discussed in the thesis, which will allow the whole machine to approach an isentropic efficiency close to the rotor-only efficiency, i.e. around ~76%.
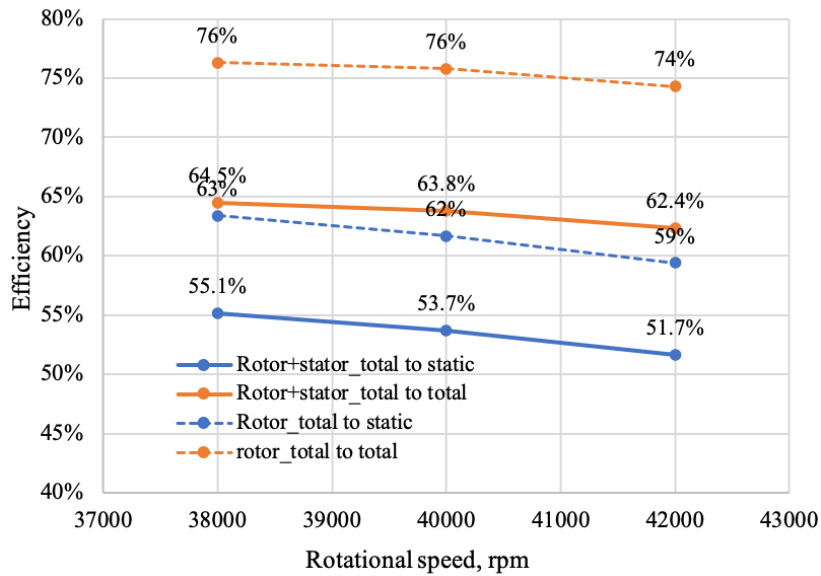

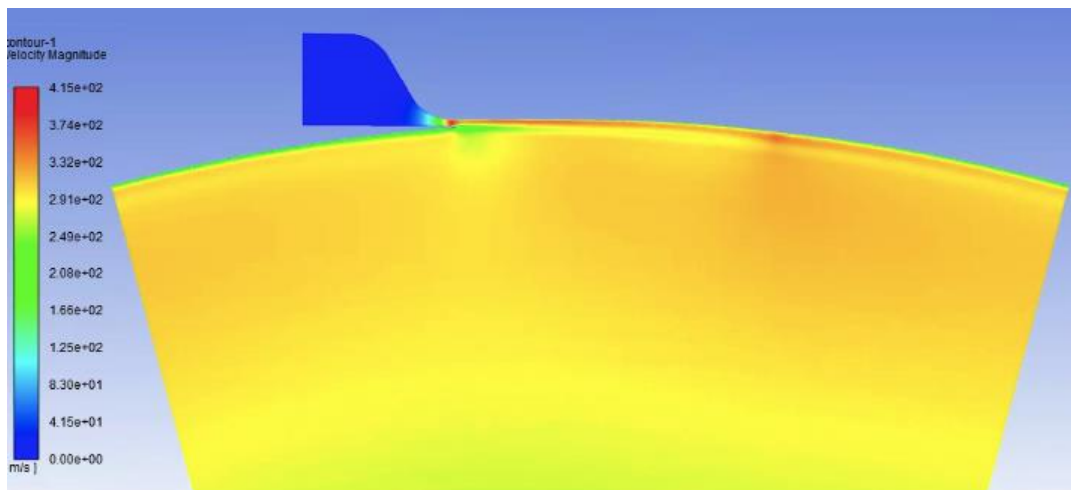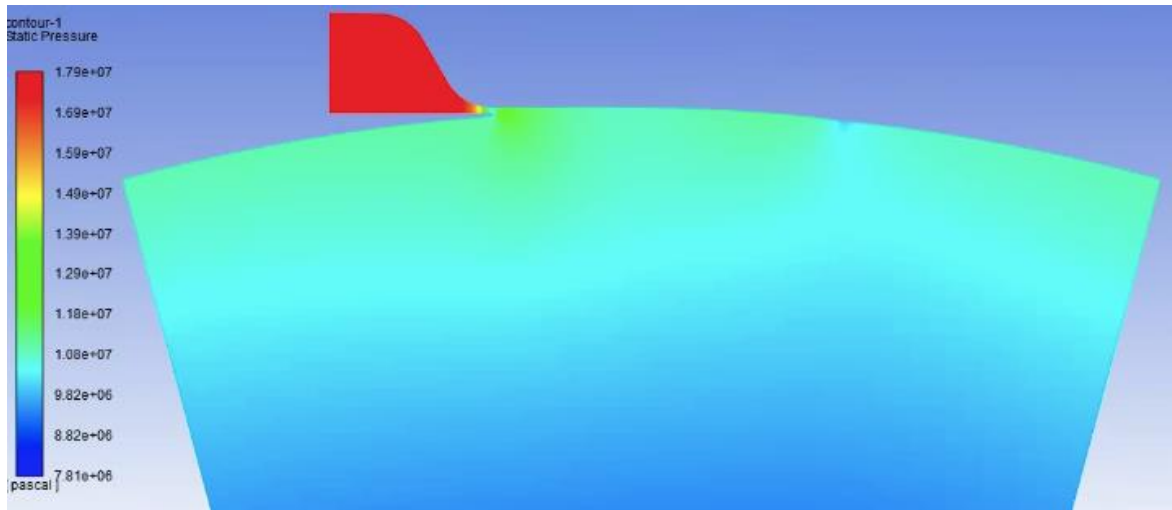Figure A.3 Efficiency versus rotational speed of the rotor estimated by CFD

Figure A.4 Contour plot of velocity at 38000 rpm

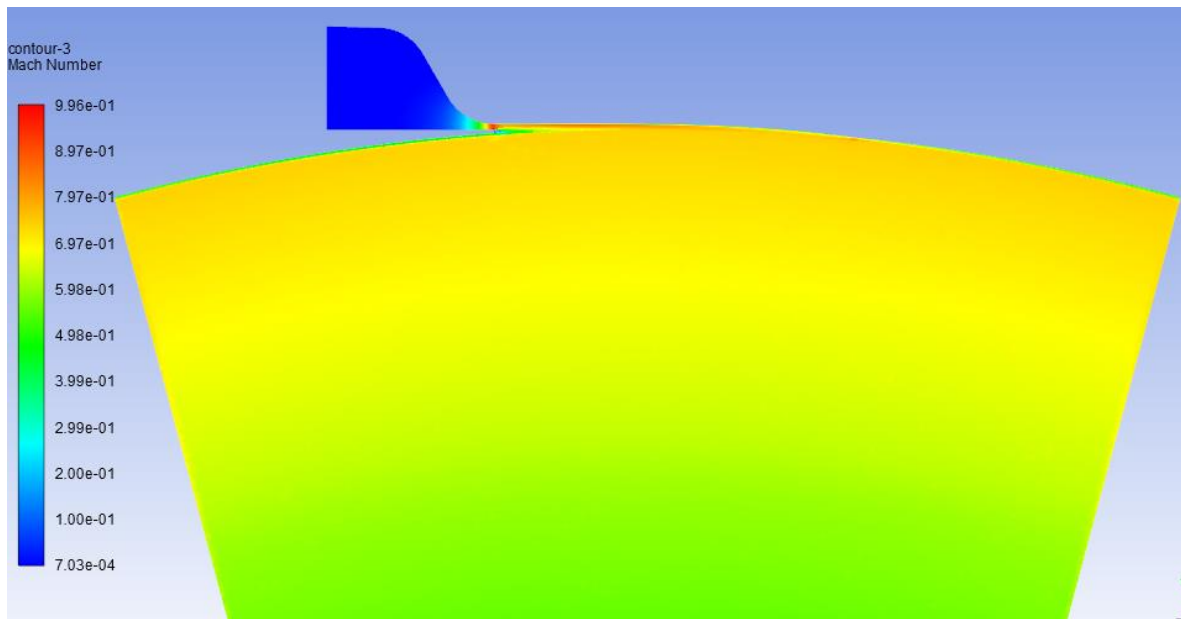Figure A.5 Contour plot of static pressure at 38000 rpm
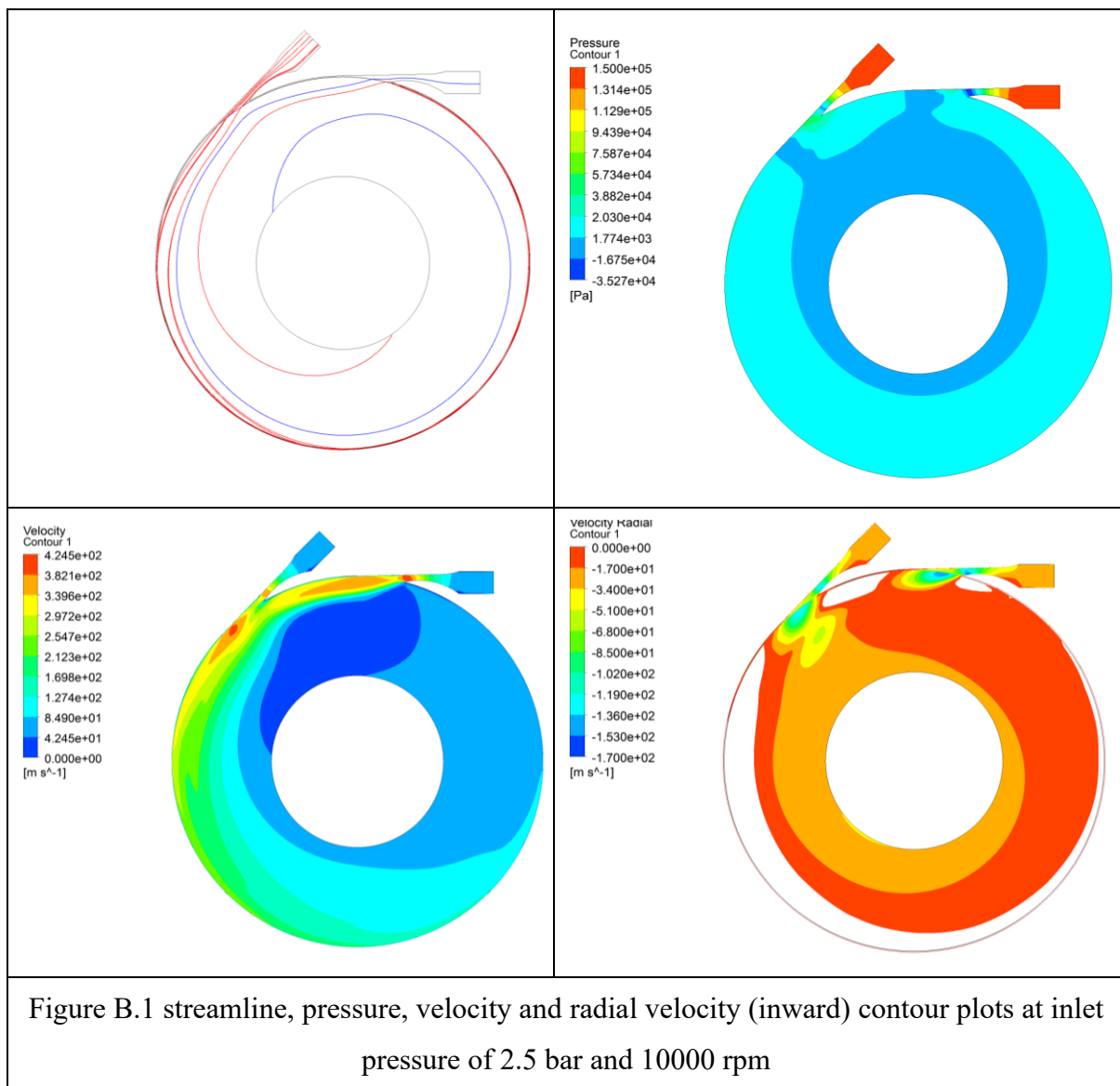

Figure A.6 Contour plot of Mach number at 38000 rpm

Appendix B CFD contour plots
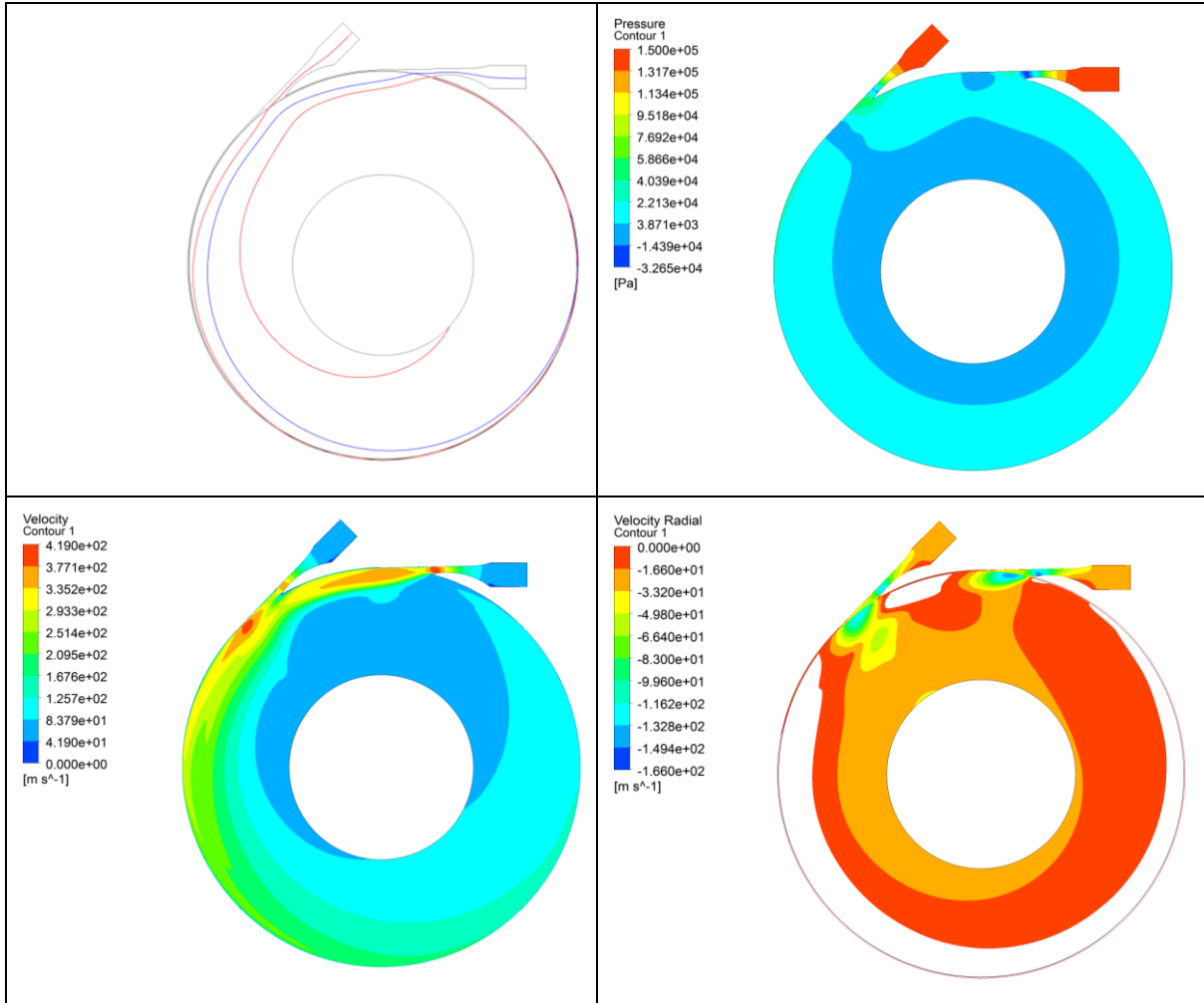
B.1   CFD contour plots for 100W Tesla air expander

Figure B.1 streamline, pressure, velocity and radial velocity (inward) contour plots at inlet pressure of 2.5 bar and 10000 rpm
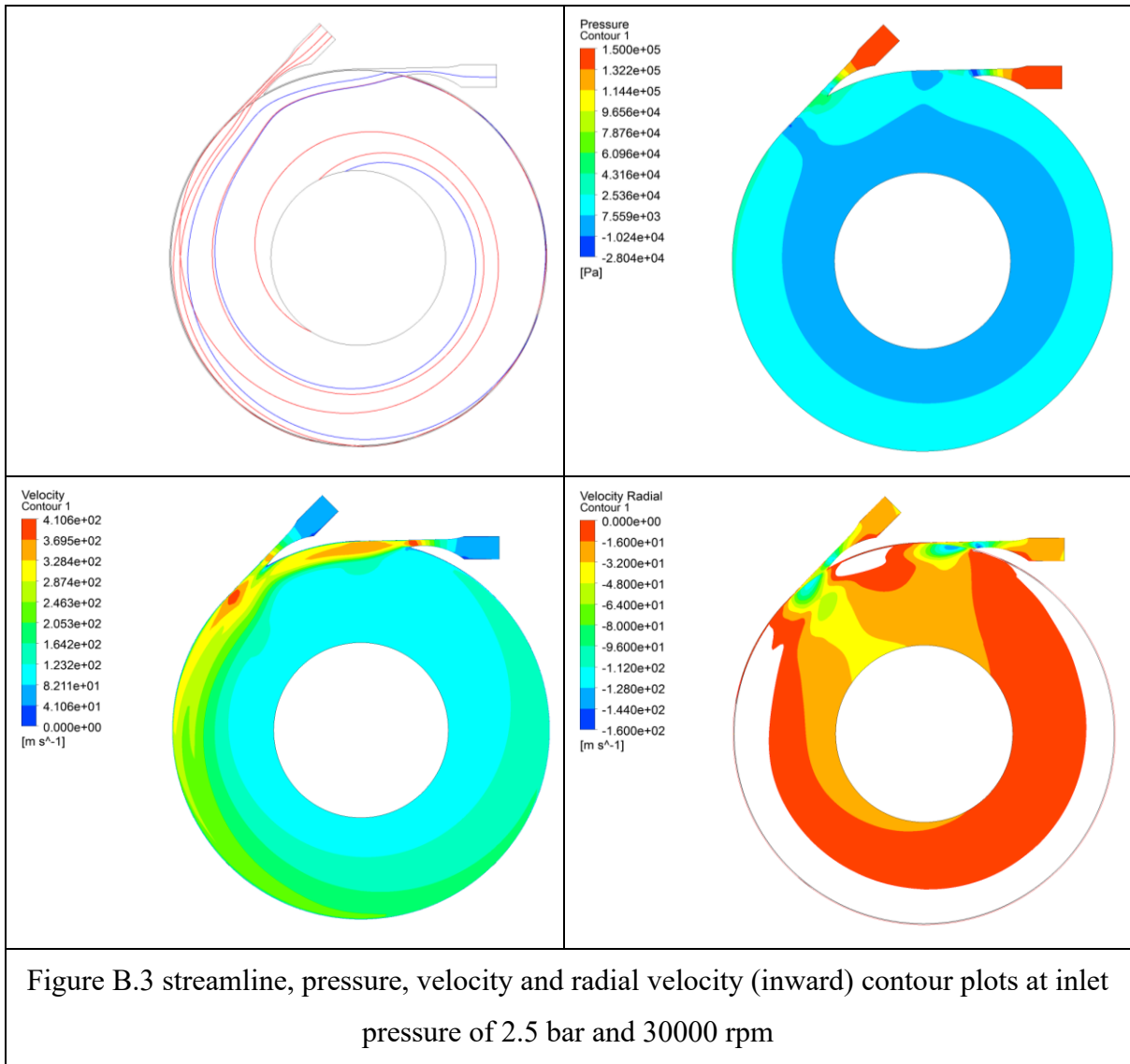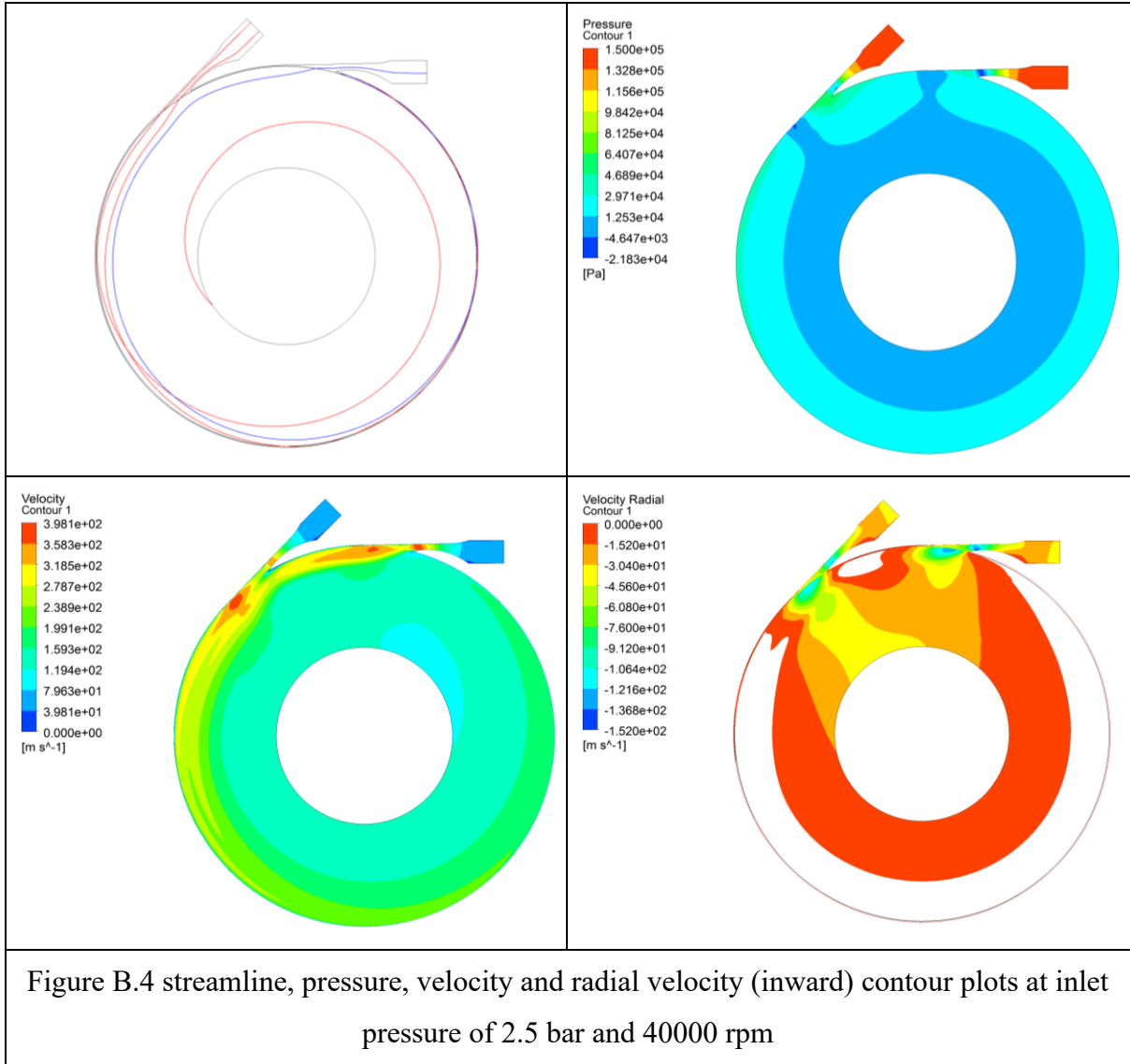
Figure B.2 streamline, pressure, velocity and radial velocity (inward) contour plots at inlet pressure of 2.5 bar and 20000 rpm

Figure B.3 streamline, pressure, velocity and radial velocity (inward) contour plots at inlet pressure of 2.5 bar and 30000 rpm
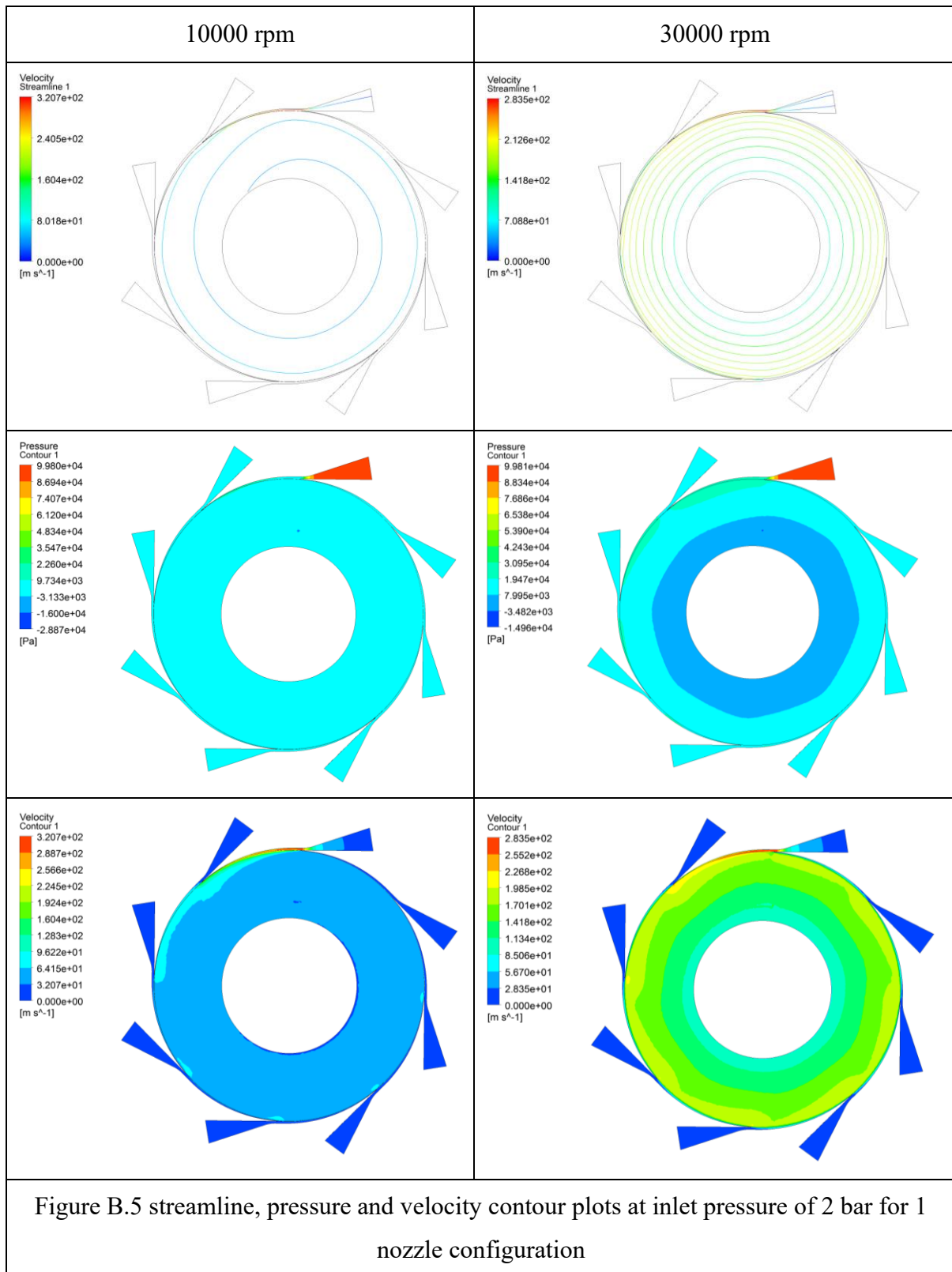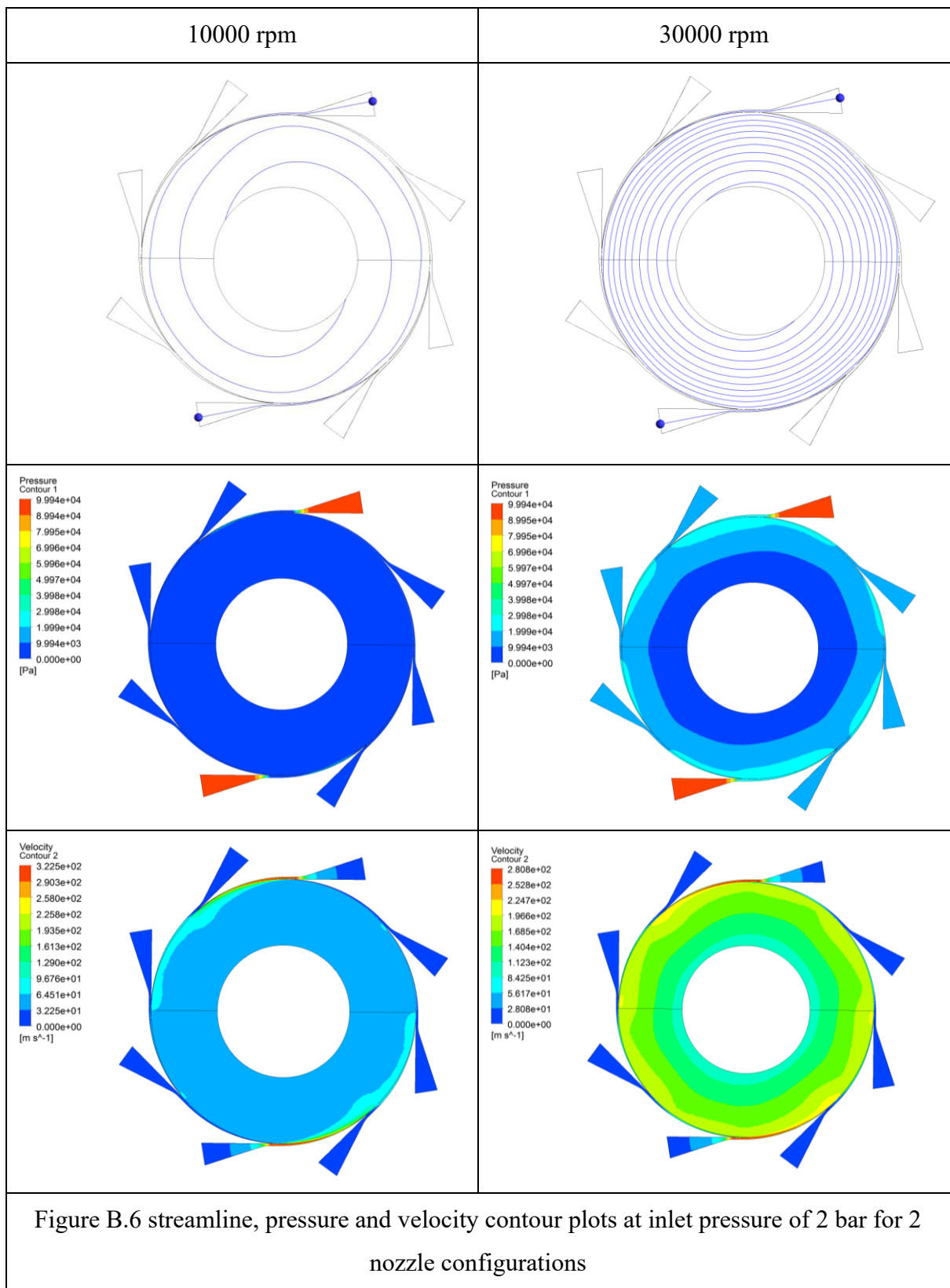
Figure B.4 streamline, pressure, velocity and radial velocity (inward) contour plots at inlet pressure of 2.5 bar and 40000 rpm

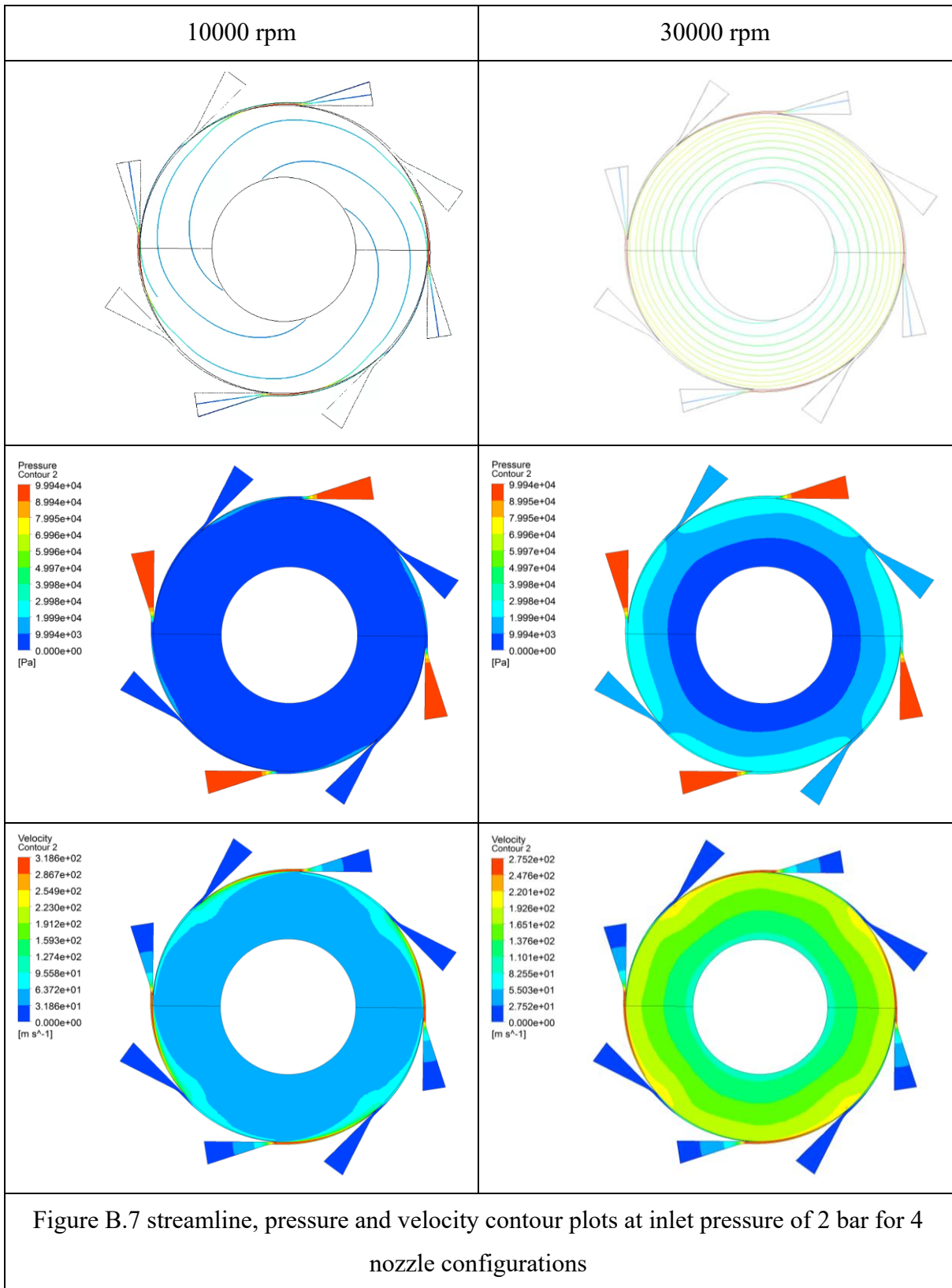## B.2   CFD contour plots for 3 kW Tesla air expander

10000 rpm	30000 rpm

Figure B.5 streamline, pressure and velocity contour plots at inlet pressure of 2 bar for 1 nozzle configuration

10000 rpm	30000 rpm

Figure B.6 streamline, pressure and velocity contour plots at inlet pressure of 2 bar for 2 nozzle configurations

10000 rpm	30000 rpm

Figure B.7 streamline, pressure and velocity contour plots at inlet pressure of 2 bar for 4 nozzle configurations

10000 rpm	30000 rpm

Figure B.8 streamline, pressure and velocity contour plots at inlet pressure of 2 bar for 8 nozzle configurations

Appendix C **Publications and patents**

1. Renuke, A., Vannoni, A., Pascenti, M., and Traverso, A., 2019, "Experimental and Numerical Investigation of Small Scale Tesla Turbines",. *ASME. Journal of Engineering Gas Turbines Power, Vol. 141(12),* 121011.

2. Renuke, A., Reggio, F., Ferrando, M., Pascenti, M., and Traverso, A., 2021, "Experimental Characterization of Losses in Bladeless Turbine Prototype",. *ASME. Journal of Engineering Gas Turbines Power,* GTP-21-1519

3. Ferrando M., Renuke A., Traverso A., and Sishtla V., 2021, " A new design method for two-phase nozzles in high efficiency heat pumps", International Journal of Refrigeration, 127(6)

4. Renuke, A., Reggio, F., Pascenti, M., Silvestri, P and Traverso, A., 2020, "Experimental Investigation on a 3 kW Tesla Expander With High Speed Generator", *ASME. TurboExpo'20,* GT2020-14572, London, England.

5. Renuke, A., Pascenti, M., and Traverso, A., 2019, "Performance Assessment of Bladeless Micro-Expander Using 3D Numerical Simulation",. *SUPEHR'19, E3S Web Conf.,Vol.113,*03016.

6. Renuke, A., Pascenti, M., and Traverso, A., 2019, "Experimental Campaign Tests on tesla Micro-Expanders",. *SUPEHR'19, E3S Web Conf.,Vol.113,*03015.

7. Vittorio Usai, Silvia Marelli, Avinash Renuke and Alberto Traverso., 2019, "Energy Harvesting Technology for turbo-compounding automotive engines with waste-gate valve ",. SUPEHR'19, E3S Web Conf., 113, 03020 (2019)

8. Renuke A. and Traverso A., 2019, "Performance Investigation of Tesla Bladeless Expander", International Gas Turbine congress, November 2018, Tokyo, Japan.

9. Renuke, A., and Traverso, A., 2022, "Assessment of Tesla Expander Performance Using 3D Numerical Simulation", *ASME. TurboExpo'22,* GT2022-82690, Netherlands.

10. Perri, A., Renuke, A., and Traverso, A., 2022, "Innovative Expanders for Supercritical Carbon-dioxide Cycles", *ASME. TurboExpo'22,* GT2022-83116, Netherlands.

11. Purushothaman, S., Renuke, A., Sorce, A., and Traverso, A., 2022 " A Review of Pressure Gain Combustion Solutions for Aerospace propulsion", *ASME. TurboExpo'22,* GT2022-83799, Netherlands.

Patents by the author

"Ultra-Efficient Bladeless Turbomachine", Italian patent application:102022000004460, Inventors: Avinash Renuke, Alberto Traverso, Matteo Pascenti, Paolo Silvestri, Federico Reggio, 2022

Appendix D Tesla expanders - Visibility

Tesla expanders being naïve technology need awareness amongst scientific community and industrial networks. Attempt have been made to disseminate results from this study through various platforms. Some of the initiatives are mentioned below:

Launch of Tesla Turbomachinery research Organisation (TTIO) at SUPHER conference at Savona, Italy

TTIO, is a non-profit organization devoted to scientific international research on Tesla or bladeless turbomachinery. Its main objective is to promote and gather worldwide scientific and technical contributions towards new knowledge and harmonization of Tesla turbomachinery technologies

Launch of TTIO – Dr Mathew Traum, University of Florida, USA addressing the launching event. Prof Traverso (right) chairing the launch session.
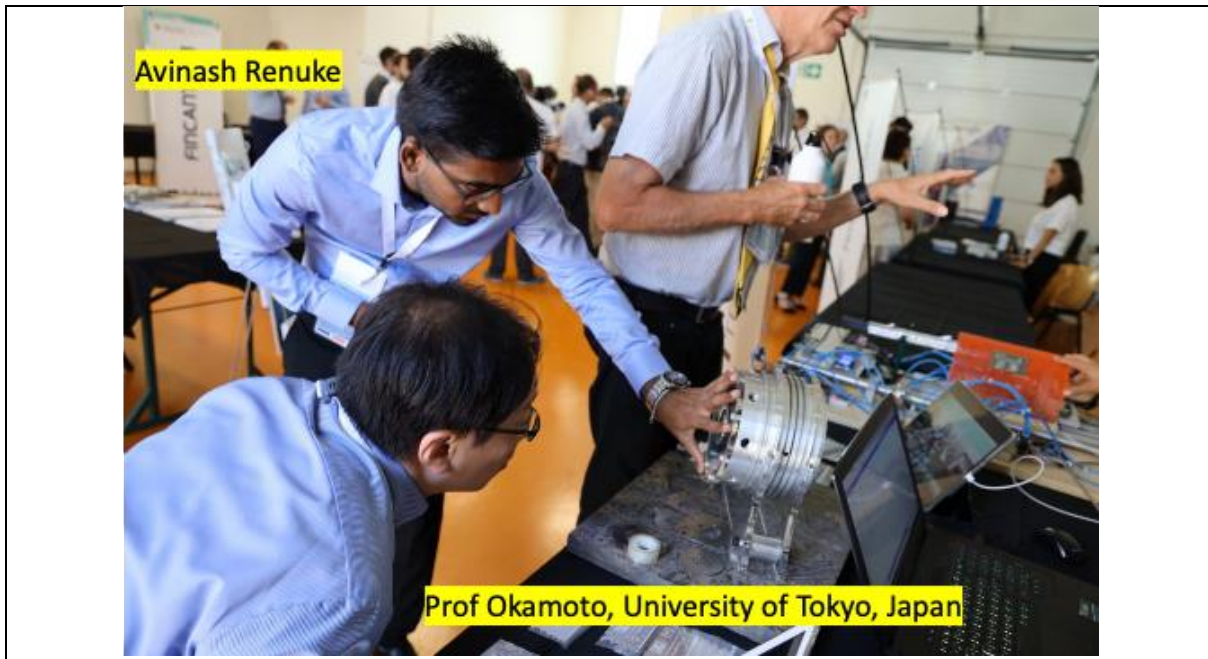
**ASME TurboExpo 2019 poster displayed at University of Florida by Prof Mathew Traum**

The poster is based on experimental characterisation of 100 W air expander and loss characterisation.
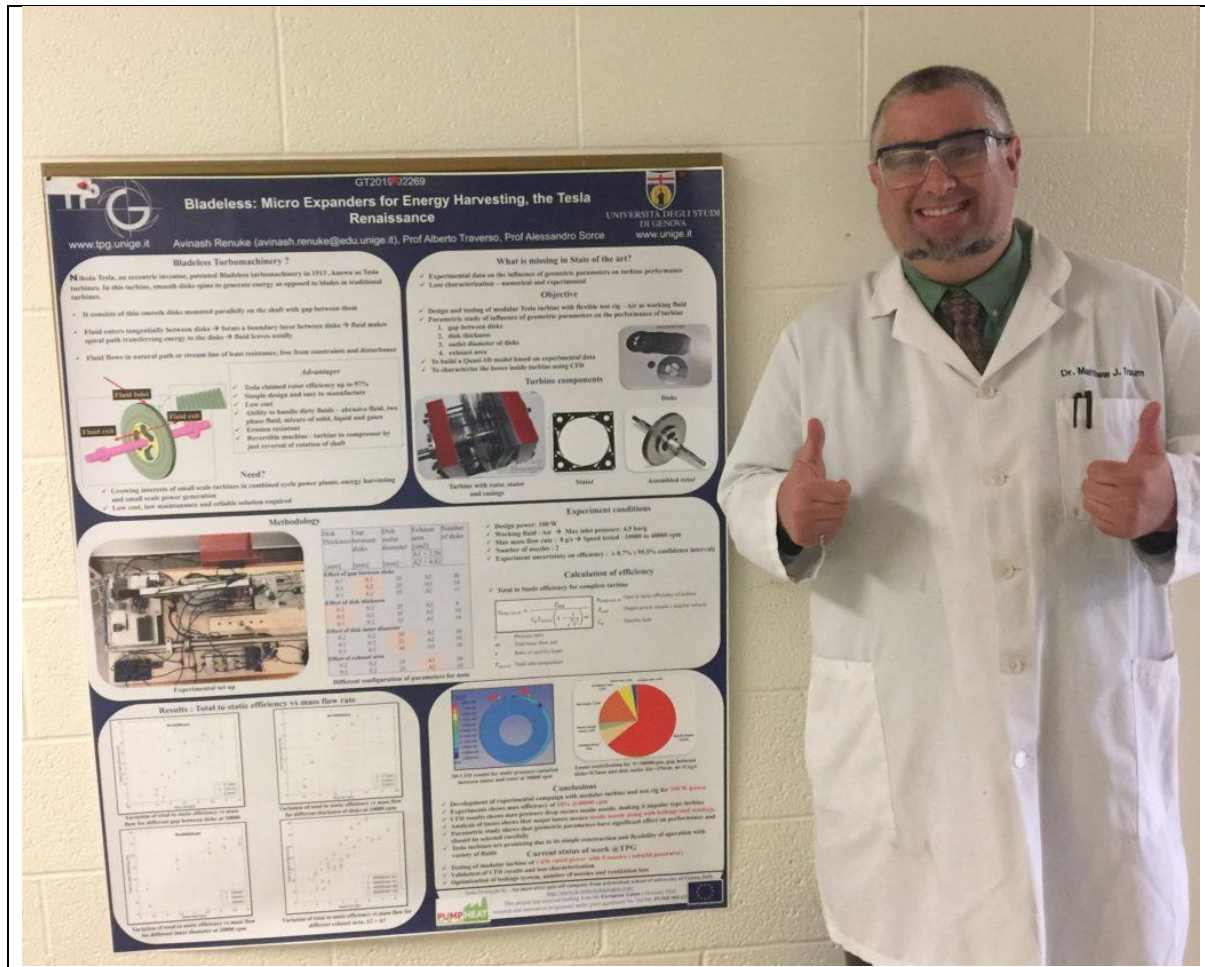
Display of 3 kW air Tesla expander at SUPHER'19 conference exhibition

Presentation of Tesla expanders at Mitsubishi Heavy Industries Ltd. Research and Innovation Centre, Takasago Japan
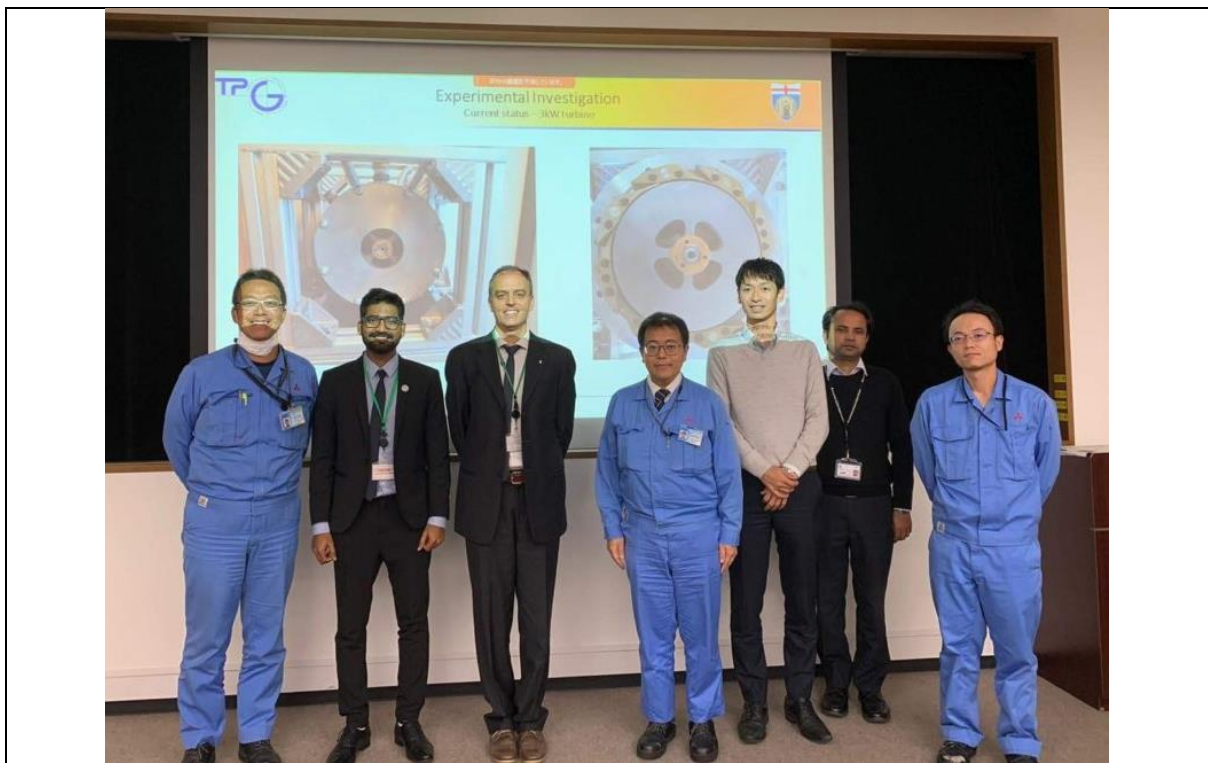
Tesla presentation at Headquarter of Mitsubishi Hitachi Power Systems Ltd, Yokohama, Japan

Tesla presentation at CRIEPI headquarter, Japan

Tesla presentation at Mayekawa heat pump industry, Tokyo, Japan

SIT Technologies booth at SUPEHR'19 displaying 3 kW Tesla air expander